# Experimental and Analytical Investigation of the Shallow-Flaw Effect in Reactor Pressure Vessels

Prepared by
T. J. Theiss, D. K. Shum, S. T. Rolfe

Oak Ridge National Laboratory

# Experimental and Analytical Investigation of the Shallow-Flaw Effect in Reactor Pressure Vessels

Prepared by
T. J. Theiss, D. K. Shum, S. T. Rolfe*

Oak Ridge National Laboratory
Operated by Martin Marietta Energy Systems, Inc.

Oak Ridge National Laboratory
Oak Ridge, TN 37831-6285

*University of Kansas, Lawrence, KS

# Abstract

The Heavy-Section Steel Technology (HSST) Program is investigating the increase in effective fracture toughness of A 533 B steel associated with shallow flaws and the implications of the shallow-flaw effect on reactor pressure vessel (RPV) life assessments. Test data from beams indicate a significant increase in the fracture toughness of shallow-crack specimens compared with deep-crack specimens in the transition region of the toughness curve for unirradiated A 533 B steel. If the toughness increase present in the test specimens were also present in a reactor vessel, the impact on pressurized-thermal shock (PTS) analyses could be significant. To facilitate transferability of the specimen data to an RPV, posttest finite-element analyses have been performed on several test specimens and a reactor vessel for a single (PTS) transient. The analyses are sufficiently refined to allow interpretation of the results in terms of the J-integral and the so-called Q-stress parameter under plane-strain analysis assumptions. A negative Q-stress parameter is indicative of a loss of crack-tip constraint, which is associated with an increase in the fracture toughness. Analyses of the test specimens indicate that at the onset of crack initiation the deep-crack specimens exhibit an essentially zero Q-stress parameter but that the shallow-crack specimen exhibits a Q-stress parameter of about –0.7, which indicates a substantial loss of constraint in the shallow-crack beam. Using the test data and posttest analysis, a locus of toughness data in terms of the J-integral and the Q-stress parameter has been constructed for a particular temperature. Analyses were also performed on an RPV with a shallow flaw under PTS loading conditions up to the maximum value of J. At maximum J, the analyses reveal a Q-stress parameter about –0.2 to –0.4, which indicates some constraint loss but less than in the shallow-crack test specimens. Considering the RPV in terms of J-integral and Q-stress suggests there may be a larger margin of safety than would be found using the J-integral alone. Thermal-shock data, which were generated using cylindrical vessels under thermal shock loading, show no significant increase in toughness even for shallow-flaw depths. The thermal shock data seem to indicate two offsetting effects: a shallow-flaw effect, which increases toughness, and an out-of-plane (biaxial) stress effect, which decreases toughness. Additional work is necessary to resolve outstanding issues for applying shallow-crack data to an RPV and validating the J-Q technique for fracture evaluations.

# Contents

# List of Figures

# List of Tables

# 1 Introduction

The Heavy-Section Steel Technology (HSST) program, sponsored by the Nuclear Regulatory Commission (NRC), is investigating the influence of crack depth on the fracture toughness of A 533 B material under conditions prototypic of a pressurized-water reactor (PWR) vessel.[1-4] Specifically, HSST is investigating the significance of the increase in fracture toughness associated with shallow- rather than deep-flaw specimens. The shallow-flaw fracture toughness increase (i.e., shallow-flaw effect) is due to a loss of constraint at the crack tip because of the proximity of the crack tip to the specimen surface.

The primary application of the HSST shallow-crack fracture toughness program is the pressurized-thermal-shock (PTS) accident scenario, which in some cases limits the operating life of a PWR reactor pressure vessel (RPV). Probabilistic fracture-mechanics analyses of an RPV have shown that shallow rather than deep flaws dominate the conditional probability of vessel failure in a PTS evaluation.[5-7] In fact, up to 95% of all initial crack initiations originated from flaws with depths of 25 mm or less. Shallow flaws contribute heavily to the conditional probability of failure for three main reasons. First, PTS life assessments are to be patterned after Reg. Guide 1.154,[8] which requires that all flaws be considered surface flaws. Furthermore, the flaw density distribution function assumed for PTS life assessments is based on the Marshall report,[9] which predicts more small flaws than large flaws. Thus, PTS analyses assume the existence of more shallow surface flaws than deep flaws. Second, PTS loading is more severe on the inner wall of the vessel that subjects shallow flaws to greater stresses. Third, in the beltline region of an RPV, irradiation damage is greatest at the inner surface of the vessel wall; this reduces the fracture toughness of the material in which a shallow surface flaw would reside. Furthermore, PTS evaluations indicate that most cracks initiate at temperatures above the lower shelf of the toughness curve for A 533 B steel (i.e., the transition region). The shallow-flaw effect in beams also takes place primarily at temperatures in the transition region. Thus, PTS analyses require that the fracture behavior of shallow surface flaws be well understood.

In addition to investigating the shallow-flaw effect for PTS analyses, the shallow-flaw investigation is important in the study of the general influence of constraint on fracture toughness. The HSST shallow-crack program has investigated the influence of both a loss of in-plane constraint (i.e., shallow-flaw effect) and a loss of out-of-plane constraint (i.e., thickness effect). The understanding of constraint is vital to the transferability of small-specimen toughness data to various structural applications (including RPVs). Additional applications important to NRC that

would benefit from an improved understanding of constraint include reactor vessel supports and circumferential-flaw analysis. Furthermore, American Society for Testing and Materials (ASTM) validity requirements in standard fracture toughness determinations may be appropriately relaxed based on a better understanding of the influence of constraint on fracture toughness.

The HSST shallow-flaw program is a joint experimental/analytical program that has produced a limited data base of shallow-flaw fracture toughness values and analysis to aid in the transferability of the specimen data to an RPV. The experimental portion of the program was divided into two phases: development and production. The development phase established the techniques appropriate for shallow-crack testing, verified the existence of a shallow-flaw effect in A 533 B beams, and compared beams of three thicknesses to choose the most appropriate thickness for the production phase of the program. Broken ends of the development phase beams were remachined and tested yielding six additional deep-crack beam tests. The production phase developed a limited data base of shallow-crack toughness values using relatively large laboratory specimens. All testing was conducted on three-point-bend specimens with a beam depth of ~100 mm (4 in.).

The analytical portion of the shallow-flaw program has conducted pretest analyses of the test specimens, posttest analyses of the test specimens, and analyses of an RPV subject to PTS loading with a shallow flaw. The pretest analysis was used to size the instrumentation used for the tests and select an appropriate shallow-crack depth. Posttest analyses have provided nondimensional factors necessary to determine the shallow-crack J-integral fracture toughness from test data for shallow-crack specimens. Posttest analysis has also quantified the constraint in the deep- and shallow-crack test specimens and an RPV under PTS loadings in terms of the Q-stress parameter to better understand the transferability of the specimen data to an RPV.

This report addresses several of the recommendations made earlier in an HSST shallow-flaw testing report.[4] The first recommendation, to test additional A 533 B shallow-crack specimens, is detailed in Chap. 2. Recommendation 2, posttest analyses of the test specimens, is covered in Chap. 3. Chapter 4 fulfills Recommendation 3, analysis of a flawed RPV under PTS loading. The analyses reported in Chaps. 3 and 4 use the J-Q fracture parameters, which satisfy Recommendation 5. Recommendation 4, a reexamination of thermal-shock[10] and pressurized-thermal-shock data, is included as a part of Chap. 5. Chapter 6 contains a summary and recommendations for future work.

NUREG/CR-5886
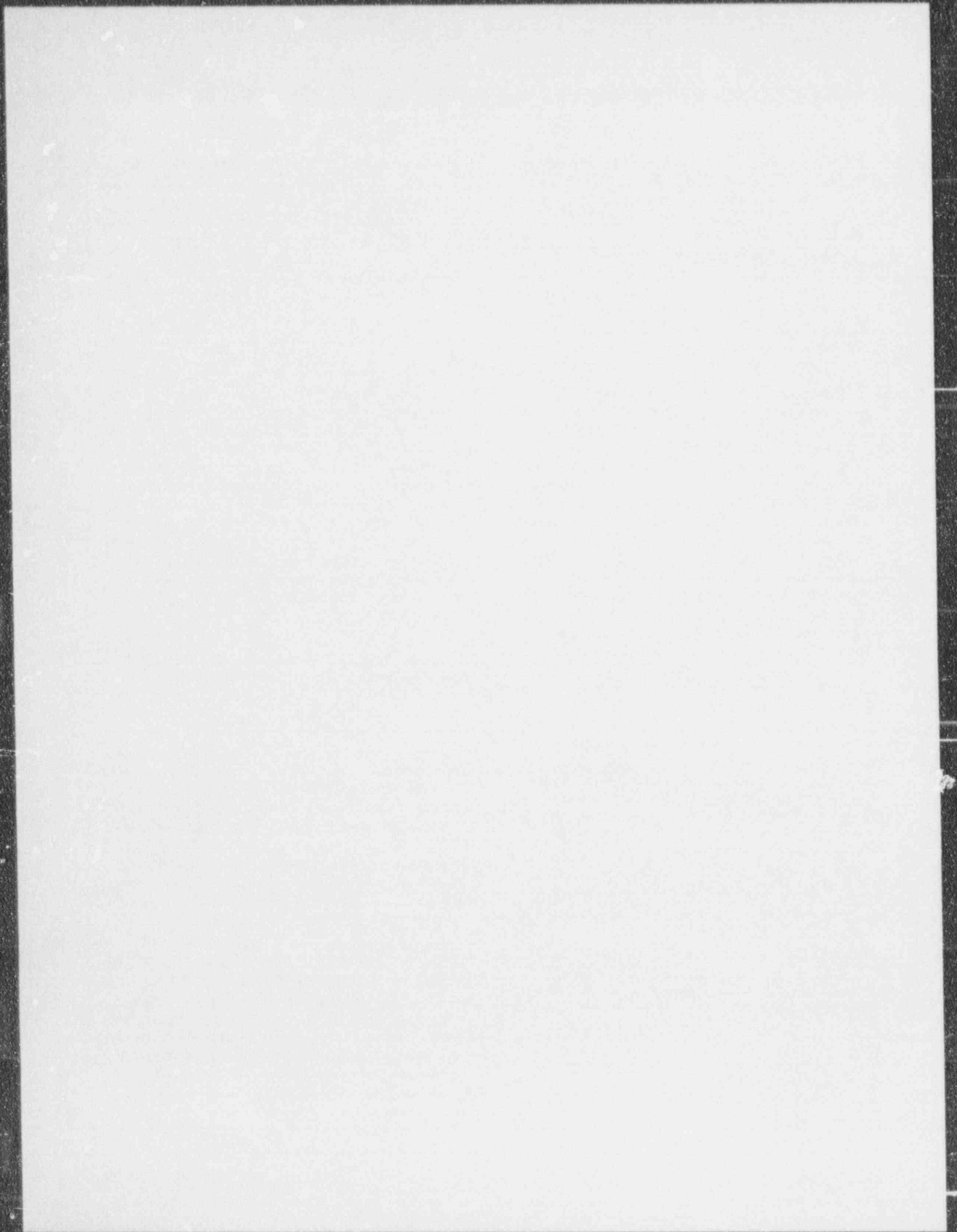
# 2 Test Results

This chapter describes the experimental results of the HSST shallow-crack fracture toughness program. The primary purpose of the shallow-crack testing was to develop a limited data base of shallow-crack fracture toughness values using relatively large laboratory A 533 B beam specimens. This chapter presents only an overview of the experimental results. Techniques used to collect shallow-crack data and properly determine the fracture toughness have been detailed previously[3,11] but are summarized in Appendix A for completeness. The test program was successful in collecting shallow- and deep-crack fracture toughness data .

## 2.1 Experimental Setup

The specimen configuration chosen for all testing in the shallow-crack program is the single-edge-notch-bend (SENB) specimen with a through-thickness crack [as opposed to the three-dimensional (3-D) surface crack]. A previous shallow crack[12,13] used SENB specimens. The straight-through notch simulates an infinitely long crack in an RPV. To simulate the conditions of a shallow flaw in the wall of a reactor vessel, the specimen depth W and thickness B must be of adequate size. Consistent with this requirement, a beam 100 mm deep (4 in.) was selected for use in the HSST shallow-crack project. PWR vessel walls are nominally 200 to 280 mm thick (8 to 11 in.). To maintain consistency with ASTM standards, the beams were

tested in three-point bending. All testing was conducted on unirradiated reactor material (A 533 grade B, class 1 steel) with the cracks oriented in the thickness (S) direction to simulate the material conditions of an axial flaw in an RPV. Specimens were taken from the center, homogeneous region of the source plate to prevent metallurgical differences between the material surrounding a shallow and deep flaw from influencing the toughness result. This is nonprototypic of an RPV because shallow flaws would be located in surface material of an RPV plate where large metallurgical gradients exist that have significantly greater fracture toughness.

To properly use shallow-crack fracture toughness data in the analysis of an RPV, the effect of out-of-plane (thickness) constraint on toughness must be well understood. To investigate the effects of out-of-plane constraint in the beams, the thickness was varied in the development phase tests to examine the effect on toughness. Three beam thicknesses were used:  B = 50, 100, and 150 mm (2, 4, and 6 in.). The span for the 50-mm-thick beam was 4W or 406 mm (16 in.). The spans for the 100- and 150-mm beams were increased to assure failure without exceeding the load capacity of the beam fixture. Figure 1 shows three of the beam sizes used in the shallow-crack testing. Both shallow- and deep-crack specimens were tested at each thickness. Beams 100 mm thick (4 in.) were used for the production phase tests. This beam was chosen for the

ORNL-PHOTO 8024-91
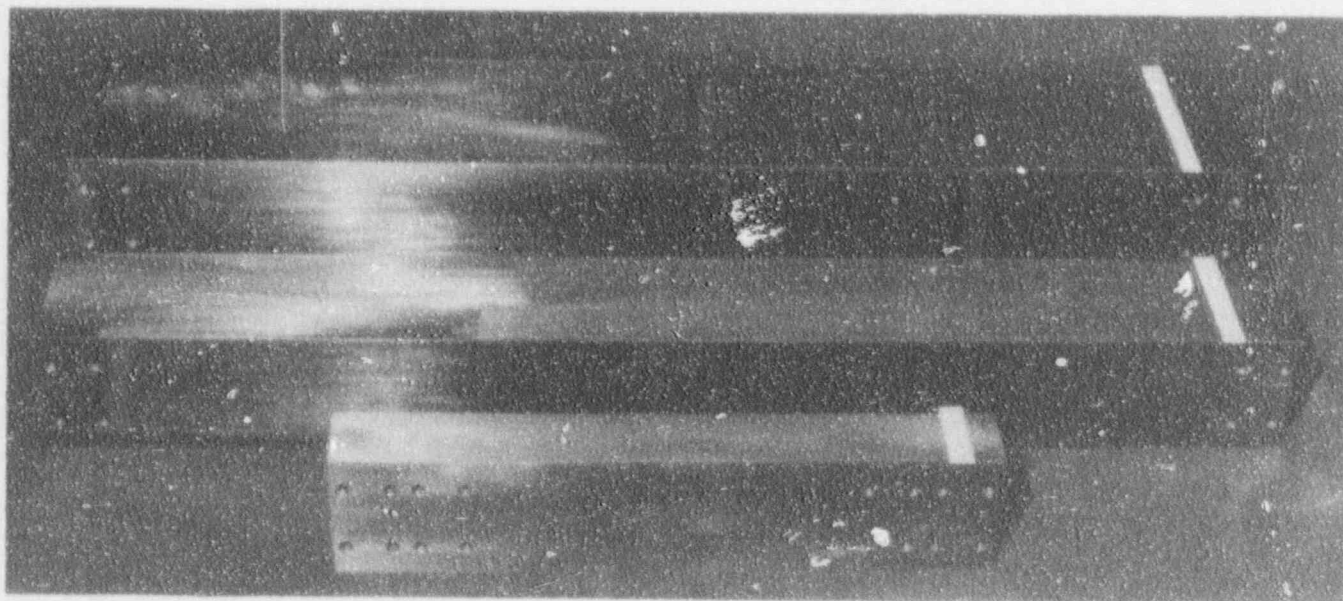


Figure 1  Three specimen thicknesses used in shallow-crack program to investigate size effects

production phase tests based on development phase results, which showed increased scatter for the 50-mm-thick beams but no substantial difference between the 100- and 150-mm-thick beams.

Two crack depths (one shallow and one deep) were tested during the shallow-crack fracture toughness testing program. The nominal shallow-crack depth chosen was a ≈ 10 mm (a ≈ 0.4 in.), which was representative of the flaw depths that resulted in a majority of the initiations in the integrated pressurized-thermal-shock (IPTS) studies.[5-7] Previous investigations defined the shallow-flaw effect in terms of normalized crack depth (a/W). These investigations used beams ~25 mm (1 in.) deep (a/W < 0.15). The specimen depth (W) and crack depth (a) for the HSST beams were chosen to allow interpretation of the shallow-crack beams in terms of "a" or a/W applicable for RPV analyses. One specimen was tested with a flaw depth of 14 mm (0.55 in.). All deep-crack specimens were cracked to an a/W ratio of ~0.5.

Instrumentation was attached to the specimens to make both J-integral and crack-tip-opening-displacement (CTOD) measurement of fracture toughness. The J-integral was determined from the load-line-displacement (LLD) using a reference bar attached to the beam fixture and a micrometer attached to the neutral axis of the beam. CTOD was determined from crack-mouth-opening displacement (CMOD) using clip gages mounted directly on the crack mouth of the specimen. Toughness data are expressed in terms of CTOD according to ASTM E1290-89, Crack-Tip Opening Displacement (CTOD) Fracture Toughness Measurement. ASTM E399, Plane-Strain Fracture Toughness of Metallic Materials, was used to analyze the deep-crack specimens to determine if the test results could be considered "valid" plane-strain ($K_{Ic}$) data. ASTM E813, $J_{Ic}$, A Measure of Fracture Toughness, is not strictly applicable to these tests because most of the failures were cleavage failures; however, critical J-integral cleavage values ($J_c$) were determined for each test. Techniques used to determine the CTOD and J-integral toughness are detailed in Appendix A.

## 2.2 Test Matrix

The development and production phases of the HSST shallow-crack testing program resulted in 14 and 18 data points, respectively. In addition, 6 deep-crack beams of varying thickness were tested to investigate out-of-plane (thickness) constraint effects yielding a data base of 38 specimens. The development phase tests were conducted primarily at one temperature (–60°C) using beams of three different thicknesses. The six additional deep-crack beams

were tested at –45°C using beams with different thicknesses. The production phase tests used one-beam geometry (100 by 100 mm) but were conducted at various temperatures. The total test matrix for the HSST shallow-crack fracture toughness program is shown in Table 1.

## 2.3 Material Characterization

Beams used in the development phase of the shallow-crack fracture toughness testing program were fabricated from HSST-CE Wide-Plate remains. A limited amount of material characterization was performed on this material as a part of that Wide-Plate test series.[14] The six additional deep-crack beams were cut from broken halves of several of the development phase specimens.

Source material for the beams in the production phase of the shallow-crack fracture toughness testing program was HSST Plate 13B. Material from HSST Plate 13A was used as source material for most of the wide-plate tests[15] and was extensively characterized at that time. HSST Plates 13A and 13B were originally fabricated as one plate (HSST Plate 13), which was cut into two pieces by the metal supplier for transport to ORNL. HSST Plate 13 is metallurgically typical of RPV plate material; however, RPVs receive a final heat treatment following the welding; this was not originally performed on HSST Plate 13. To be more prototypic of the conditions in RPV material, the production phase material was heat treated at 620°C (1150°F) for 40 h prior to final machining. A characterization piece was also heat treated and delivered for fabrication into the various characterization specimens and testing. The original characterization of this material (HSST Plate 13A) was performed in the L-T orientation. This recent characterization supplements the original characterization by providing properties in the L-S orientation through the plate thickness. All production phase shallow-crack testing was in the L-S orientation.

Material properties used in the analysis of the shallow-crack test results for both the development and production phases are included in Table 2. Additional information on the shallow-crack production phase material characterization can be found in Ref. 16. Subsequent shallow-crack material characterization has been performed, and results will be issued soon.*

---

*S. K. Iskander, "Preliminary Report on the Characterization of HSST Plate 13B in the L-S Orientation," to be issued as a USNRC NUREG report.

Table 1 Test matrix for the HSST shallow-crack program

| Phase | Temperature (°C) | Crack depth (mm) | Thickness (mm) | Number of beams tested |
|-------|------------------|------------------|----------------|------------------------|
| Development | –60 | ~50 | 50 | 3 |
| | –60 | ~50 | 100 | 1 |
| | –60 | ~50 | 150 | 1 |
| | –60 | ~50 | 50 | 3 |
| | –60 | ~10 | 100 | 2 |
| | –60 | ~10 | 150 | 2 |
| | –60 | ~14 | 50 | 1 |
| | –35 | ~10 | 50 | 1 |
| | | | Subtotal | 14 |
| Six additional beams | –45 | ~50 | 50 | 2 |
| | –45 | ~50 | 100 | 2 |
| | –45 | ~50 | 150 | 2 |
| | | | Subtotal | 6 |
| Production | –105 | ~10 | 100 | 3 |
| | –40 | ~50 | 100 | 3 |
| | –40 | ~10 | 100 | 3 |
| | –23 | ~10 | 100 | 3 |
| | –6 | ~50 | 100 | 3 |
| | –6 | ~10 | 100 | 3 |
| | | | Subtotal | 18 |
| | | | Total | 38 |

## 2.4 Results

Load vs CMOD curves were generated for each development beam tested at T = –60°C. To normalize the load between beams of different spans, thicknesses, and slightly different beam depths, the applied nominal bending stress (rather than applied load) was plotted vs CMOD. The applied stresses for the test and analysis results were calculated according to Mc/I, where M is the applied bending moment, c is the distance from the beam neutral axis to the location of the stress, and I is the second moment of inertia. The stress vs CMOD test data shown in Fig. 2 agree well with the analytical data, providing confidence in the experimental test data.

The analytical stress vs CMOD curves in Fig. 2 were generated using a plane-strain, elastic-plastic, finite-element ADINA[17] model. The test data represent beams of three different thicknesses. The consistency of the test data and the agreement with the plane-strain analytical results indicate little loss of out-of-plane constraint due to insufficient thickness of the test specimens.

Critical CTOD ($\delta_c$) and J-integral ($J_c$) toughness estimates were determined for each test from available load-CMOD and load-LLD data, respectively. Because $J_c$ and $\delta_c$ are related[18] according to $J_c = m\sigma_f\delta_c$, where m is the constraint parameter and $\sigma_f$ is the flow strength (average of yield and tensile strength), additional checks on the test data were made. The constraint parameter m was determined for each test and found to average 1.5 for deep-crack tests and 1.1 for shallow-crack tests; these are similar to previous analytical results.[12] The $\delta_c$ toughness data were converted to an elastic-plastic stress-intensity-factor $K_c$ according to $K_c = \sqrt{(m \cdot \sigma_f \cdot \delta_c \cdot E')}$, where m = 1.5 and $E' = E/(1 - \upsilon^2)$ for deep-crack specimens, and m = 1.1 and $E' = E$ for shallow-crack specimens. The plane-strain value of $E'$ was used for the deep-crack data because of the insensitivity of the deep-crack data to the specimen thickness. The plane-strain value of $E'$ is inappropriate for the shallow-crack data due to the loss of constraint and toughness increase in the data. Comparison of $K_c$ from the J-integral and $\delta_c$ calculations reveals consistent results (see Table 3).

### Table 2  Material properties for A 533 B steels used in HSST shallow-crack program

*Development phase and six deep-crack beams[a]*

HSST CE – WP

E = 206,850 MPa (30,000 ksi)

$v = 0.3$

$\sigma_0$ (room temperature) = 403 MPa (58 ksi)

$\sigma_u$ (room temperature) = 556 MPa (81 ksi)

$\sigma_f = 1/2 (\sigma_y + \sigma_u) = 480$ MPa

$RT_{NDT} = -35°C (-31°F)$

*Production phase*

HSST Plate 13B after postweld heat treatment

E = 206,850 MPa (30,000 ksi)

$v = 0.3$

$\sigma_0 = 452$ MPa at T = –40°C (66 ksi at –40°F)

$\sigma_u = 640$ MPa at T = –40°C (93 ksi at –40°F)

$\sigma_f = 1.17 \sigma_0 = 529$ MPa at T = –40°C

$RT_{NDT} = -15°C (+5°F)$ (center material)

---

[a] $\sigma_0$ and $\sigma_u$ estimated at other temperature from

$$\sigma_s = \sigma_0' - A + \frac{55,000}{T + 273} ,$$

where

$\sigma_0$ = yield strength at temperature T, MPa;

$T$ = temperature, °C;

$\sigma_0'$ = known $\sigma_0$ at temperature T;

$A$ = calibration constant.

The toughness data expressed in terms of $K_c$ vs temperature are presented in Table 3 and Fig. 3 (along with a material characterization curve for HSST Plate 13A[15]). The data show a significant increase in the fracture toughness for shallow-crack specimens in the transition region of the A 533 B toughness curve. All of the specimens failed in cleavage except the data point indicated with the arrow in Fig. 3. As expected, the shallow-crack specimens on the lower shelf, where linear-elastic behavior occurs, showed little to no toughness increase. The specimens had crack depths that were deep (a ~ 50 mm) or shallow (a ~10 mm) except for one beam with a crack depth of 14 mm. This intermediate crack-depth specimen also appears to show the shallow-crack-toughness elevation.

Toughness data are plotted as a function of beam thickness for all of the tests conducted at $T - RT_{NDT} = -25$ and $-11°C$ (–45 and –20°F) in Fig. 4. As indicated in Figs. 3 and 4, the toughness values for the shallow- and deep-crack specimens from the 100- and 150-mm-thick (4- and 6-in.) beams generally are consistent with the 50-mm-thick (2-in.) data. However, there appears to be slightly more data scatter associated with the 50-mm-thick (2-in.) beams than with the 100- and 150-mm-thick (4- and 6-in.) beams. None of the deep-crack tests strictly meet the requirements of ASTM E399 for a valid plane-strain $K_{IC}$ result due to insufficient crack depth. The beams, which had otherwise linear-elastic test records and were sufficiently thick for valid results, are indicated in Fig. 4.

ORNL-DWG 92M-2874 ETD
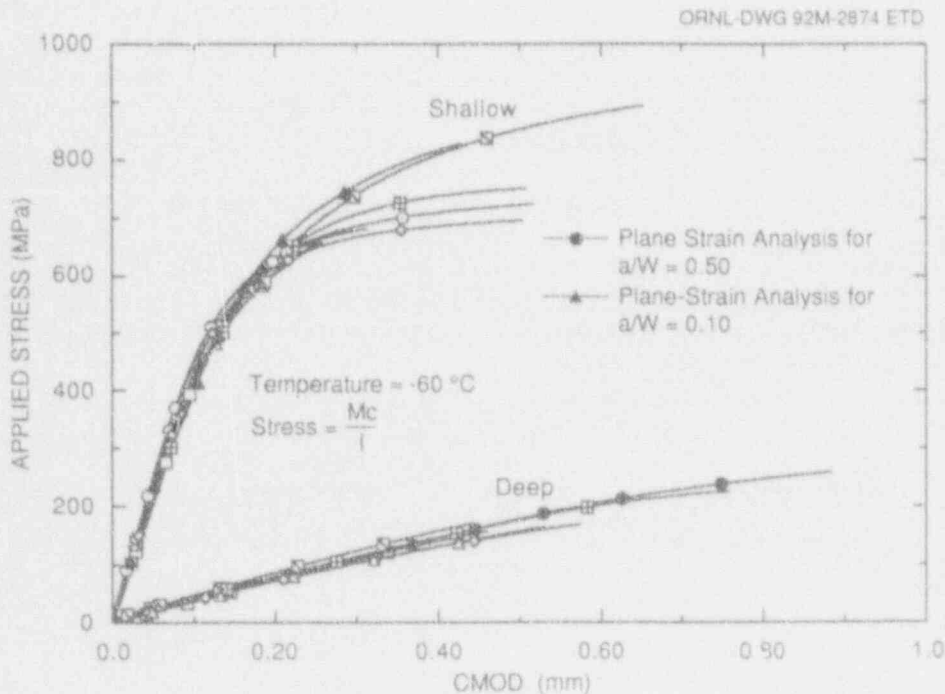


Figure 2  Applied stress vs CMOD for development beams tested at –60°C

6

Table 3 HSST shallow-crack test data

| HSST beam No. | Temperature (°C) | S (mm) | B (mm) | W (mm) | a (mm) | a/W | Failure load (kN) | CTOD total (mm) | J integral (MPa·mm) | $K_c$ from CTOD (MPa·√m) | $K_c$ from J (MPa·√m) |
|---|---|---|---|---|---|---|---|---|---|---|---|
| | | | | | | *Development phase* | | | | | |
| 3 | −36 | 406 | 51 | 100 | 10.0 | 0.10 | 600.0 | 0.586 | 261 | 269 | 232 |
| 4 | −61 | 406 | 51 | 100 | 51.8 | 0.52 | 128.1 | 0.048 | 42 | 97 | 97 |
| 5 | −55 | 406 | 51 | 99 | 51.2 | 0.52 | 139.7 | 0.049 | 48 | 97 | 105 |
| 6 | −59 | 406 | 51 | 100 | 51.9 | 0.52 | 184.6 | 0.117 | 102 | 151 | 152 |
| 7 | −59 | 406 | 51 | 94 | 10.2 | 0.11 | 483.5 | 0.137 | 92 | 134 | 138 |
| 8 | −60 | 406 | 51 | 94 | 9.6 | 0.10 | 657.4 | 0.476 | 284 | 250 | 243 |
| 9 | −62 | 406 | 51 | 94 | 9.5 | 0.10 | 552.4 | 0.352 | 173 | 215 | 189 |
| 10 | −60 | 406 | 51 | 94 | 14.0 | 0.15 | 489.3 | 0.235 | 143 | 176 | 172 |
| 11 | −57 | 864 | 102 | 94 | 8.4 | 0.09 | 472.4 | 0.196 | 101 | 160 | 145 |
| 12 | −57 | 864 | 102 | 95 | 49.8 | 0.53 | 116.5 | 0.061 | 50 | 109 | 106 |
| 13 | −60 | 864 | 102 | 94 | 8.8 | 0.09 | 501.7 | 0.357 | 208 | 216 | 208 |
| 14 | −60 | 864 | 152 | 93 | 8.7 | 0.09 | 723.2 | 0.346 | 225 | 212 | 216 |
| 15 | −59 | 864 | 153 | 94 | 8.7 | 0.09 | 684.1 | 0.146 | 85 | 138 | 133 |
| 16 | −58 | 864 | 153 | 94 | 50.0 | 0.53 | 170.4 | 0.060 | 46 | 108 | 102 |
| | | | | | | *Six deep-crack beams phase* | | | | | |
| 12A | −44 | 406 | 102 | 94 | 51.0 | 0.54 | 251.8 | 0.077 | 60 | 120 | 117 |
| 13A | −46 | 406 | 102 | 94 | 50.8 | 0.54 | 293.1 | 0.111 | 86 | 144 | 140 |
| 14A1 | −44 | 406 | 51 | 93 | 50.2 | 0.54 | 135.2 | 0.121 | 93 | 150 | 145 |
| 14A2 | −44 | 406 | 51 | 93 | 50.8 | 0.55 | 102.7 | 0.043 | 39 | 90 | 94 |
| 15A | −47 | 406 | 153 | 94 | 50.7 | 0.54 | 435.0 | 0.094 | 79 | 133 | 134 |
| 16A | −43 | 406 | 153 | 94 | 51.9 | 0.55 | 348.3 | 0.062 | 51 | 107 | 108 |
| | | | | | | *Production phase* | | | | | |
| 17 | −6 | 610 | 102 | 102 | 52.6 | 0.52 | 245.1 | 0.116 | 96 | 142 | 148 |
| 18 | −24 | 610 | 101 | 102 | 10.6 | 0.10 | 777.1 | 0.466 | 238 | 239 | 222 |
| 20 | −4 | 610 | 101 | 101 | 10.8 | 0.11 | 823.3 | 1.733 | 985 | 451 | 451 |
| 21 | −23 | 610 | 101 | 102 | 10.7 | 0.11 | 724.1 | 0.306 | 152 | 193 | 177 |
| 22 | −7 | 610 | 101 | 102 | 10.9 | 0.11 | 793.5 | 0.942 | 564 | 333 | 342 |
| 24 | −7 | 610 | 102 | 102 | 52.0 | 0.51 | 269.1 | 0.367 | 268 | 253 | 247 |
| 25 | −39 | 610 | 102 | 102 | 52.0 | 0.51 | 238.4 | 0.110 | 85 | 144 | 139 |
| 26 | −40 | 610 | 102 | 102 | 11.0 | 0.11 | 740.1 | 0.355 | 175 | 212 | 191 |
| 27 | −22 | 610 | 101 | 102 | 10.7 | 0.11 | 787.3 | 0.559 | 242 | 261 | 224 |
| 28 | −6 | 610 | 101 | 102 | 10.3 | 0.10 | 832.7 | 1.242 | 786 | 382 | 403 |
| 31 | −40 | 610 | 102 | 102 | 51.5 | 0.51 | 205.5 | 0.063 | 51 | 109 | 108 |
| 32 | −103 | 610 | 102 | 102 | 11.1 | 0.11 | 417.7 | 0.018 | 20 | 52 | 65 |
| 33 | −103 | 610 | 102 | 102 | 10.7 | 0.11 | 339.8 | 0.010 | 13 | 40 | 51 |
| 34 | −106 | 610 | 101 | 102 | 10.4 | 0.10 | 431.0 | 0.019 | 21 | 54 | 67 |
| 35 | −7 | 610 | 102 | 102 | 51.7 | 0.51 | 244.2 | 0.121 | 95 | 146 | 147 |
| 36 | −38 | 610 | 102 | 102 | 51.6 | 0.51 | 176.1 | 0.042 | 35 | 89 | 89 |
| 37 | −39 | 610 | 102 | 102 | 10.8 | 0.11 | 745.9 | 0.263 | 135 | 182 | 167 |
| 38 | −39 | 610 | 102 | 102 | 10.8 | 0.11 | 755.3 | 0.206 | 106 | 162 | 148 |

Test
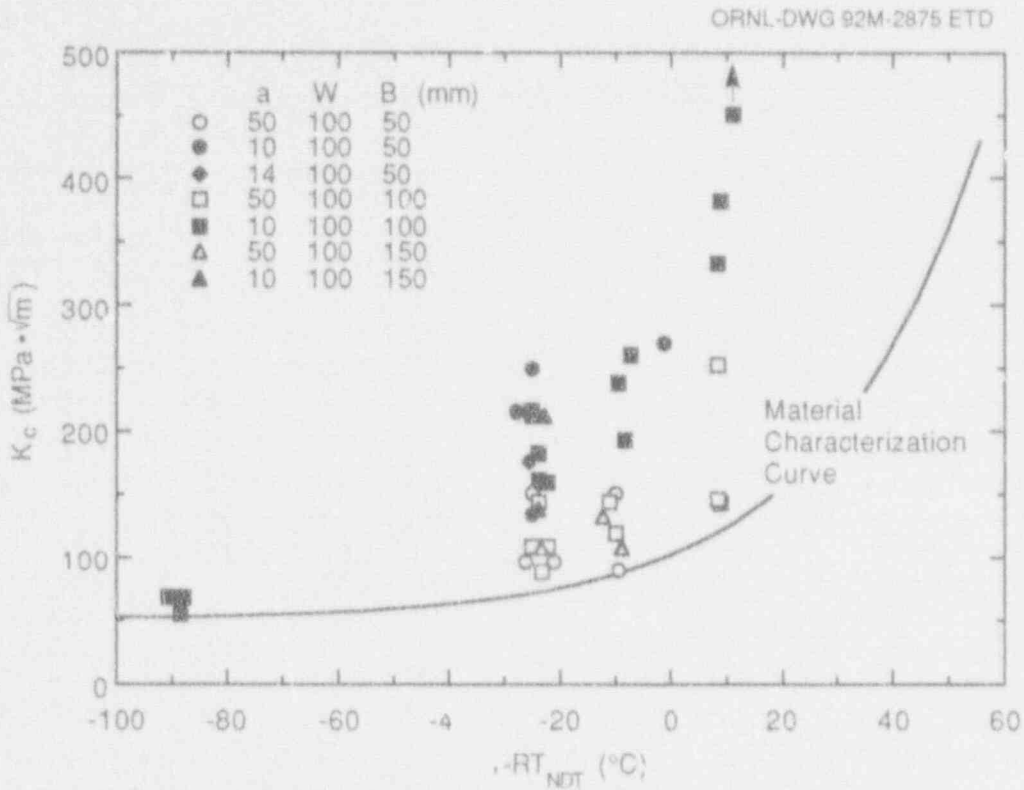
Figure 3 All toughness ($K_c$) data vs normalized temperature for shallow- and deep-crack specimens

ORNL-DWG 92M-2876 ETD
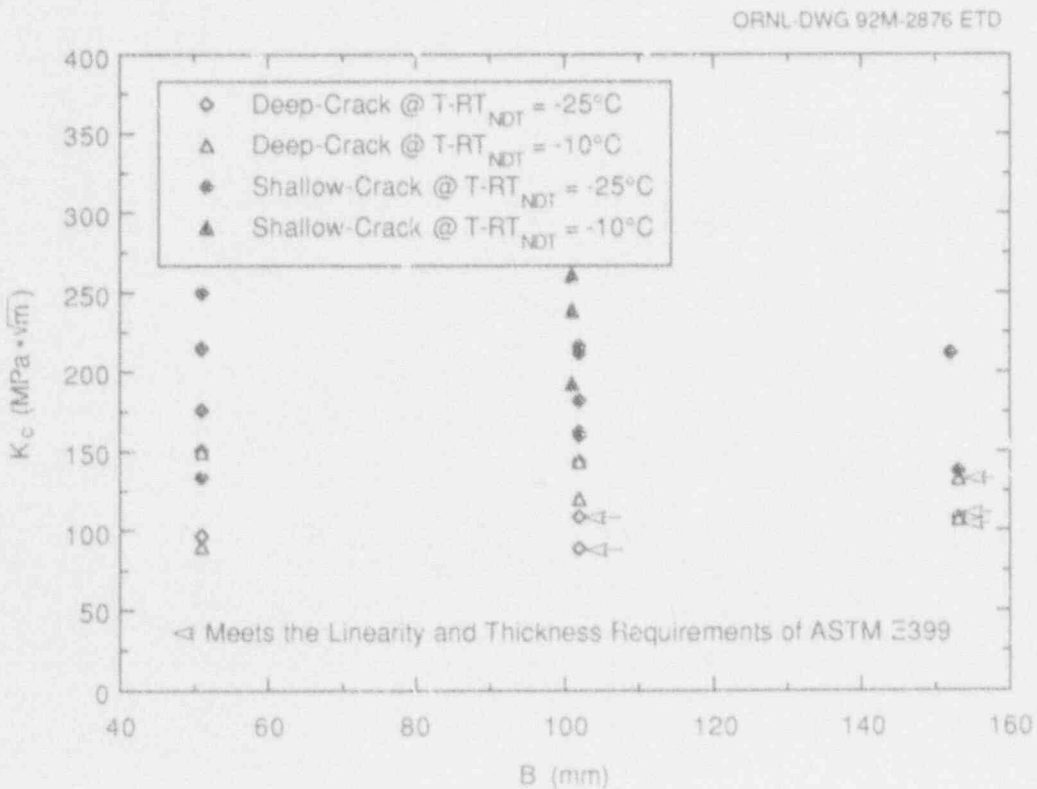
Figure 4 Toughness ($K_c$) data vs beam thickness for shallow- and deep-crack specimens at T = −60, −45, and −40°C

The shallow-crack toughness increase can be quantified in terms of a ratio of toughness values at one temperature or a temperature shift. The ratios of the shallow-to-deep lower-bound $\delta_c$ at $T = -60$ and $-40°C$ are 2.4 and 4.9, respectively, which is consistent with the A36 (Ref. 12) and A517 (Ref. 13) results from the University of Kansas. In terms of $K_c$, the shallow-crack-toughness increase is ~60% at $T =$

$-60°C$. Figure 5 shows the shallow-and deep-crack test data with approximate lower-bound curves. The shallow-crack, lower-bound curve was formed using the deep-crack, lower-bound curve shifted by 35°C (63°F). The shifted deep-crack, lower-bound curve fits the shallow-crack data well at all test temperatures.

ORNL-DWG 92M-2877 ETD
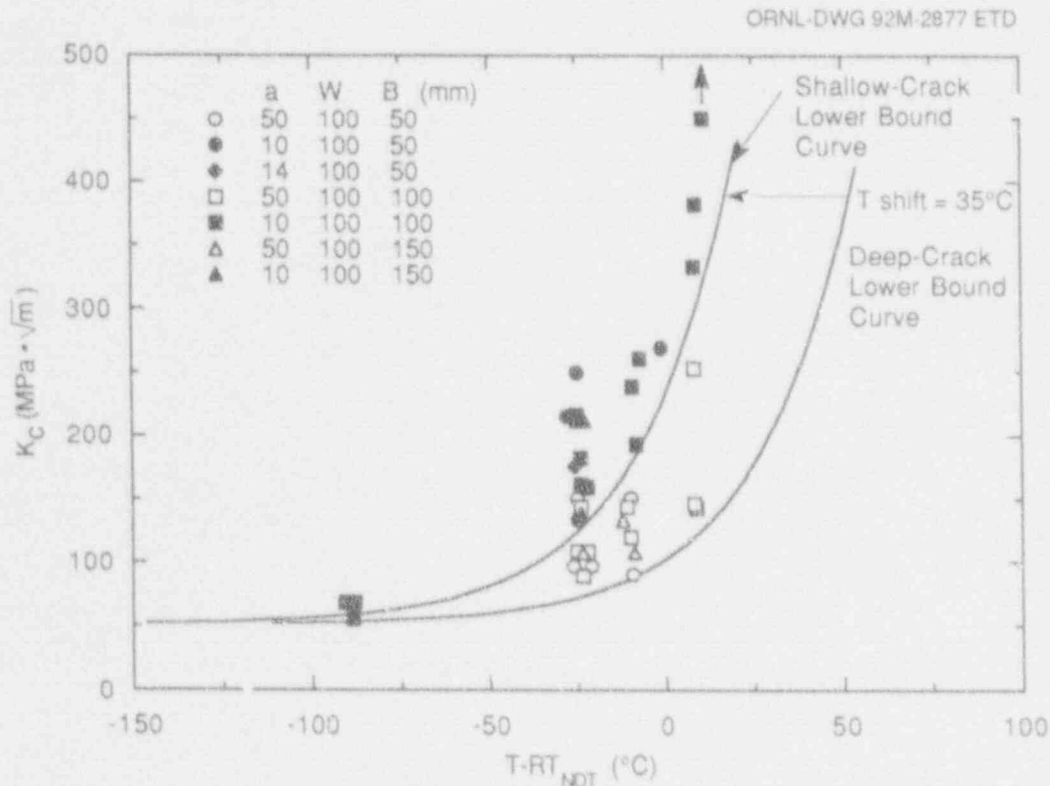


Figure 5 All toughness ($K_c$) data vs normalized temperature for shallow- and deep-crack specimens with shallow- and deep-crack lower-bound curves

9

# 3 Posttest Specimen Analysis

This chapter presents detailed posttest two-dimensional (2-D) plane-strain analysis results for a select number of specimens from the production phase of the shallow-flaw fracture toughness testing program. Specifically, detailed finite-strain, finite-element analyses were performed for six specimens that were tested at –40°C. Three of the specimens (beams 36, 31, and 25) are deep-flaw specimens with a nominal crack-depth to specimen-width ratio of a/W = 0.5, while the remaining three are shallow-flaw specimens (beams 38, 37, and 21) with a nominal a/W = 0.1. As shown in Table 2, the three shallow-flaw specimens exhibited higher toughness levels than the three specimens with deep flaws. The primary objectives of these analyses are to (1) evaluate the utility of the recently proposed two-parameter J-Q concept[19,20] to characterize the crack-tip fields up to the onset of crack initiation in specimens with either deep or shallow flaws, and (2) provide a framework for interpreting and ordering the observed toughness differences between the deep- and shallow-flaw geometries.

## 3.1 Material Models

Two material models have been adopted in the analysis of the test specimens. The first material model simulates the unirradiated tensile properties of A 533 B (HSST Plate 13B) at –40°C (–40°F) as determined from characterization studies (Chap. 2). The linear elastic portion of the true stress–true strain curve is characterized by a yield strain of magnitude $\varepsilon_0 = \sigma_0/E = 0.0022$, where the Young's modulus $E = 207.2$ GPa ($30 \times 10^6$ psi), the uniaxial yield stress in tension $\sigma_0 = 454$ MPa (65.8 ksi), and Poisson's ratio $\nu = 0.3$. The uniaxial true-stress, true-plastic-strain curve in tension is modeled in a multilinear fashion as indicated in Fig. 6. In subsequent discussions this material model is referred to as the unadjusted model.

Posttest analysis results to be presented indicate that finite-element models based in part on the unadjusted material

ORNL-DWG 92-2878 ETD
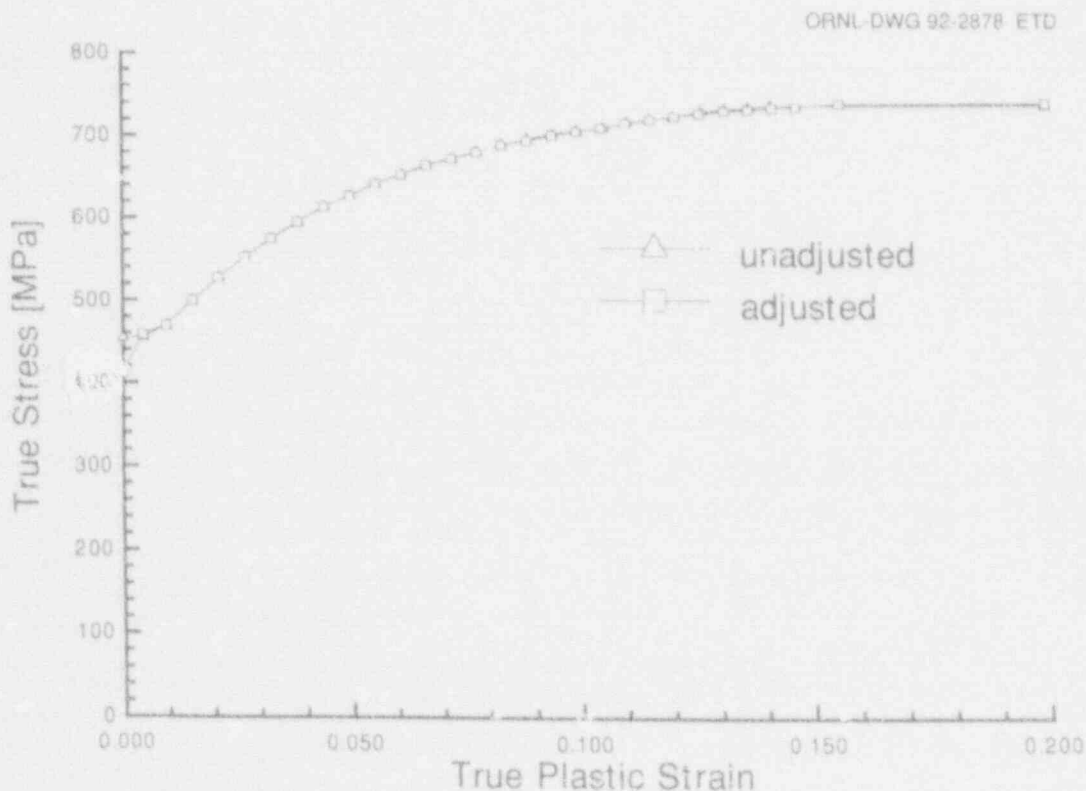


Figure 6 Uniaxial true stress–true plastic strain curve in tension for unadjusted and adjusted material models

model underestimate the displacements of the specimens as compared with experimentally measured values. Various reasonable analysis options to reduce the stiffness of the finite-element models have been attempted. One option, in conjunction with other analysis techniques to be described later, that results in good agreement between calculated and measured mechanical responses of the specimens is to reduce both the Young's modulus and the uniaxial yield stress in tension from their pretest characterization values. The magnitudes of the reduction are consistent with anticipated variability in tensile material properties. In subsequent discussions this material model is referred to as the adjusted model.

The adjusted material model incorporates adjustments to the unirradiated tensile characteristics of A 533 B (HSST Plate 13B) steel in the following manner. Within the linear-elastic region, the Young's modulus is reduced by 5% such that E = 196.5 GPa (28,500 ksi), since E had not been explicitly determined. The yield stress was arbitrarily reduced by 9% such that $\sigma_0$ = 413 MPa (59.9 ksi). A 9% variation in yield is reasonable based on the scatter of material properties. The adjusted yield strain is thus $\varepsilon_0$ = 0.0021, and Poisson's ratio remains $\nu$ = 0.3. The uniaxial engineering-stress, engineering-strain curve in tension beyond yield is the same as the unadjusted model. The

uniaxial true-stress, true-plastic-strain curve in tension for the adjusted model is also indicated in Fig. 6.

Minimal differences are observed between the stress-strain curves of these two material models when they are presented in the form indicated in Fig. 6. However, an indication of the relative plastic response of these two material models can be obtained with the stress-strain curves presented in the form indicated in Fig. 7. In Fig. 7, the instantaneous yield stress $\sigma$ is normalized by the initial yield stress $\sigma_0$. The effects of the differences between the two material models on analysis results are expected to become significant as the loading conditions in a specimen approach elastic-plastic behavior.

## 3.2 Finite-Element Models and Analysis Assumptions

The finite-strain, elastic-plastic posttest analyses are performed using the finite-element code ABAQUS.[21] The analyses assume a rate-independent, $J_2$ (isotropic-hardening) incremental plasticity theory as implemented in ABAQUS. The planform for both the shallow- and deep-flaw specimen is 102 by 610 mm (4 by 24 in.). The initial

ORNL-DWG 92-2879 ETD
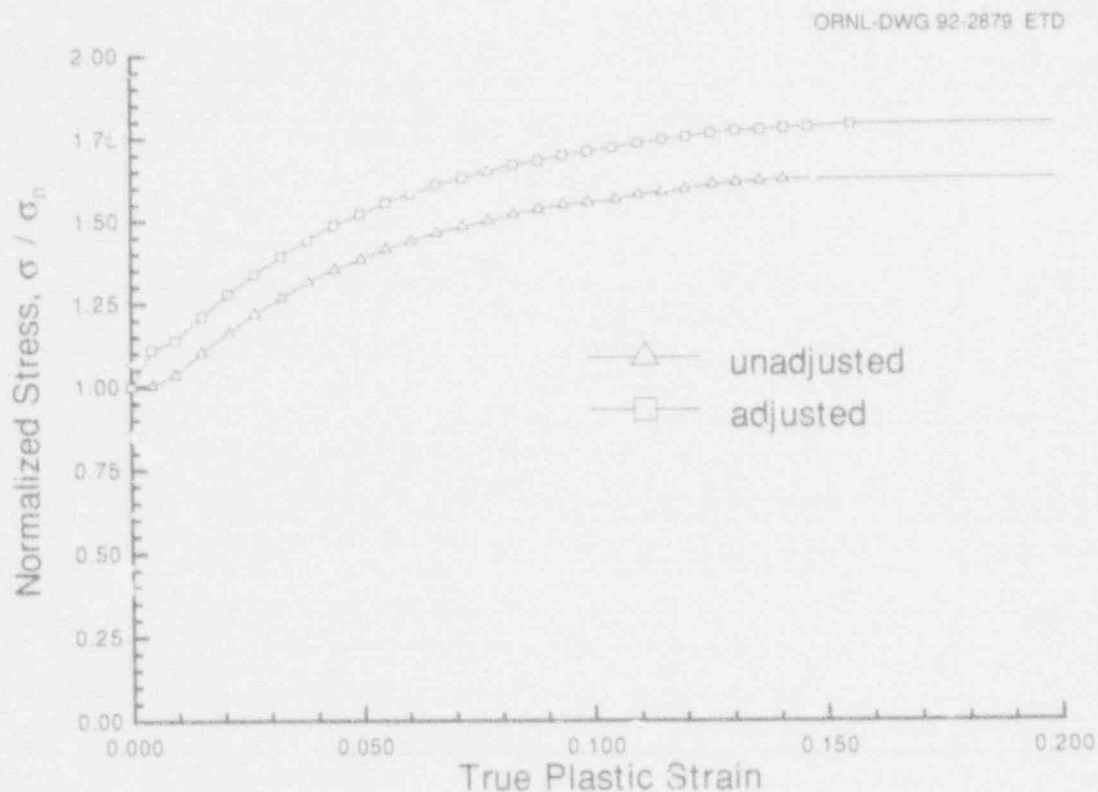


Figure 7 Normalized stress-strain curves for unadjusted and adjusted material models

flaw depth is 10.2 mm (0.4 in.) for the shallow-flaw specimen and 50.8 mm (2 in.) for the deep-flaw specimen. The shallow-flaw specimen geometry is modeled with the finite-element mesh indicated in Fig. 8(a)-(c), which is made up of 914 10-node generalized-plane-strain isoparametric elements with a total of 2883 nodes. The deep-flaw specimen geometry is modeled with the finite-element mesh indicated in Fig. 9(a)-(c), which is made up of 922 10-node generalized-plane-strain isoparametric elements with a total of 2903 nodes. These 10-node elements behave as conventional 8-node isoparametric elements except for an extra degree-of-freedom (DOF) that allows for uniform straining in a direction perpendicular to the plane of the mesh.[21] In a plane-strain analysis the out-of-plane DOF is not active. The integration order of the elements is $2 \times 2$.

A unique feature of the finite-element meshes is the highly refined crack-tip region. The rectangular crack-tip region in Figs. 8(a) and 9(a) is made up of 29 (shallow-flaw) or 31

(deep-flaw) "rings" of elements as indicated in Figs. 8(b) and 9(b). The mathematically sharp crack-tip profile associated with small-strain fracture analysis is replaced, in the present finite-strain context, with an initial root radius before the imposition of external loading as indicated in Figs. 8(c) and 9(c). The assumption of a finite value of the initial root radius is necessary to facilitate numerical convergence of the finite-element results. The magnitude of the initial root radius is $r_0 = 0.6$ μm (2.36 by $10^{-5}$ in.) for the shallow-flaw mesh, while for the deep-flaw mesh $r_0 = 1.3$ μm (5.03 by $10^{-5}$ in.). The high degree of mesh refinement is necessary to obtain an accurate determination of the crack-tip stress and strain fields ahead of the blunting notch tip. The proposed Q-stress parameter is determined based on crack-tip fields over such a region.

J-integral values are determined from up to 29 (shallow-flaw) or 31 (deep-flaw) paths surrounding the crack tip to verify path independence. A measure of the refinement of

ORNL-DWG 92-2880 ETD
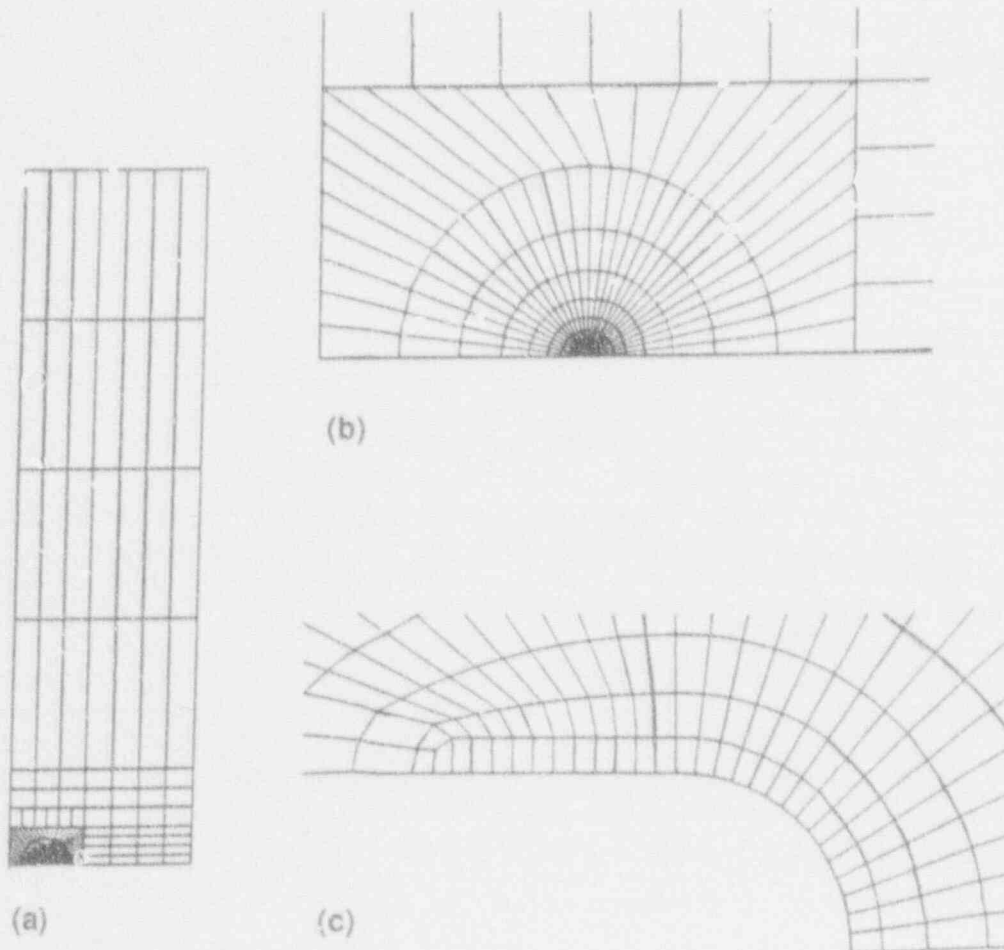


Figure 8 FEA mesh for a/W = 0.1

ORNL-DWG 92-2881 ETD
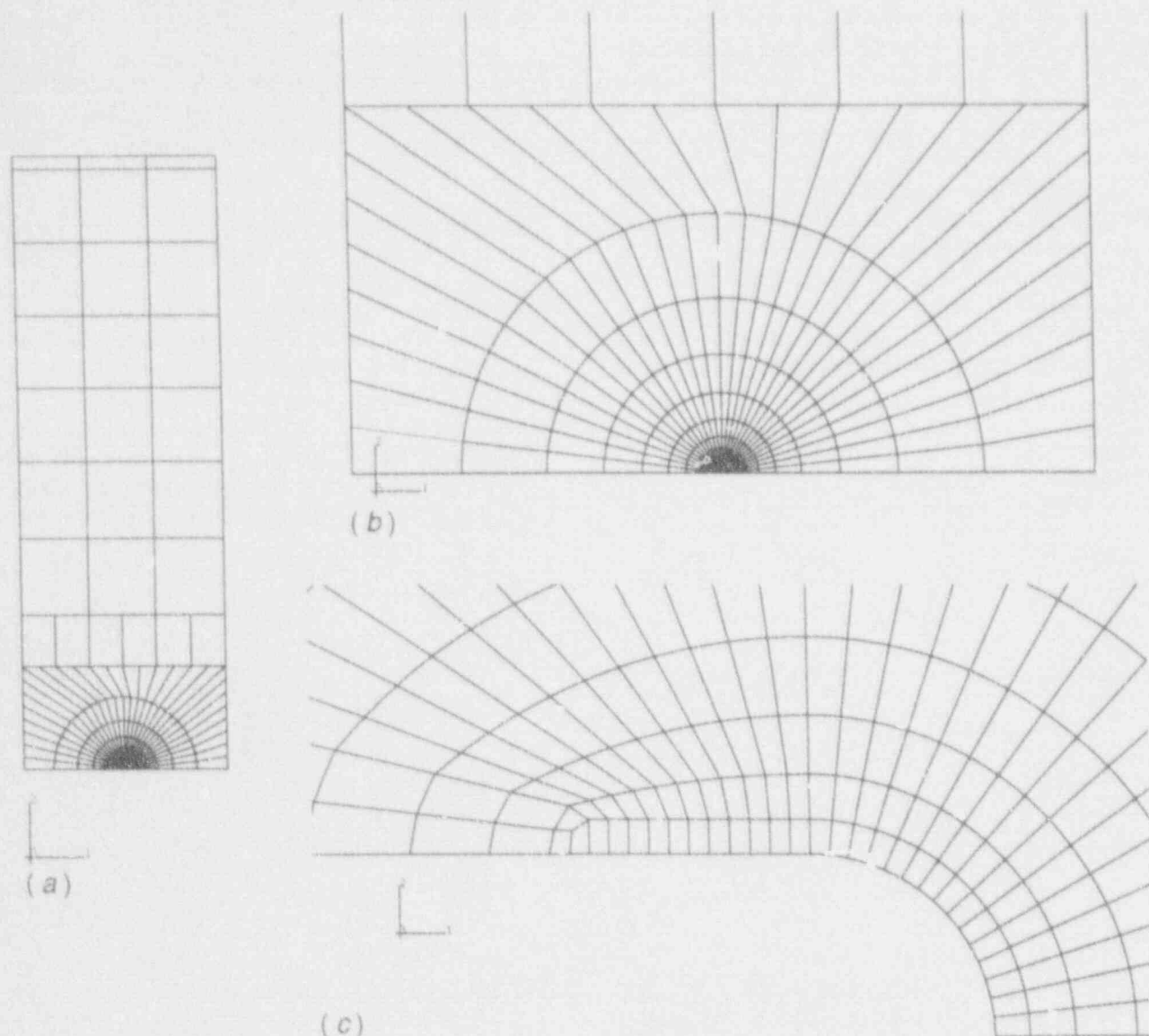


Figure 9 FEA mesh for a/W = 0.5

the meshes indicated in Figs. 8 and 9 is that the elastically determined K value using these meshes is within 99.5% of the reported value in the literature.[22] Convergence requirements of the elastic-plastic finite-element results to be presented are specified by means of limiting the maximum value of the residual nodal force per unit thickness at any node. Specifically, the maximum value is required to be <0.1% of the product between the yield stress and the smallest element dimension in the finite-element mesh.

## 3.3 Comparison of Calculated and Measured Mechanical Responses

Experimental measurements for the load (P), LLD, and CMOD are available for the six specimens considered in

these analyses. Comparison of the calculated and measured mechanical responses provides a means to gage the general accuracy of the analysis results and an additional basis for establishing confidence in the calculated fracture mechanics parameters. Comparison of the calculated and measured P-LLD response for the shallow-flaw specimens is indicated in Fig. 10, while an analogous comparison of the P-CMOD response is presented in Fig. 11. Similar comparisons for the deep-flaw geometry are presented in Figs. 12 and 13.

Figures 10 and 11 present two sets of calculated responses (LLD and CMOD, respectively) along with the measured responses for the three shallow-flaw specimens (beams 38, 37, and 26). The measured responses of these specimens

14

ORNL-DWG 92M-2682 ETD



Figure 10  P-LLD for a/W = 0.1

ORNL-DWG 92M-2883 ETD
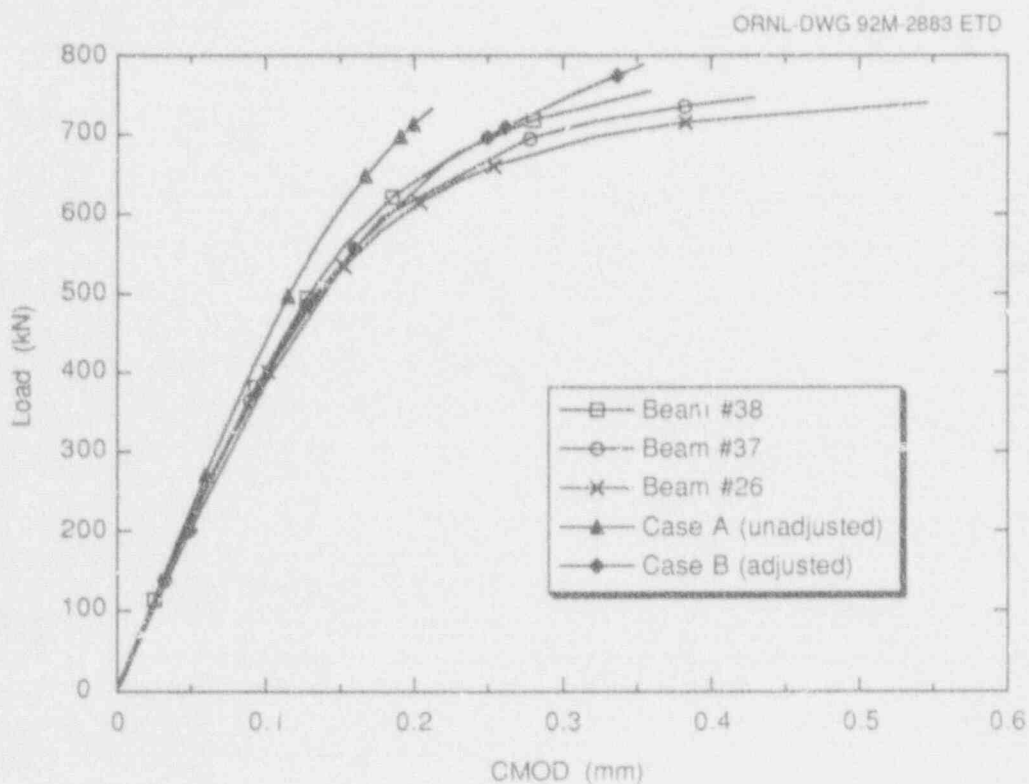


Figure 11  P-CMOD for a/W = 0.1

ORNL-DWG 92M-2884 ETD
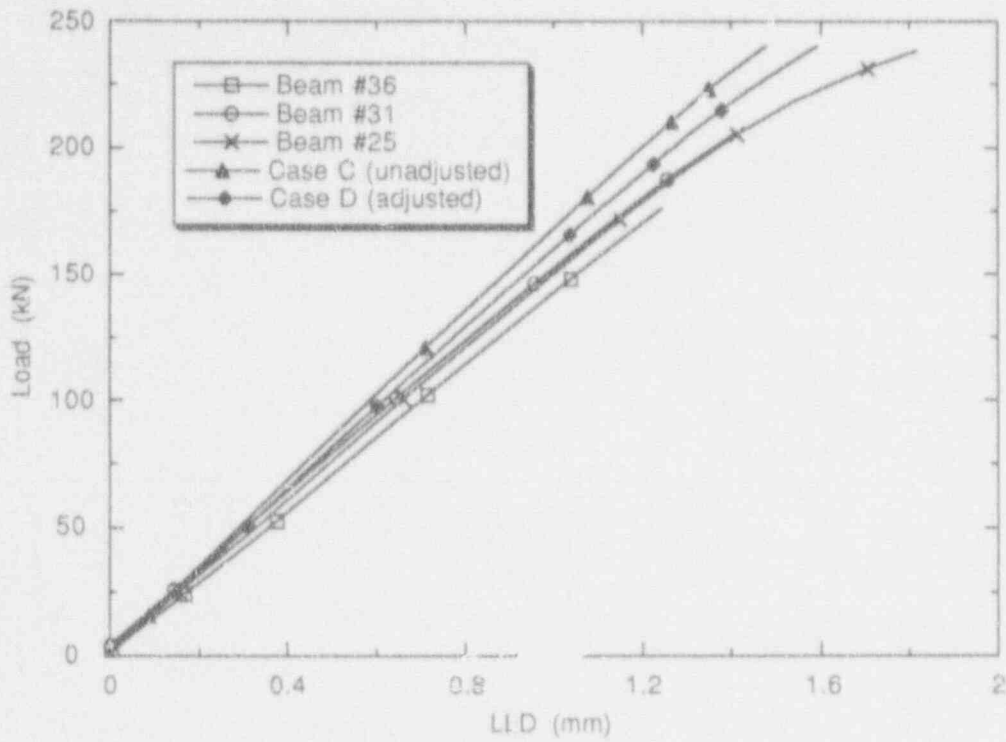


Figure 12  P-LLD for a/W = 0.5

ORNL-DWG 92M-2885 ETD
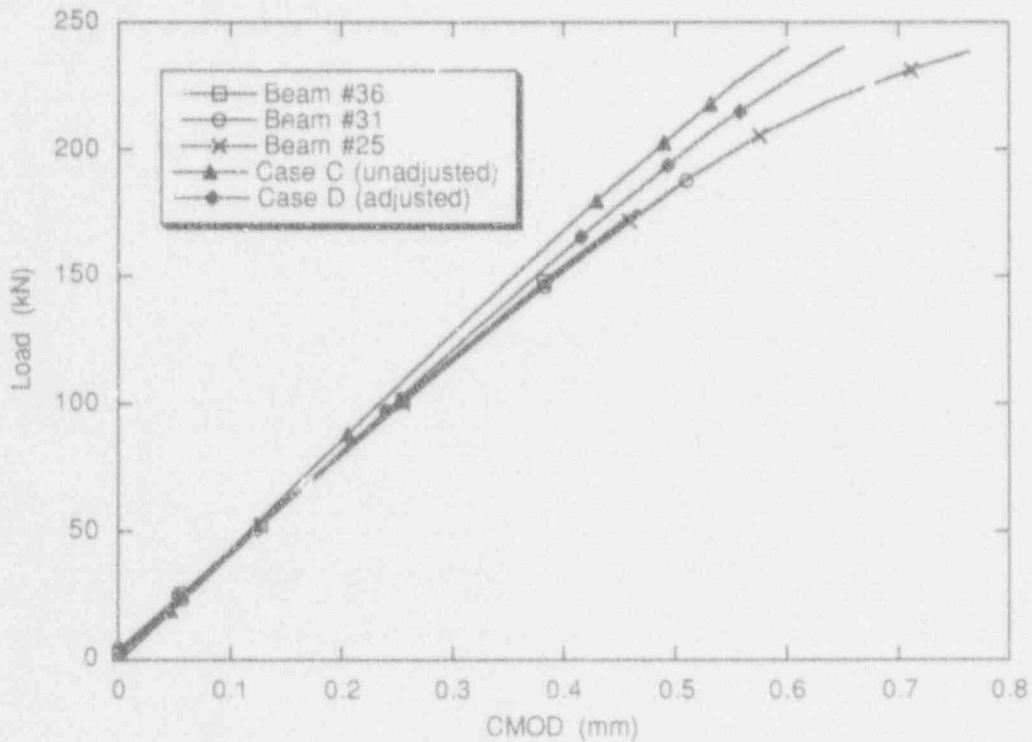


Figure 13  P-CMOD for a/W = 0.5

appear to indicate the presence of general yielding conditions at the onset of crack initiation. The two sets of calculated curves correspond to two cases of analysis conditions labeled as Cases A and B. The set of calculated P-LLD and P-CMOD curves corresponding to Case A were determined based on a/W = 0.1 and the unadjusted material model. The finite-element analysis was carried out under "load-control" because the reaction forces were specified along the back-side of the specimen ahead of the crack tip.

From Figs. 10 and 11 it is observed that at a given value of applied load the calculated LLD and CMOD responses are below the measured values both in the elastic and plastic regimes. Analysis options that have been attempted to reduce the stiffness of the finite-element models include reasonable adjustment of the material model and/or refinement of the flaw depth. Posttest examination of the fracture surfaces for the three shallow-flaw specimens, along nine locations on the crack front, indicates that the actual flaw depth is 10.8 mm (a/W = 0.106) rather than the assumed value of 10.2 mm (a/W = 0.10).

Analysis results for Case B were determined based on an actual flaw depth of a/W = 0.106 and the adjusted material model described previously. The finite-element analysis was carried out under "displacement-control" because displacements were specified along the back-side of the specimen ahead of the crack tip. As evident from Figs. 10 and 11, analysis conditions for Case B appear to result in better agreement between the calculated and measured mechanical responses both in the elastic and plastic regimes.

In Figs. 12 and 13, analysis results for Cases C and D, along with the measured responses for the three deep-flaw specimens (beams 36, 31, and 25), are presented. Analysis results for Case C corresponds to a/W = 0.5 and the unadjusted material model. Discrepancies are observed between results for Case C and the measured responses. Posttest examination of the fracture surfaces for the three deep-flaw specimens indicates that the actual flaw depth is 51.6 mm (a/W = 0.502) rather than the assumed value of 51 mm (a/W = 0.50) or an increase of only 1%. Analysis results for Case D were thus determined based on the nominal flaw depth of a/W = 0.50 and the adjusted material model. Both Cases C and D were carried out under "load-control." As evident from Figs. 12 and 13, analysis conditions for Case D appear to result in better agreement between the calculated and measured mechanical responses both in the elastic and plastic regimes.

## 3.4 Comparison of J-Integral Values from Finite-Element Analysis and J-Estimation Schemes

Fracture toughness is often expressed as the magnitude of the J-integral or the stress-intensity factor (K) at the onset of crack initiation. The J-integral values have been determined as a part of the posttest analysis of the specimens. In Fig. 14, the magnitude of the J-integral as a function of LLD is presented for the shallow-flaw geometry based on Case B conditions. The magnitude of critical values of P and LLD ($P_c$, $LLD_c$) for the three shallow-flaw specim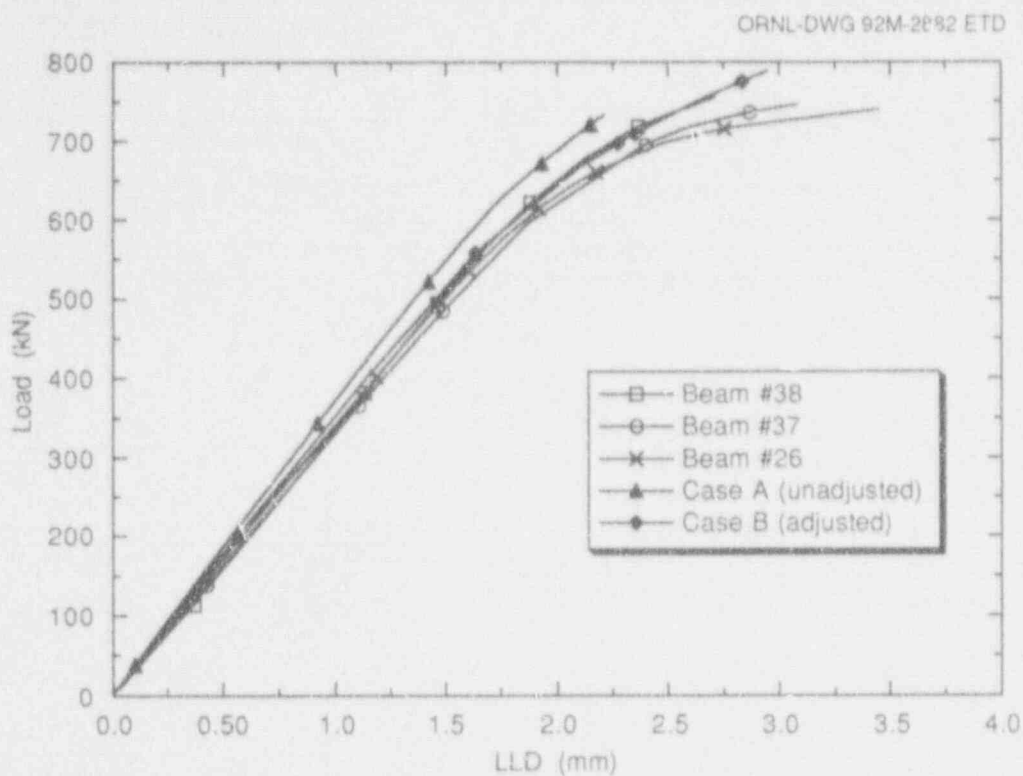ens at crack initiation are indicated in Table 4. The magnitude of the analytical J-integral based on attaining $LLD_c$ can be determined from the curve labeled as $J_{LLD}$ in Fig. 14. These J-integral values are denoted as $J_{LLD_c}$ and are listed in Table 4. Because the calculated P-LLD curve for the shallow-flaw specimen underestimates the measured value of LLD at a given value of P, $J_{LLD_c}$ can be regarded as an upper bound to the actual value of the J-integral at the onset of crack initiation. On the other hand, the magnitude of the J-integral based on attaining $P_c$ can be regarded as a lower bound to the actual value of the J-integral. These J-integral values are denoted as $J_{P_c}$ and are listed in Table 4. In terms of the stress-intensity factor, magnitudes of $K_{LLD_c}$ and $K_{P_c}$ are also listed in Table 4. Analogous results for the deep-flaw geometry based on Case D conditions are presented in Fig. 15 and in Table 5.

A measure of the shallow-flaw effect on toughness can be obtained based on the ratio of the lowest-calculated toughness between the shallow- and deep-flaw specimens. Specifically, lower-bound toughness enhancement in terms of $J_{LLD_c}$ is equal to 2.64, and in terms of $K_{LLD_c}$ is equal to

J-estimation schemes based on the magnitude of the experimentally determined LLD and CMOD for both the shallow- and deep-flaw geometry are presented in Chap. 2 and Appendix A. The J-integral values based on these estimation schemes, denoted as $J_{EXP}$, are indicated in Figs. 14 and 15 and listed in Tables 4 and 5. In terms of the stress-intensity factor, magnitudes of $K_{EXP}$ are also listed in Tables 4 and 5. The lower-bound toughness enhancement in terms of $J_{EXP}$ (LLD) is equal to 3.03, and in terms of $K_{EXP}$ (LLD) is equal to 1.74.

ORNL-DWG 92M-2886 ETD
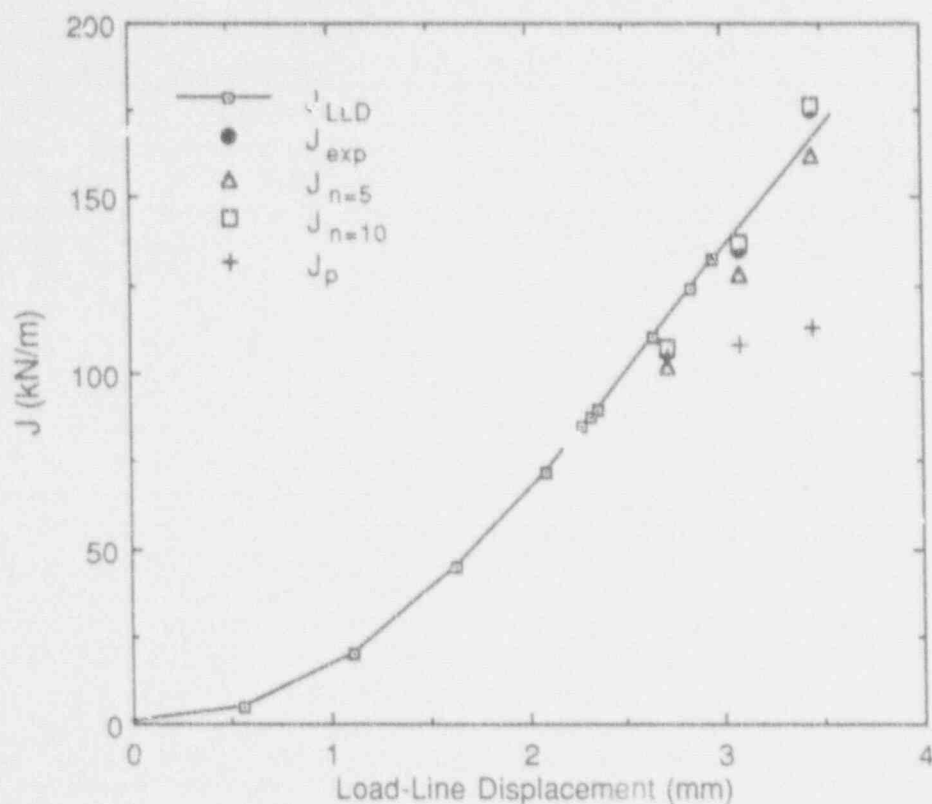


Figure 14 J-LLD for a/W = 0.1

Table 4 Experimental and analytical results of fracture toughness for the shallow-flaw
(a/W = 0.1) specimen based on Case B conditions

| Beam No. | $P_c$ (kN) | $LLD_c$ (mm) | $J_{LLD_c}$ (kN/m) | $J_{P_c}$ (kN/m) | $J_{exp}$ (kN/m) from LLD | $J_{exp}$ (kN/m) from CMOD |
|---|---|---|---|---|---|---|
| 38 | 756 | 2.71 | 115 | 112 | 106 | 127 |
| 37 | 746 | 3.08 | 142 | 108 | 135 | 160 |
| 26 | 740 | 3.45 | 169 | 1^5 | 175 | 217 |

| | | | $K_{LLD_c}$ (MPa·$\sqrt{m}$) | $K_{P_c}$ (MPa·$\sqrt{m}$) | $K_{exp}$ (LLD) (MPa·$\sqrt{m}$) | $K_{exp}$ (CMOD) (MPa·$\sqrt{m}$) |
|---|---|---|---|---|---|---|
| 38 | | | 158 | 138 | 151 | 162 |
| 37 | | | 175 | 139 | 171 | 182 |
| 26 | | | 190 | 142 | 194 | 212 |

Results in Figs. 14 and 15 indicate that values of $J_{EXP}$ calculated from measured values of LLD compare favorably with the finite-element results. The general accuracy of the LLD-based J-estimation scheme for the deep-flaw geometry is verified by the observation that all of the deep-flaw $J_{EXP}$ values are between $J_{LLD_c}$ and $J_{P_c}$ and clustered

about the $J_{LLD}$ curve. A similar degree of accuracy is observed for the case of the shallow-flaw geometry, although one of the $J_{EXP}$ values is slightly higher than the upper-bound $J_{LLD_c}$ value. The J-integral estimation scheme based on CMOD appears to overestimate the fracture toughness for shallow-flaw specimens because all

18

ORNL-DWG 92M-2887 ETD
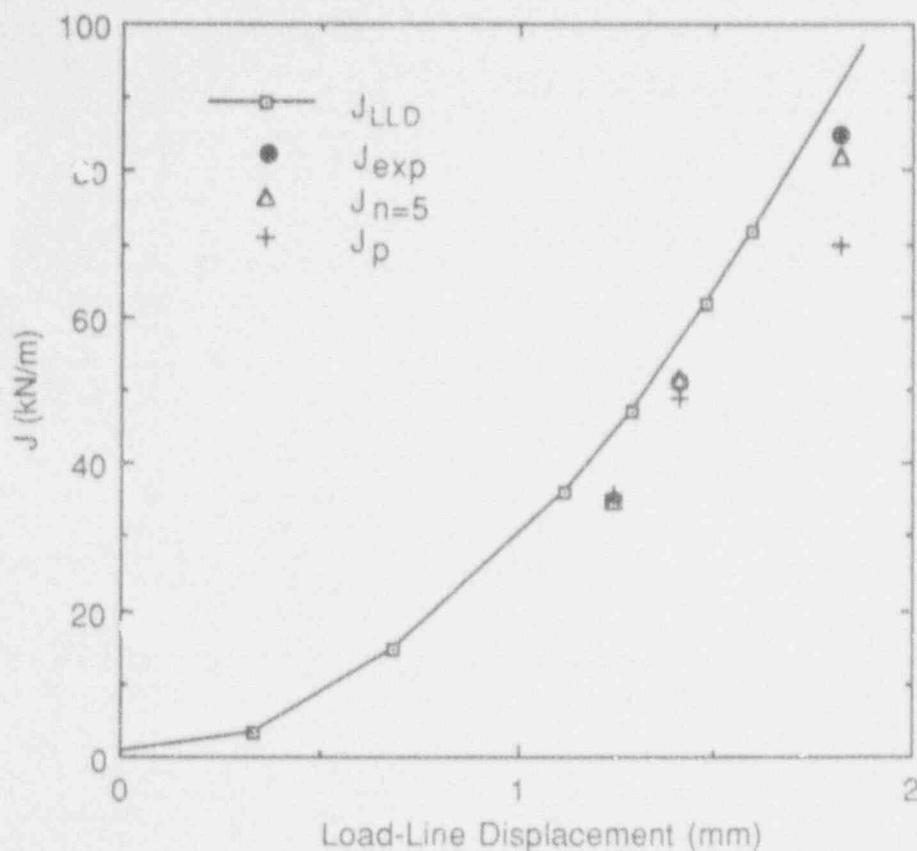


Figure 15 J-LLD for a/W = 0.5

Table 5 Experimental and analytical results for the fracture toughness for deep-flaw
(a/W = 0.5) specimens based on Case D conditions

| Beam No. | $P_c$ (kN) | $LLD_c$ (mm) | $JLLD_c$ (kN/m) | $JP_c$ (kN/m) | $J_{exp}$ (kN/m) from LLD | $J_{exp}$ (kN/m) from CMOD |
|---|---|---|---|---|---|---|
| 36 | 176 | 1.24 | 44 | 35 | 35 | 34 |
| 31 | 206 | 1.41 | 57 | 49 | 51 | 51 |
| 25 | 238 | 1.82 | 91 | 71 | 85 | 89 |

| | | | $K_{LLD_c}$ (MPa·$\sqrt{m}$) | $K_{P_c}$ (MPa·$\sqrt{m}$) | $K_{exp}$ (LLD) (MPa·$\sqrt{m}$) | $K_{exp}$ (CMOD) (MPa·$\sqrt{m}$) |
|---|---|---|---|---|---|---|
| 36 | | | 97 | 88 | 89 | 89 |
| 31 | | | 111 | 103 | 108 | 109 |
| 25 | | | 141 | 123 | 139 | 144 |

19

Posttest

values of $J_{EXP}$ (CMC) were above the upper-bound value of $J_{LLD_c}$.

As a further check on the evaluation methods, the J-integral values obtained using either the finite-element method or the CMOD-based J-estimation scheme can be compared with available results in the literature. Specifically, a J-estimation scheme based on plastic work determined from the experimental P-LLD record has recently been proposed for the SEN3 specimen geometry for a wide range of crack depths and strain hardening response.[*] In Fig. 14, the J-integral values based on this estimation scheme, for the case with Ramberg-Osgood strain-hardening coefficient n = 5 and 10, are denoted as $J_{n=5}$ and $J_{n=10}$. Unirradiated A 533 B is often identified with $5 \leq n \leq 10$. Good agreement between the plastic work-based J-integral values and $J_{LLD_c}$ and $J_{EXP}$ is observed. For the deep-flaw case of a/W = 0.5, J-integral values using the plastic work-based scheme are essentially independent of strain-hardening response. Consequently, only $J_{n=5}$ values are indicated in Fig. 15. Good agreement exists between the plastic work-based J-integral values of $J_{LLD_c}$ and $J_{EXP}$.

---

[*] M. T. Kirk and R. H. Dodds, Jr., "J and CTOD Estimation Equations for Shallow Cracks in Single Edge Notch Bend Specimens," Report No. UILU-ENG-91-2013, Department of Civil Engineering, University of Illinois at Urbana-Champaign, Urbana, Ill., January 1992.

## 3.5 Small-Scale Yielding Reference Crack-Tip Stress Fields

The two-parameter J-Q approach appears to provide a rigorous theoretical framework both to characterize the crack-tip fields and to provide a basis for interpreting and ordering experimentally determined fracture toughness values. The basis for this approach is a rather precise definition of crack-tip constraint based on the Q-stress parameter. A brief discussion on the definition of the Q-stress parameter, along with its linear elastic fracture-mechanics (LEFM) counterpart the T-stress parameter, is presented in Appendix B. In the case of the deep- and shallow-flaw specimens, the Q-stress parameter is defined as the difference between the "opening-mode" stress component obtained from a large-strain, plane-strain, finite-element analysis of the specimen and the corresponding stress component determined from the associated reference small-scale yielding (SSY) conditions. A brief discussion on the conditions of SSY and the related concept of boundary-layer analysis is presented in Appendix C.

The "opening-mode" stress component for the reference SSY problem, along the crack plane directly ahead of the blunting notch tip, is indicated in Fig. 16 for both the unadjusted and the adjusted material model. The stress component is normalized by the initial yield stress $\sigma_0$, and
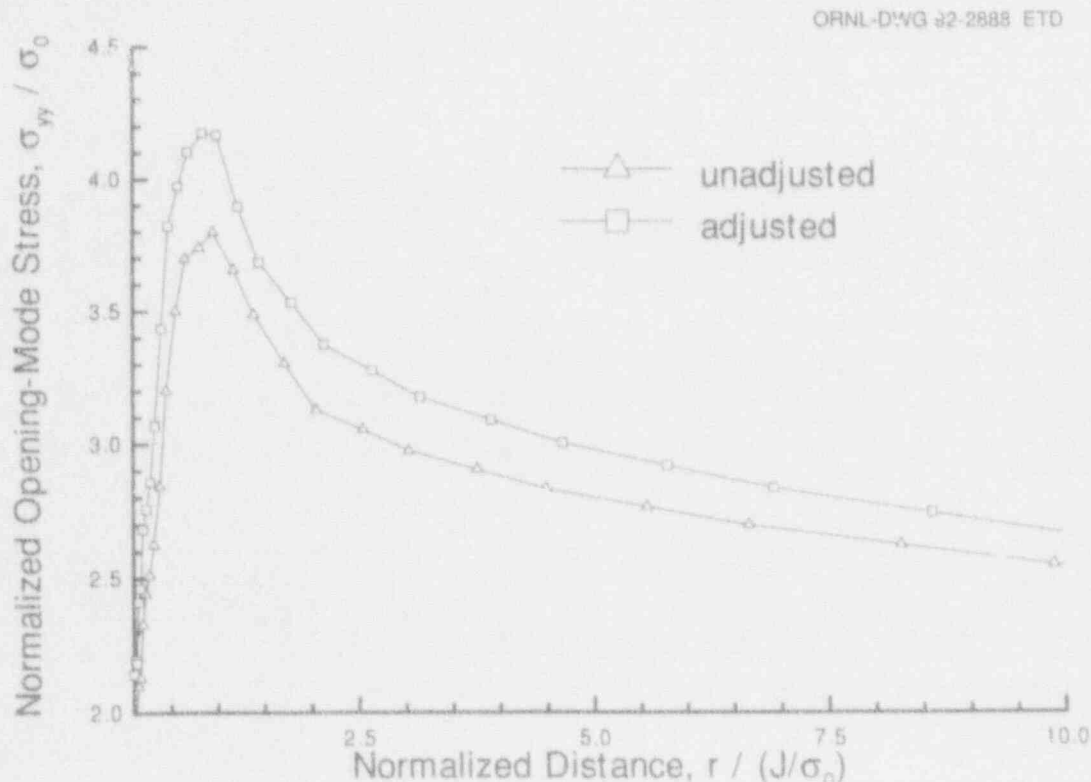
Figure 16 SSY distributions of opening-mode stress component for unadjusted and adjusted material models

distance ahead of the blunting notch tip is expressed in terms of the normalized distance parameter $r/(J/\sigma_0)$. With reference to Figs. 6 and 7, it is observed that the differences in the relative plastic response of these two material models are manifested in the observed differences in their respective SSY crack-tip fields. In Fig. 16 and subsequent figures, the "opening-mode" stress component is determined from averaged nodal values based on extrapolation from integration points of surrounding elements. The magnitude of the J-integral can be obtained using the standard plane-strain conversion between J and K based on the applied value of K in the SSY analysis. Alternately, the J-integral can be obtained using the J-integral option provided by ABAQUS. Excellent agreement is found between these two methods of evaluating the J-integral, thus providing an avenue for verifying the numerical accuracy of the finite-element results.

## 3.6 Shallow- and Deep-Flaw Specimen Crack-Tip Stress Fields

Distributions of the "opening-mode" stress component for the shallow-flaw geometry, along the crack plane directly ahead of the blunting notch tip, are indicated in Fig. 17 for various stages of loading based on Case B conditions. The loading stages are expressed in terms of the magnitude of the applied load as deduced from the finite-element results (recall the analysis was performed under displacement control). From Table 4, the experimentally determined critical values of the applied load ($P_c$) for the three specimens are 740, 746, and 756 kN. Also indicated in Fig. 17 is the SSY distribution for the specimen material based on the adjusted material model. The stress component is normalized by the initial yield stress $\sigma_0$, and distance ahead of the blunting notch tip is expressed in terms of the normalized distance parameter $r/(J/\sigma_0)$, where J is the value of the J-integral associated with the specified loading conditions. Analysis results in Fig. 17 indicate that the crack-tip fields in the shallow-flaw specimen progressively deviate from the SSY distributions as the specimens are loaded toward the onset of crack initiation. Crack initiation for the three shallow-flaw specimens occurred under substantially non-SSY conditions.

Analogous results for the "opening-mode" stress distributions for the deep-flaw geometry are indicated in Fig. 18. As shown in Table 5, the magnitudes of $P_c$ for the three specimens are 176, 206, and 238 kN. Analysis results in Fig. 18 indicate that crack initiation for the three deep-flaw specimens occurred under essentially SSY conditions.
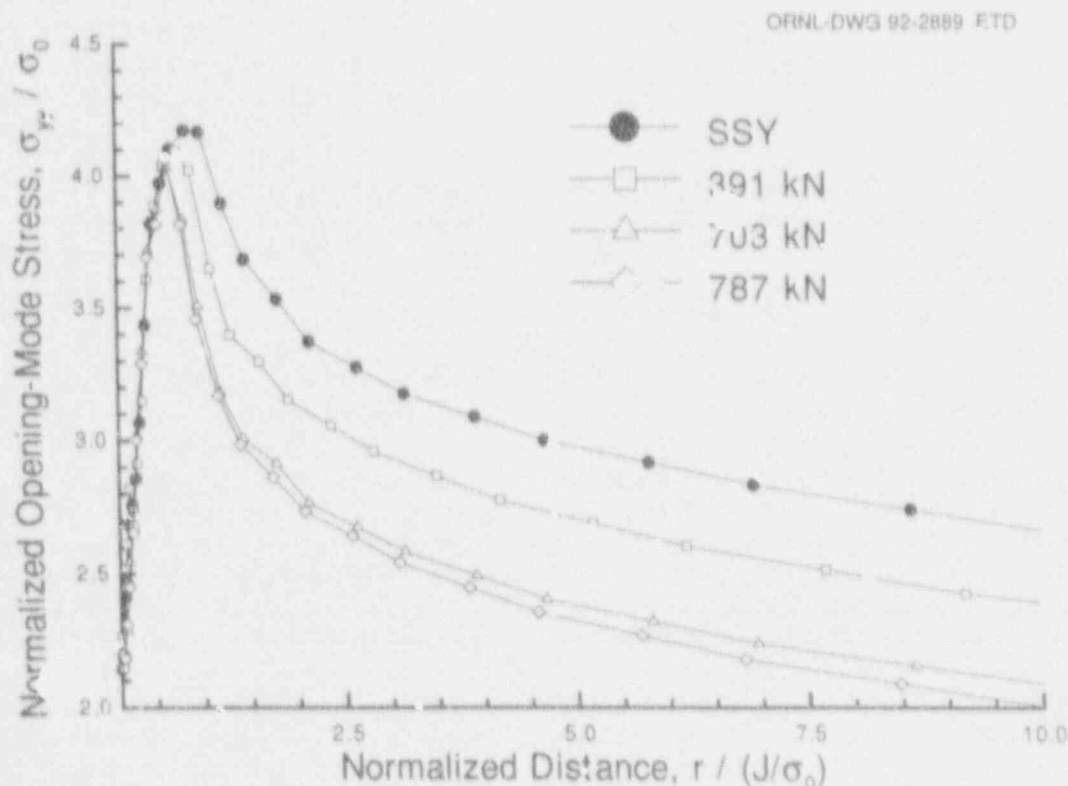
Figure 17 Distributions of opening-mode stress component for a/W = 0.1 as a function of applied load up to crack initiation

21

ORNL-DWG 92-2890 ETD
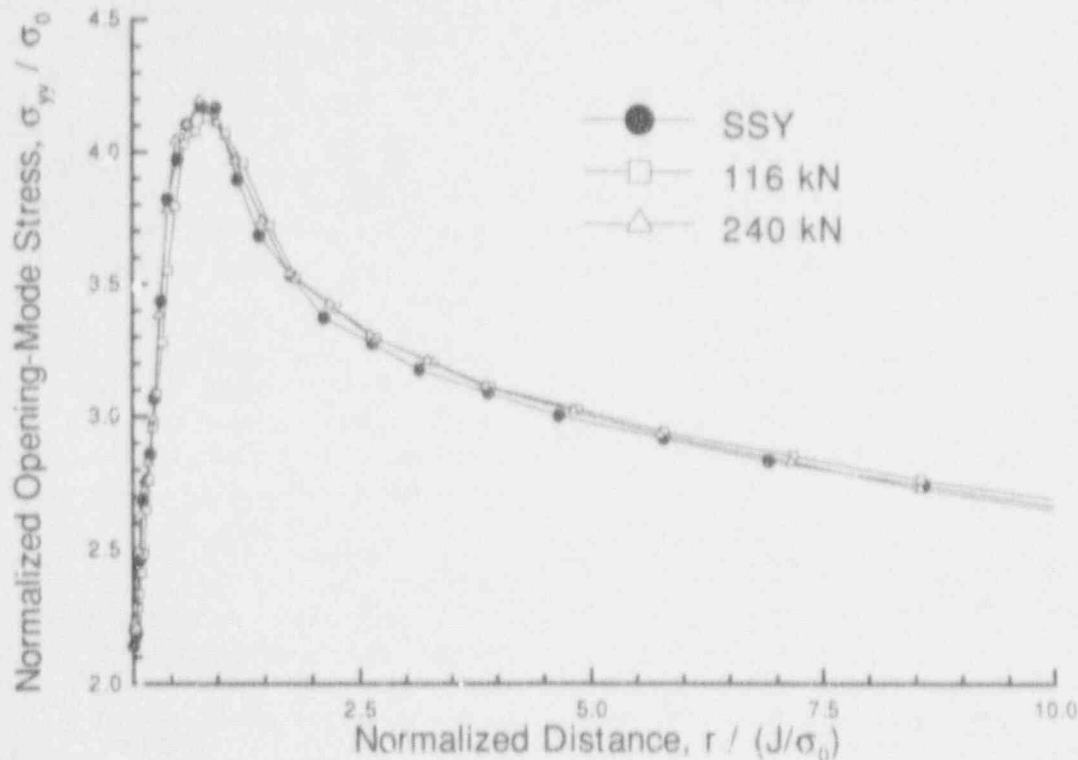


Figure 18 Distributions of opening-mode stress component for a/W = 0.5 as a function of applied load up to crack initiation

## 3.7 Correlation of Deep- and Shallow-Flaw Toughness in Terms of $J_c(Q)$ Locus

The primary objectives of these analyses are to evaluate the utility of the recently proposed two-parameter J-Q concept to characterize the crack-tip fields up to the onset of crack initiation and provide a framework for interpreting and ordering the observed toughness differences between the deep- and shallow-flaw geometries. Analysis results for the shallow- and deep-flaw specimens appear to support the J-Q concept and interpretation method in the following sense. First, results from Figs. 17 and 18 indicate that the Q-stress parameter can be defined for the six specimens up to the onset of crack initiation. Crack initiation for the deep-flaw specimens occurred under conditions of $Q_c \approx 0$; for the shallow-flaw specimens crack initiation occurred under conditions of $Q_c \approx -0.7$. Second, the observed toughness variation between the shallow- and deep-flaw specimens can be ordered via the Q-stress parameter. Correlation of toughness for the shallow- and deep-flaw specimens in terms of critical values of $J_{LLD_c}$ ($J_c$) and the Q-stress ($Q_c$) is indicated in Fig. 19. The absence of toughness elevation for the deep-flaw specimens ($Q_c \approx 0$) relative to pretest characterization data is consistent with the

adoption of the Q-stress parameter as a measure of deviation from plane-strain constraint ($Q_c = 0$) as discussed in Appendix C. Increase in toughness for the shallow-flaw specimens relative to the deep-flaw specimens is associated with a nontrivial, negative value of the Q-stress parameter. The results in Fig. 19 are consistent with reported trends on the effects of Q-stress on the $J_c(Q)$ toughness locus for other types of steels.[23],[*] However, recent reanalysis of the ORNL wide-plate series using 2-D, J-Q techniques resulted in a different set of $J_c(Q)$ toughness data than that for the shallow-crack tests.

Interpretation and application of the $J_c(Q)$ toughness locus indicated in Fig. 19 also needs to take into account the following observations concerning the current definition of the Q-stress. In view of the Q-stress parameter's role as a crack-tip field-intensity parameter, determination of the magnitude of the Q-stress parameter based on differences of stress distributions at a *single location* ahead of the crack tip is perhaps unnecessarily restrictive both from a numerical and physical standpoint. Indeed, while the Q-stress is defined and evaluated at $r/(J/\sigma_0) = 2$ in this

---

[*] C. F. Shih, N. P. O'Dowd, and M. T. Kirk, "A Framework for Quantifying Crack Tip Constraint," presented at the ASTM Symposium on Constraint Effects in Fracture, Indianapolis, Ind., May 8–9, 1991.

ORNL-DWG 92M-2891 ETD
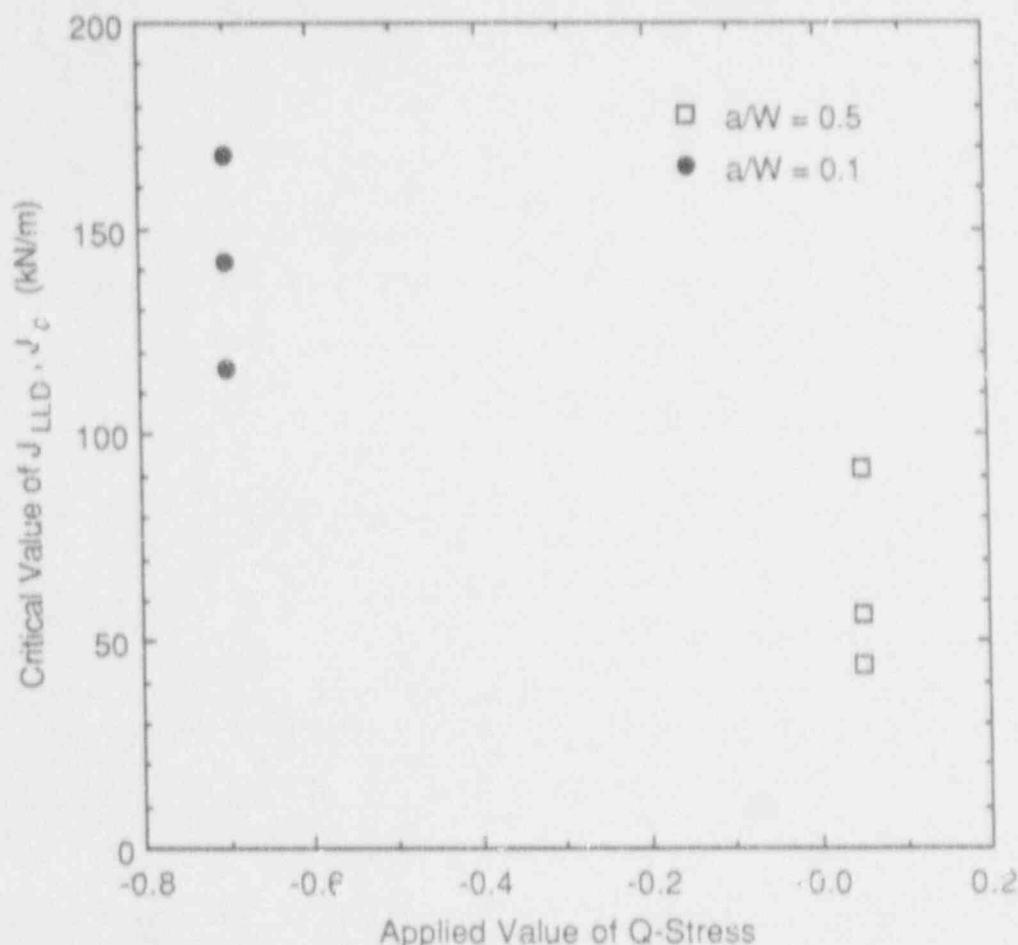


Figure 19  Correlation of $J_c$ with Q for six specimens

study, the differences between the reference SSY distribution and the distribution for the three specimens at various stages of loading are essentially uniform over a distance of $2 \leq r/(J/\sigma_0) \leq 10$. Numerically, it needs to be emphasized that finite-element results for stress components at a given mesh location, while accurate within the analysis context, are often averaged or extrapolated values and are thus mildly mesh-dependent. In this study these stress values are averaged nodal values extrapolated from integration locations. The results in Figs. 17 and 18 appear amendable to a more relaxed definition of the Q-stress, and hence $Q_c$, based on averaged differences of stress distributions over a limited range of distances ahead of the crack tip, for example, in the range of $2 \leq r/(J/\sigma_0) \leq 5$.

Regardless of whether the Q-stress is determined at a single location or over a region, an important consideration in

determining the utility of the Q-stress parameter is the range of *physical* distances over which the Q-stress parameter is determined. In the case of the adjusted material model, the magnitude of the parameter $J/\sigma_0$ at the onset of crack initiation for the deep- and shallow-flaw specimens based on $J_{LLD_c}$ falls in the range 87 $\mu$m $\leq$ $J_{LLD_c}/\sigma_0 \leq 407$ $\mu$m. The average grain size for HSST Plate 13A, a companion plate to HSST Plate 13B, is on the order of 20 to 30 $\mu$m.[15] Thus, it appears that the Q-stress parameter at the onset of crack initiation for these specimens is evaluated over physically meaningful distances that are consistent with the underlying continuum analysis assumptions.

# 4 RPV Analysis

This chapter presents detailed 2-D plane-strain analysis results for an RPV with an inner-surface axial flaw subject to a postulated PTS transient. The PTS transient simulates the pressure-temperature history of an RPV in a PWR during a small-break-loss-of-coolant accident (SBLOCA). The primary objectives of these analyses are to (1) evaluate the utility of the two-parameter J-Q approach to characterize the crack-tip fields in an RPV throughout a PTS transient and (2) present a methodology that incorporates small-specimen $J_c(Q,T)$ toughness locus data in the safety-margin assessment of an RPV.

## 4.1 Material Models

Three material models that simulate a wide range in the tensile properties of RPV-grade materials have been considered. The first material model simulates the unirradiated tensile properties of A 533 B steel plate (HSST Plate 13B) at $-40°C$ ($-40°F$) and can be considered as a lower-shelf-temperature material model. This material model is identical to the unadjusted material model discussed in Chap. 3. The uniaxial true-stress, true-plastic-strain curve in tension

is indicated in Fig. 20. In subsequent discussions this material model is referred to as Case 1.

The second material model simulates the unirradiated tensile properties of A 533 B steel plate (HSST Plate 13A) at 180°C (356°F) and can be considered an upper-shelf-temperature material model.[15] As discussed in Chap. 2, HSST Plates 13A and 13B are companion plates of A 533 B material. The linear-elastic portion of the true-stress, true-strain curve is characterized by a yield strain of magnitude $\varepsilon_0 = \sigma_0/E = 0.002$, where the Young's modulus $E = 196.9$ GPa (28,564 ksi), the uniaxial yield stress in tension $\sigma_0 = 390$ MPa (56.6 ksi), and Poisson's ratio $\nu = 0.3$. The uniaxial true-stress, true-plastic-strain curve in tension is modeled in a multilinear fashion as indicated in Fig. 20. In subsequent discussions this material model is referred to as Case 2.

The third material model simulates the irradiation-embrittled tensile properties of A 533 B (HSST Plate 13A).[24,25] The linear-elastic portion of the true-stress, true-strain
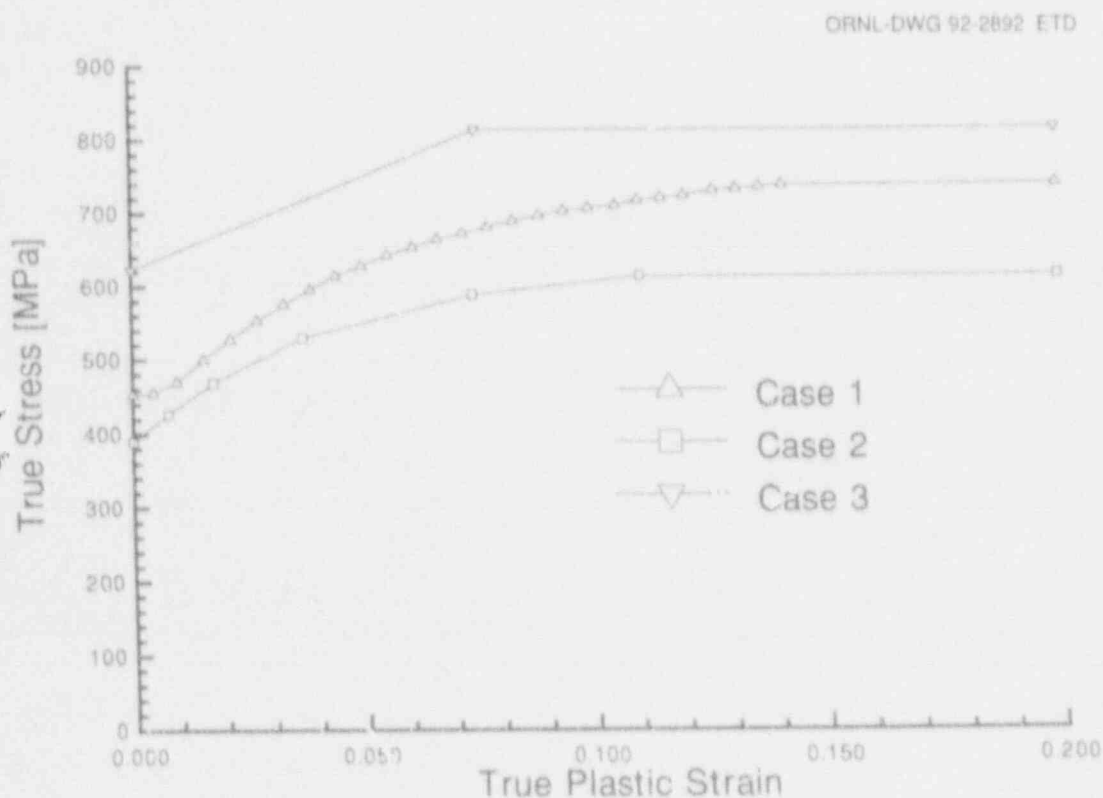
Figure 20 Uniaxial true stress–true plastic strain curve in tension for Cases 1, 2, and 3

curve is characterized by a yield strain of magnitude $\varepsilon_0 = \sigma_0/E = 0.0032$, where the Young's modulus $E = 193.1$ GPa (28,000 ksi), the uniaxial yield stress in tension $\sigma_0 = 621$ MPa (90 ksi), and Poisson's ratio $v = 0.3$. The uniaxial true-stress, true-plastic-strain curve in tension is modeled in a bilinear fashion as indicated in Fig. 20. In subsequent discussions this material model is referred to as Case 3.

An indication of the relative plastic response of these three material models can be obtained with the stress-strain curves presented in the form indicated in Fig. 21. In Fig. 21, the instantaneous yield stress is normalized by the initial yield stress $\sigma_0$. Analysis results to be presented indicate that the fracture response of the RPV under Case 3 conditions is significantly different than either Cases 1 or 2.

## 4.2 Finite-Element Model and Analysis Assumptions

The RPV being considered in this study has an inner radius of 1384 mm (54.5 in.) and a wall thickness of 200 mm (7.875 in.). The effects of a thin layer of stainless steel cladding, deposited on the inner surface of the RPV, on the thermal-mechanical response of the vessel is not considered. A 2-D inner-surface axial flaw with a depth of 10.2 mm (0.4 in.) is assumed to exist in this vessel before the onset of the PTS transient to be described shortly. In the terminology of small-specimen testing, the axial flaw is characterized by a flaw-depth to wall-thickness ratio $a/W = 0.05$.

The finite-strain, elastic-plastic nature of the RPV analyses are performed using the finite-element code ABAQUS.[21] The analyses assume a rate-independent, $J_2$ (isotropic-hardening) incremental plasticity theory as implemented in ABAQUS. The RPV geometry is modeled with the finite-element mesh (indicated in Fig. 22) that is made up of 1112 10-node generalized-plane-strain isoparametric elements with a total of 3511 nodes. The integration order of the elements is $2 \times 2$. Values of the J-integral as a function of the PTS transient are determined from up to 31 paths surrounding the crack tip to verify path independence. Similar to the finite-element models presented in Chap. 3, a unique feature of the finite-element mesh for the RPV is the highly refined crack-tip region. The rectangular crack-tip region is made up of 31 "rings" of elements. The magnitude of the initial root radius is $r_0 = 0.26$ µm ($1 \times 10^{-5}$ in.). The high degree of mesh refinement is necessary to obtain an accurate determination of the crack-tip fields ahead of the blunting notch tip.



ORNL-DWG 92-2893 ETD
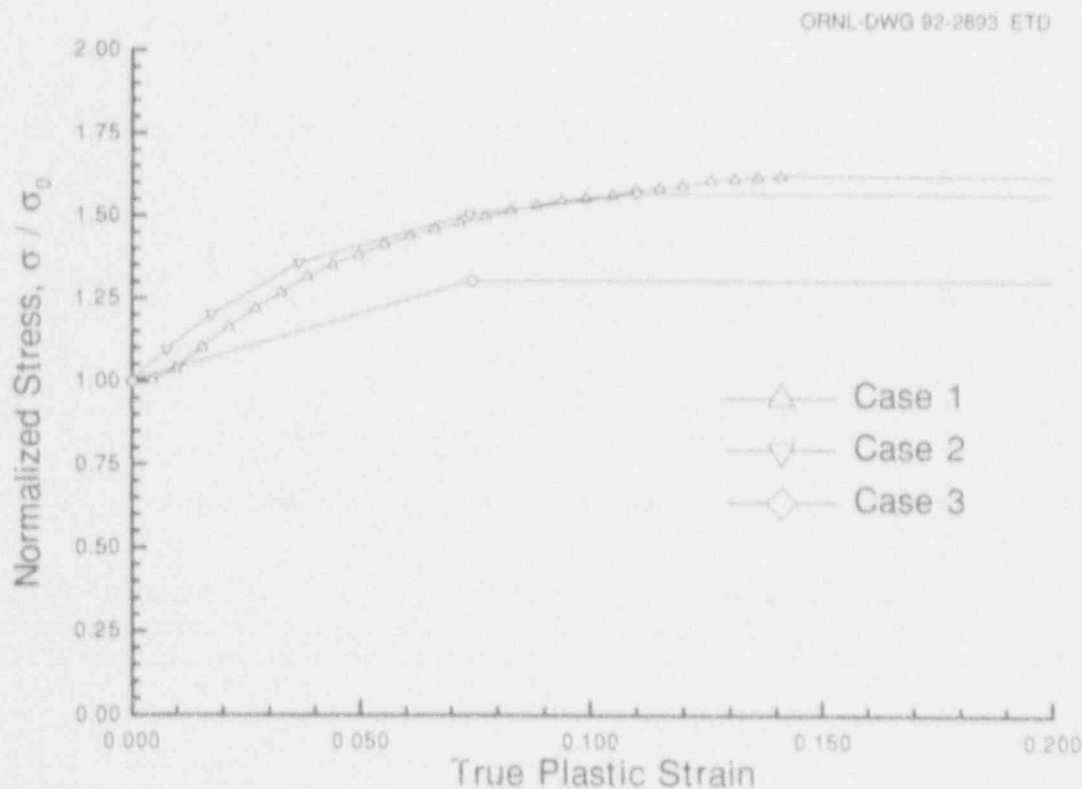
Figure 21 Normalized stress-strain curves for unadjusted and adjusted material models

ORNL-DWG 92-2894 ETD



(a)

(b)
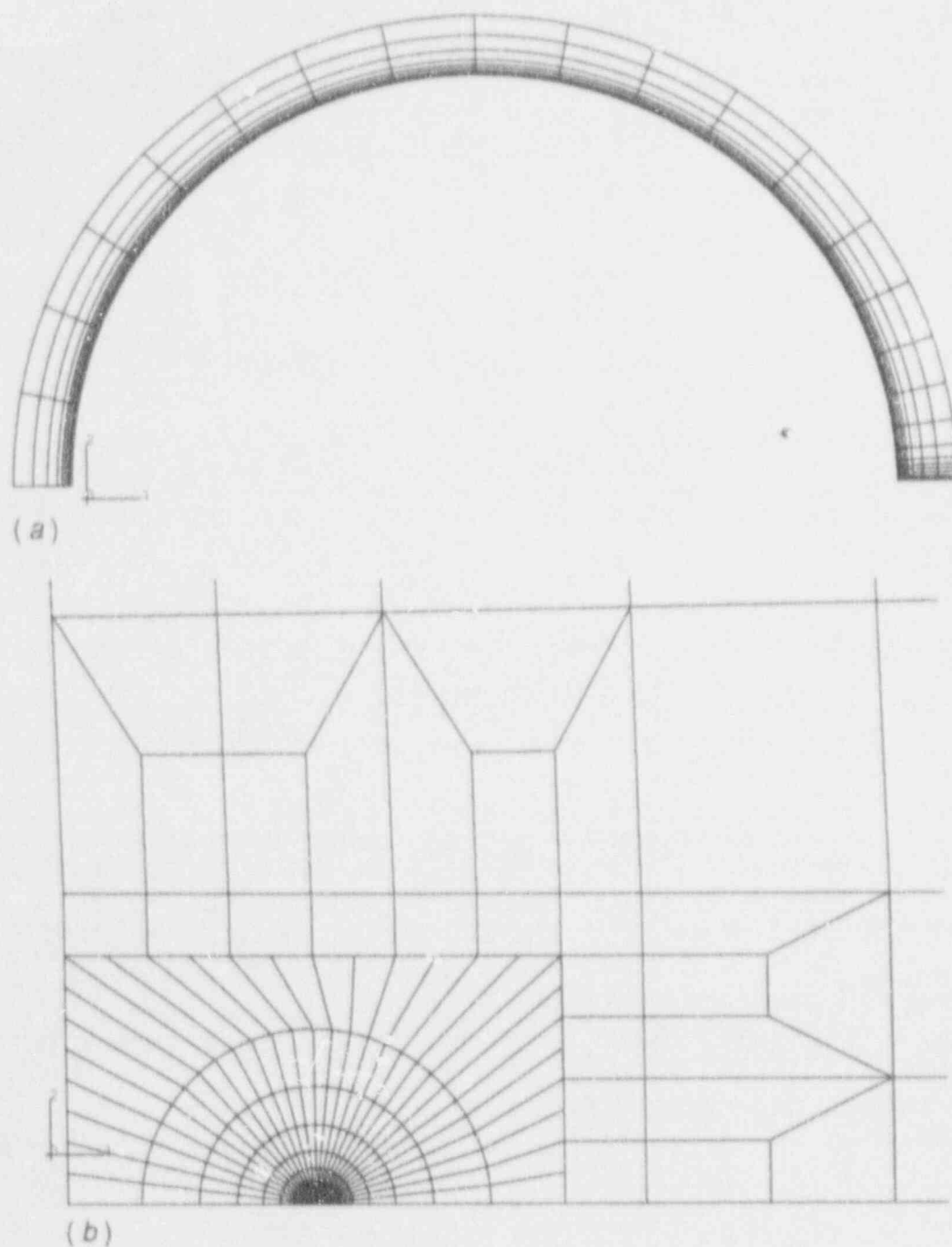
Figure 22 FEA mesh for RPV

The PTS transient being considered is indicated in Fig. 23. The PTS transient simulates the pressure-fluid temperature history of a PWR-RPV during an SBLOCA. The operating pressure and temperature of the RPV before the onset of the transient are 14.1 MPa (2050 psi) and 268°C (515°F), respectively.

Analysis of the fracture response of the RPV, in which the temperature-dependence of material properties was neglected, has been performed based on the three material models described previously. Recall that these material models simulate the tensile properties of RPV-grade materials in the unirradiated lower-transition, unirradiated

27
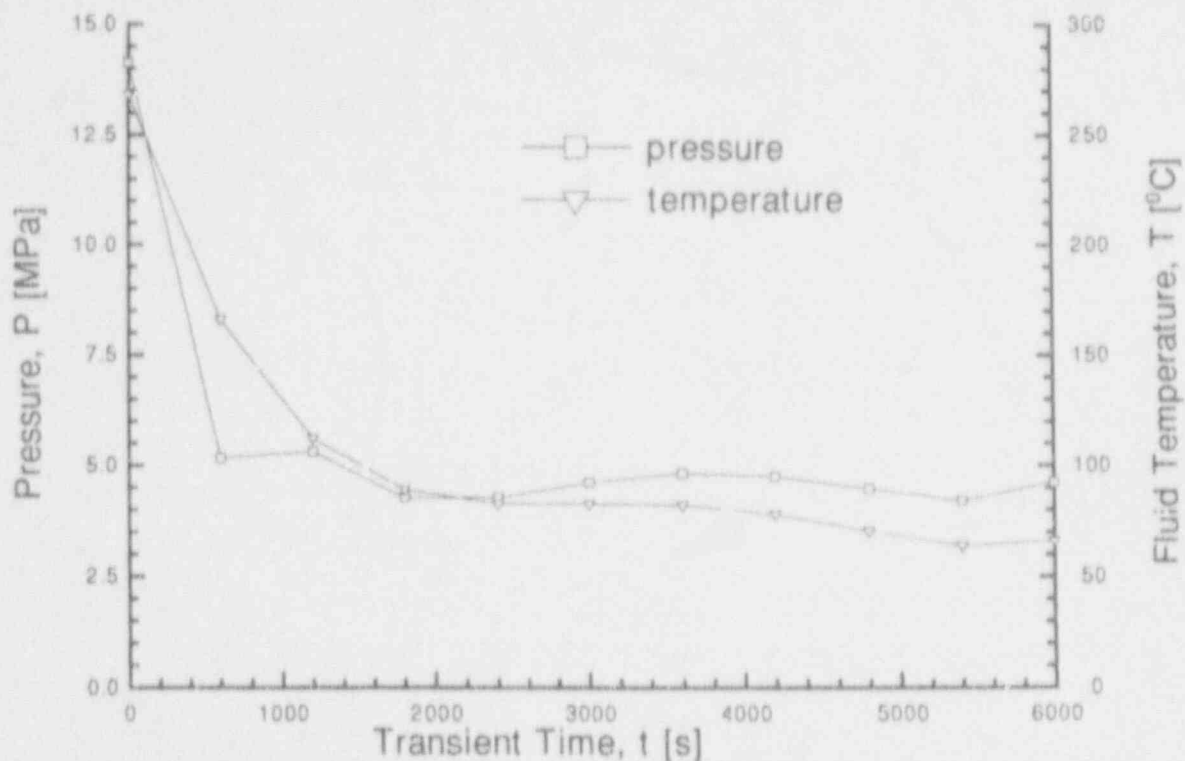
Figure 23 SBLOCA pressure and bulk coolant temperature (P-T) history

upper-shelf, and irradiation-embrittled conditions. The range of material properties represented by the three material models is believed to be sufficiently broad to simulate material responses in operating vessels.

## 4.3 Effects of PTS Loading on the RPV in Terms of J-Integral Values

Effects of the PTS loading on the RPV, in terms of the value of the applied J-integral as a function of transient time up to ~1200 s, are shown in Fig. 24 for the three material models. The magnitude of the J-integral increases monotonically with transient time up to ~1200 s; unloading of the crack tip as characterized by a decrease in the magnitude of the J-integral occurs after that time. Note that the time at which unloading occurs is independent of the material model adopted in the analysis. The magnitude of the J-integral at operating conditions ($J_{op}$), and its maximum value at ~1200 s into the transient ($J_{max}$), are listed in Table 6 for the three material models.

From Fig. 24 and Table 6, it is observed that the effects of the PTS loading on the RPV, when expressed solely in terms of the value of the J-integral, are relatively insensi-

tive to the material model adopted in the analysis. Recall that each of the analyses was performed assuming temperature-independence of tensile material properties during the transient. Consequently, this relative insensitivity suggests that the analysis results, in terms of the value of the J-integral as a function of transient time, would not be significantly different if detailed accounting of the temperature-dependence of tensile material properties had been considered.

## 4.4 SSY Reference Crack-Tip Stress Fields

As discussed in Chap. 3 and in Appendixes B and C, the basis of the J-Q approach is a definition of crack-tip constraint based on the Q-stress parameter. In the context of the present RPV analysis, the Q-stress parameter is defined as the difference between the "opening-mode" stress component obtained from a large-strain, plane-strain, finite-element analysis of the RPV and the corresponding stress component from the associated reference SSY problem. A boundary-layer approach using the finite-element code ABAQUS, assuming a rate-independent, $J_2$ (isotropic-hardening) incremental plasticity theory, is adopted in evaluating the reference SSY crack-tip fields.

ORNL-DWG 92-2R96 ETD
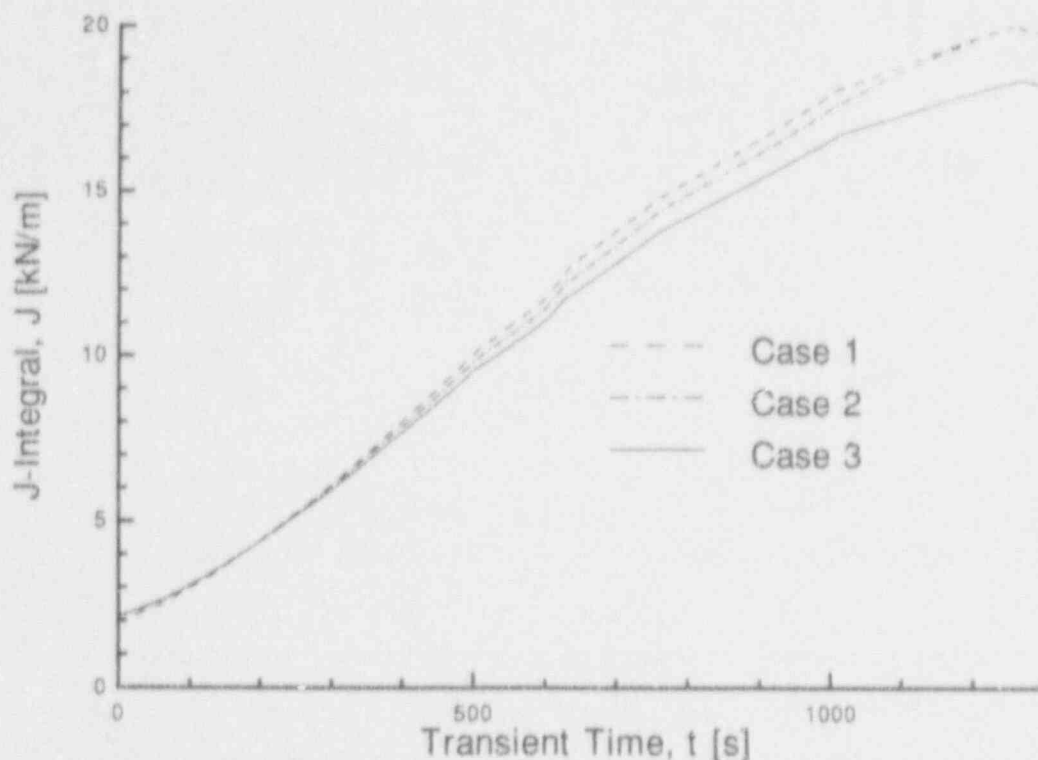


Figure 24 J-integral values as a function of time for Cases 1, 2, and 3

Table 6 Magnitude of the J-integral at operating conditions ($J_{op}$) and its maximum value ($J_{max}$) at ~1200 s into the transient for Cases 1, 2, and 3

| Model | $J_{op}$ (kN/m) | $J_{max}$ at ~1200 s (kN/m) |
|---|---|---|
| Case 1 | 2.05 | 20.3 |
| Case 2 | 2.14 | 19.5 |
| Case 3 | 2.2 | 17.9 |

The "opening-mode" stress component for the reference SSY problem, along the crack plane directly ahead of the blunting notch tip, is shown in Fig. 25 for Cases 1, 2, and 3. Figures 20 and 21 show that the differences in the relative plastic response of these three material models are manifested in the observed differences in their respective SSY crack-tip fields.

## 4.5 RPV Crack-Tip Stress Fields Under PTS Conditions

Distributions of the "opening-mode" stress component for the RPV based on the Case 1 material model, along the crack plane directly ahead of the blunting notch tip, are indicated in Fig. 26 for various times during the transient up to ~1200 s. The stress distribution associated with the RPV's operating pressure and temperature is labeled as t = 0 s. Also indicated in Fig. 26 is the SSY distribution for the Case 1 material model shown in Fig. 25.

Analysis results in Fig. 26 indicate that the crack-tip fields in the RPV have deviated from the SSY distribution even under operating conditions. The extent of the deviation from SSY conditions increases as the transient progresses through time. These results indicate that should crack initiation occur in the neighborhood of 1200 s into the transient, it would do so under substantially non-SSY conditions. The effects of unloading on the crack-tip fields that occurs for transient times greater than 1200 s, will be discussed shortly in conjunction with the Case 3 material model.

ORNL-DWG 92-2897 ETD
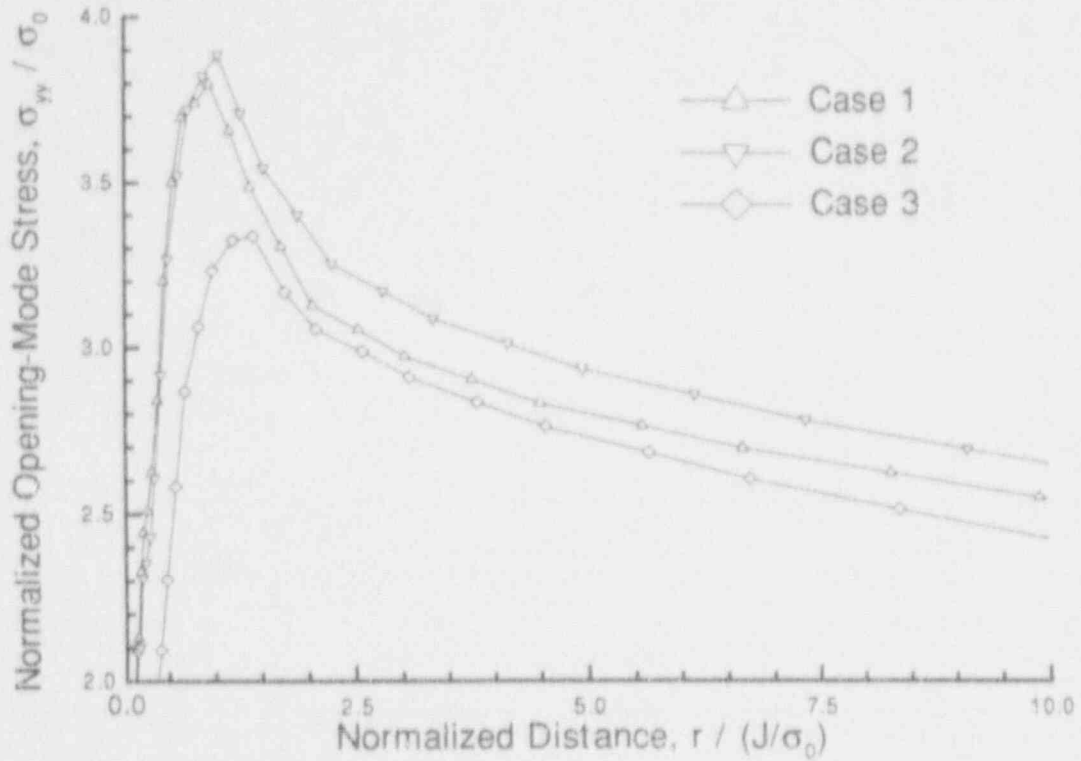


Figure 25  SSY distributions of opening-mode stress component for Cases 1, 2, and 3

ORNL-DWG 92-2898 ETD
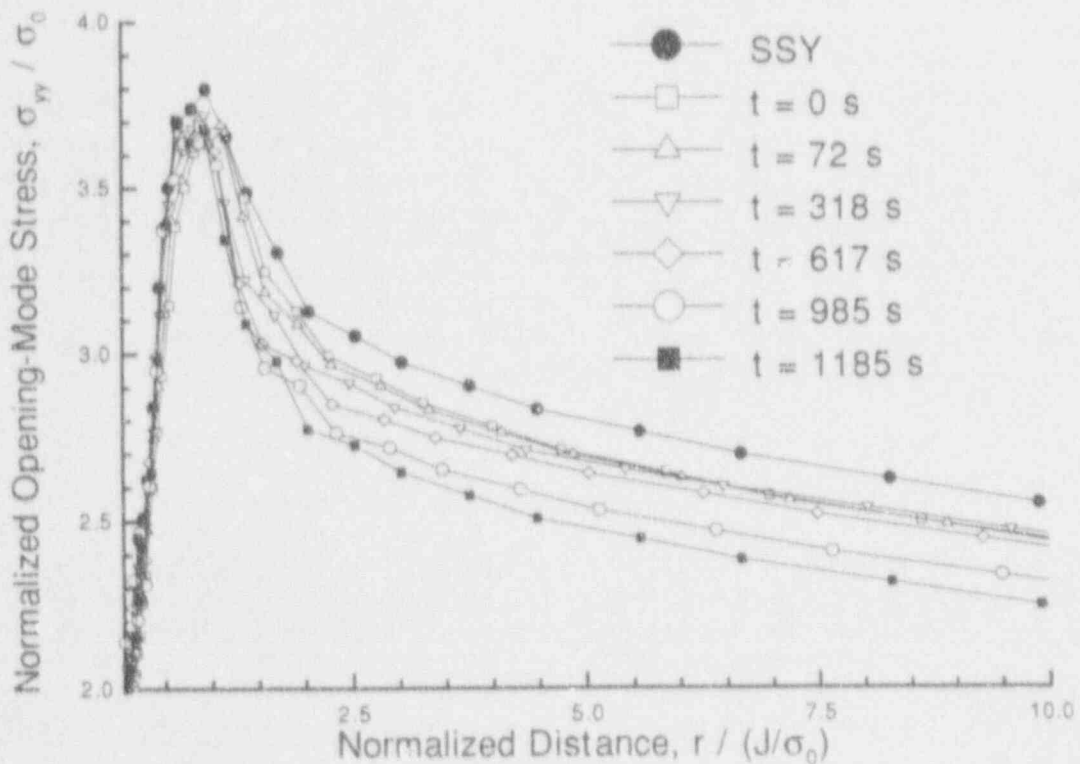


Figure 26  Distributions of opening-mode stress component for Case 1 material model: SSY and PTS loading up to maximum loading at ~1200 s into transient

30

Analogous results for the "opening-mode" stress distributions based on the Case 2 material model are indicated in Fig. 27. Analysis results in Fig. 27 also indicate that the crack-tip fields in the RPV have deviated from the SSY distribution under operating conditions. By 1200 s into the transient, the crack-tip fields are also substantially non-SSY in nature.

Analysis results for the "opening-mode" stress distributions for the Case 3 material model are indicated in Fig. 28. Analysis results in Fig. 28 also indicate that the crack-tip fields in the RPV have deviated from the SSY distribution under operating conditions. However, for up to 1200 s into the transient, the additional deviation of the crack-tip fields from the SSY distribution is not as significant as either Cases 1 or 2.

The results from Figs. 26 to 28 indicate that a calculated value of the Q-stress, based on a single location in the range of $2 \leq r/(J/\sigma_0) \leq 10$, is somewhat sensitive to the exact location. This sensitivity decreases with increase in loading time and essentially disappears by 1200 s into the transient. This sensitivity is in contrast with the results obtained in the posttest analysis of the test specimens

discussed in the Chap. 3. A factor that may contribute to the observed sensitivity during a PTS transient is that a PTS transient involves thermal-mechanical loads. Available analyses on the evaluation of the Q-stress thus far only involve mechanical loads. However, it is emphasized that the utility of the Q-stress approach is not *per se* dependent on the nature of the applied loading (e.g., mechanical vs thermal-mechanical). Instead, the utility of the Q-stress approach is only dependent on the existence of crack-tip fields of the J-Q type as discussed in Appendix B.

Beyond 1200 s into the transient, the net effects of the decreasing pressure and temperature associated with the PTS loading on the RPV result in monotonic unloading of the crack tip. The effects of unloading on the crack-tip fields are qualitatively similar for the three material models, and the results for Case 3 are used to illustrate the unloading effects. The stress distribution for Case 3 up to 1800 s into the transient is indicated in Fig. 29. With the onset of unloading that occurs subsequent to the attainment of a maximum value of the J-integral at ~1200 s, reverse yielding results in the formation of a compressive region ahead of the crack tip. At the same time, the magnitude of the stresses, such as the opening-mode stress component indicated in Fig. 29, decreases in the remaining tensile

ORNL-DWG 92-2899 ETD
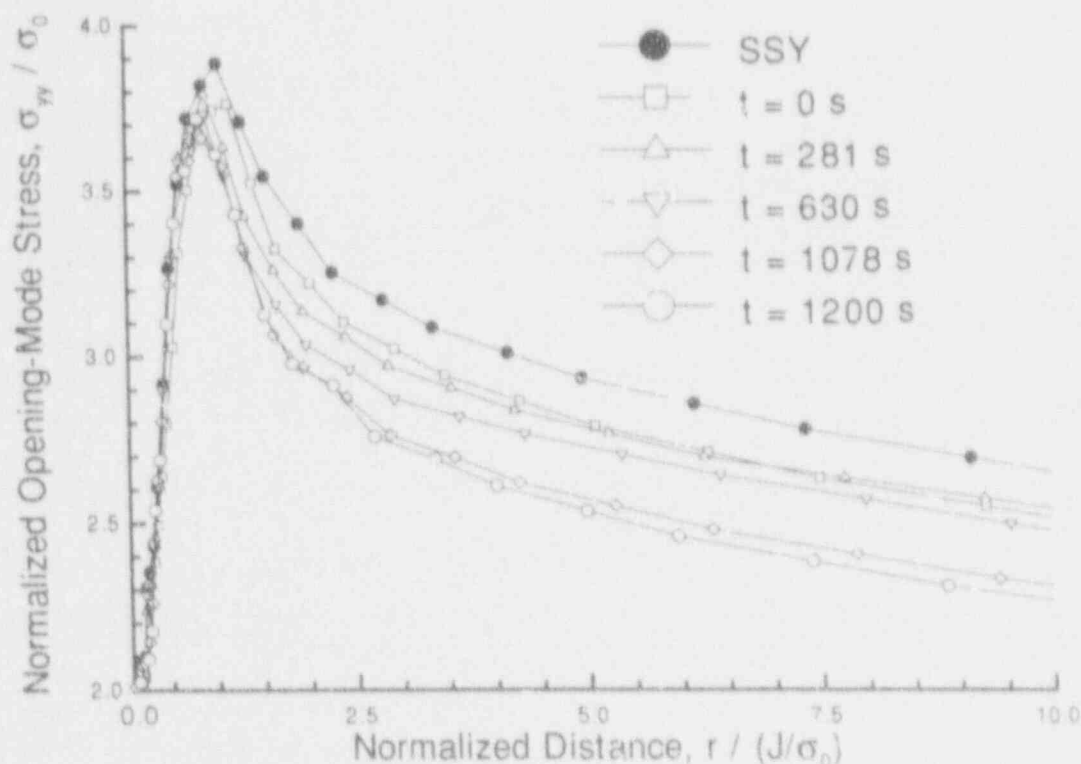


Figure 27 Distributions of opening-mode stress component for Case 2 material model: SSY and PTS loading up to maximum loading at ~1200 s into transient

ORNL-DWG 92-2900 ETD
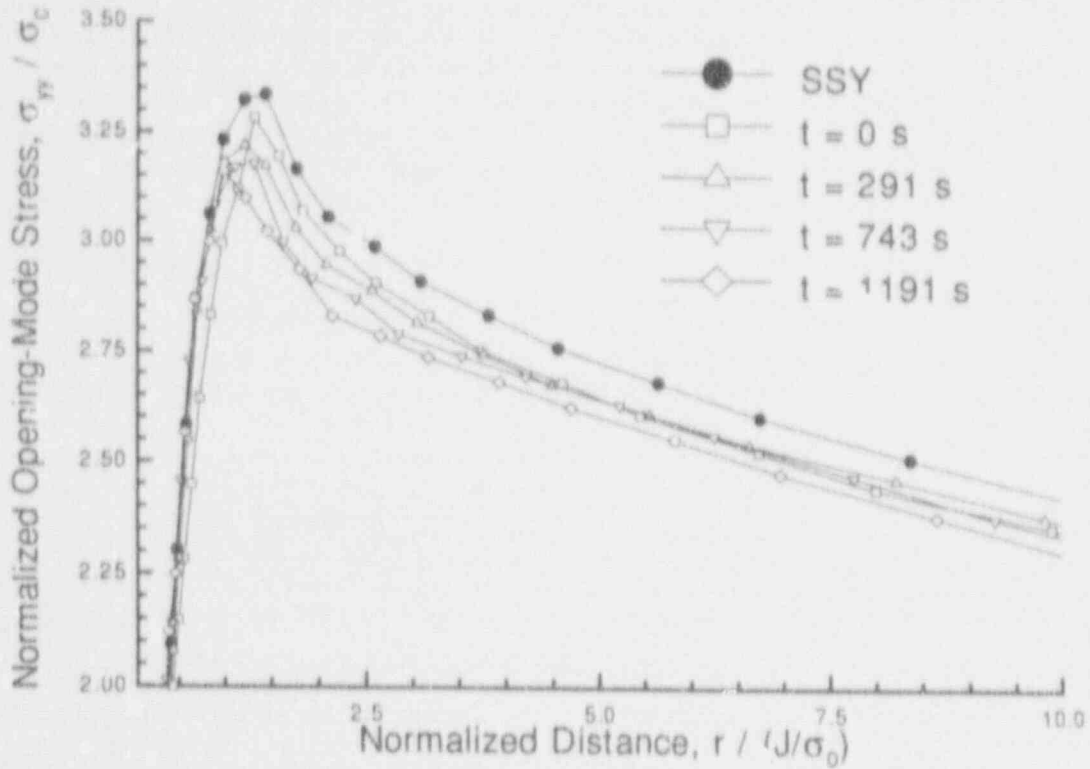


Figure 28 Distributions of opening-mode stress component for Case 3 material model: SSY and PTS loading up to maximum loading at ~1200 s into transient

ORNL-DWG 92-2901 ETD
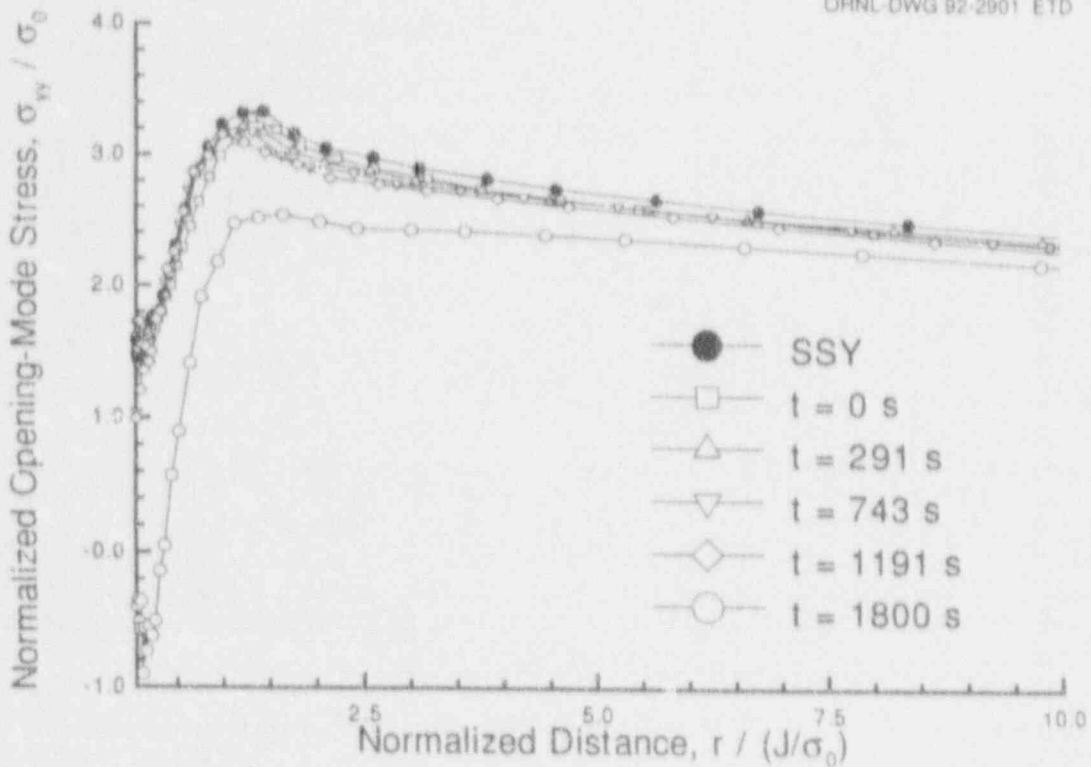


Figure 29 Distributions of opening-mode stress component for Case 3 material model: SSY and PTS loading up to 1800 s into transient

32

region ahead of the crack tip. The extent of the reverse yielding increases with transient time because the value of the J-integral monotonically decreases with time after attaining its maximum value. Interpretation of the crack-tip fields up to maximum loading and beyond, in the context of safety-margin assessment of an RPV in terms of a J-Q approach, is discussed in the following section.

## 4.6 Effects of PTS Loading on the RPV in Terms of J-Q Values

The primary objectives of these analyses are to evaluate the utility of the two-parameter J-Q approach to characterize the crack-tip fields in an RPV throughout a PTS transient and to present a methodology that incorporates small-specimen $J_c(Q,T)$ toughness locus data in the safety-margin assessment of an RPV. Analysis results appear to support the applicability of the J-Q approach and interpretation method under PTS conditions in the following sense. Results from Figs. 26 to 28 indicate that the Q-stress

parameter can be defined, for the assumed RPV, flaw geometries, and transient conditions, up to maximum loading ($t \leq 1200$ s) as characterized by the value of the J-integral during the transient. Potential problems associated with the determination of the Q-stress parameter under unloading conditions ($t > 1200$ s) will be addressed shortly. Following the discussion in Appendix B, the Q-stress parameter (as a function of transient time) is defined as the difference between the "opening-mode" stress component (as a function of time) and the associated SSY distribution in Figs. 26 to 28. The effects of the PTS loading on the RPV in terms of pairs of J-Q values are indicated in Fig. 30 for all three material models up to ~1200 s into the transient.

Neither transient time t nor crack-tip temperature T is explicitly indicated in Fig. 30. However, by referencing the values listed in Table 6 and the results in Figs. 23 and 26 to 28, it is evident that an increase in transient time and a decrease in crack-tip temperature correspond to an increase

ORNL-DWG 92M-2902 ETD
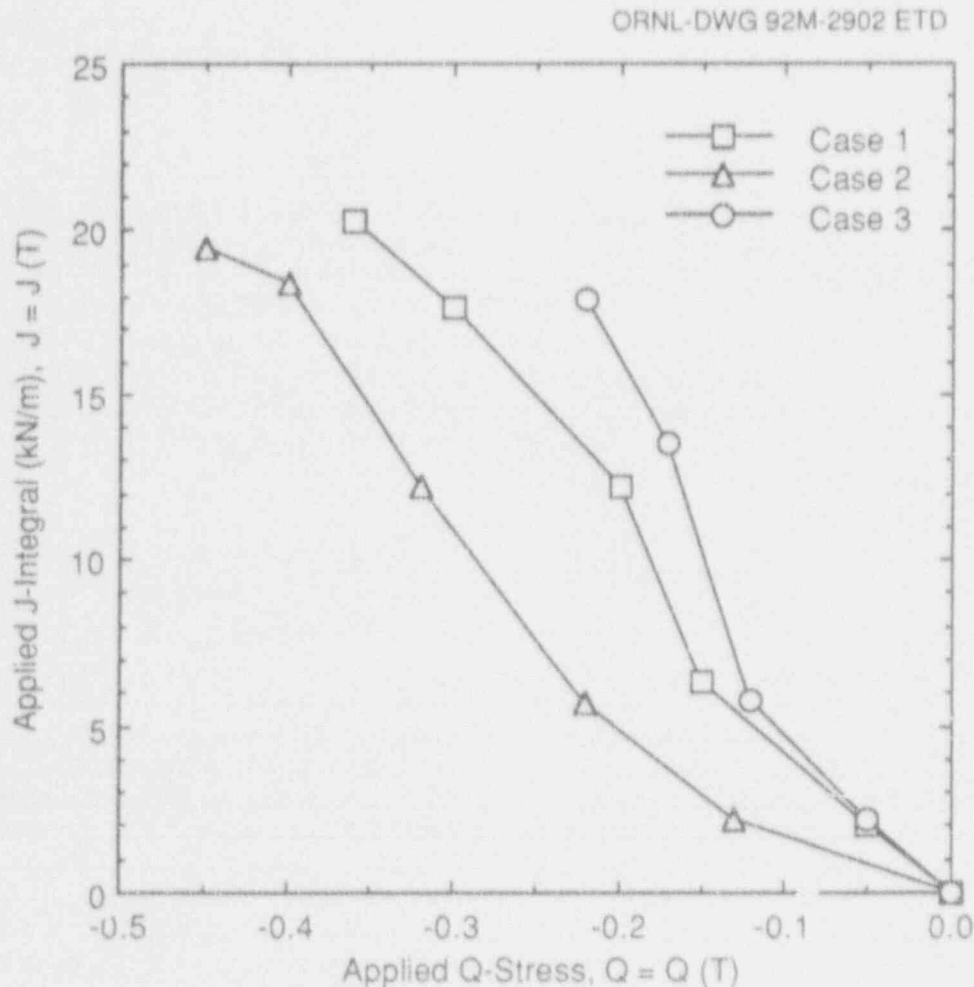


Figure 30  Applied J-Q locus for RPV for Cases 1, 2, and 3

in the value of the J-integral and a decrease in the value of the Q-stress parameter. That is both transient time and crack-tip temperature are parametric variables along the three J-Q trajectories indicated in Fig. 30. Recall that the fracture response of the RPV, as indicated in Fig. 24 solely in terms of values of the J-integral, is only slightly different for the three material models throughout the transient up to maximum loading. On the other hand, the differences in the assumed tensile response associated with the three material models result in greater differences in terms of Q-stress values. Specifically, the absolute value of the Q-stress for Case 3 conditions (simulated irradiation embrittlement) is much lower than for either Cases 1 or 2 (unirradiated). Implications of the observed differences in magnitude of the Q-stress, as a function of the material model assumed in the analyses, toward the safety-margin assessment of an RPV based on a two-parameter J-Q approach will be addressed in the next section. It is appropriate at this point to consider a number of observations that are relevant toward the evaluation and interpretation of the Q-stress parameter associated with an RPV subject to PTS loading conditions.

### 4.6.1 Definition of the Q-Stress Parameter Under Unloading Conditions

The current definition of the Q-stress parameter, as a difference-quantity between the current stress fields and the reference SSY at a single location, appears to be implicitly limited to monotonic loading conditions only. A trivial example in which use of the Q-stress parameter is not meaningful is the case of an unloaded body without residual stresses. The Q-stress parameter should reflect this absence of loading on the body. However, $Q = 0$ does not denote the absence of loading, but merely that the crack-tip fields correspond to the SSY distributions. In the case of an unloaded body without residual stresses, a strict interpretation of the current definition of the Q-stress parameter as a difference-quantity would imply the magnitude of the Q-stress parameter is identically the magnitude of the "opening-mode" stress ratio of the reference SSY distribution.

An example of this limitation in the context of RPV analysis is the evaluation of the Q-stress parameter during the unloading phase of a PTS transient. As indicated in Fig. 29, by 1800 s into the PTS transient, reverse yielding has resulted in the formation of a compressive region ahead of the crack tip and in a distribution of the "opening-mode" stress component that is substantially below the various distributions under monotonic loading conditions. Indeed, the magnitude of the "opening-mode" stress field associated with the unloading crack tip, over the range of distances currently associated with the determination of the

Q-stress parameter, would eventually be negative at a much later time in the transient. (A related example of this limitation is the evaluation of the Q-stress parameter during the reloading phase of a PTS transient that involves repressurization.) Consequently, the Q-stress parameter is currently being considered for use only up to the point of maximum loading.

### 4.6.2 Physical Significance of J-Q Annulus

Care must be taken to ensure that the physical distances associated with the evaluation of the Q-stress parameter in RPV applications are meaningful and consistent with the underlying continuum analysis assumptions. From Table 6, the value of the J-integral under operating conditions $J_{op}$ is on the order of 2 kN/m for the present analysis conditions. The magnitude of the parameter $J/\sigma_0$ at operating conditions for Cases 1 to 3 thus correspond to ~4 to 6 µm. Taking the average grain size of 20 to 30 µm for steel plate A 533 B-13A as representative of RPV-grade materials,[15] it is observed that at operating conditions the Q-stress parameter is evaluated over distances that are substantially smaller than those necessary for the calculated Q-stress to be both physically meaningful and relevant in the context of continuum mechanics.

On the other hand, the maximum value of the J-integral, which occurs at ~1200 s into the transient with a value of $J_{max} \approx 20$ kN/m, results in a magnitude of the parameter $J/\sigma_0$ on the order of 40 to 60 µm. If one further adopts the more relaxed definition of the Q-stress proposed in the previous chapter, namely over a limited range of distances ahead of the crack tip in the range of $2 \leq r/(J/\sigma_0) \leq 5$, then evaluation of the Q-stress parameter at ~1200 s is physically meaningful and relevant in the context of continuum mechanics.

## 4.7 Incorporation of Small-Specimen $J_c(Q,T)$ Toughness Locus Data in RPV Safety-Margin Assessment

A methodology to incorporate small-specimen $J_c(Q,T)$ toughness locus data in the safety-margin assessment of an RPV is presented in this section. For simplicity, it is assumed that type-I warm prestress (WPS) is operative during the unloading phase of this transient, so attention is focused on the PTS transient only up to ~1200 s.[26] It will be shown that the predicted margin of safety in RPVs under PTS conditions is then greater based on the two-parameter approach than that based on the conventional one-parameter approach. A schematic illustrating the differences between the one- and two-parameter safety-

margin assessment method is given in Fig. 31, in which the applied J-Q trajectory for Cases 1 to 3 illustrates possible RPV response as a function of (simulated) irradiation-embrittlement of the vessel.

Current RPV safety-margin assessment methods character-ize the severity of a given loading condition solely in terms of the magnitude of the J-integral or the stress-intensity factor K.[5-7,27] Prediction of crack initiation, crack arrest, and reinitiation using this single-parameter approach is based on comparison of the applied value of the J-integral (or K) with the relevant *irradiated* material toughness parameter. In an analysis, representation of loading condi-tions in terms of either J or K is equivalent in the context of characterizing the crack-tip field-intensity parameter. How-ever, the determination of fracture toughness as defined in ASTM E399 and ASTM E813 involves an additional con-sideration on the micromechanics of fracture. Cleavage

fracture is associated with $K_{Ic}$, and ductile fracture with $J_{Ic}$. In a subsequent discussion, this distinction between the use of J or K in analysis and toughness determination is ignored, and J will be used throughout the discussion. In addition, scatter in fracture toughness is also ignored for purposes of this discussion.

During a PTS transient, the crack-tip temperature, and hence fracture toughness, decreases monotonically with transient time. A curve that schematically illustrates the locus of one-parameter irradiated fracture toughness, denoted as $J_c(T)$, is shown in Fig. 31. It is emphasized that the one-parameter $J_c(T)$ toughness locus does not depend on the Q-stress parameter but that its indicated variation with Q-stress is strictly an indication of the dependence $J_c(T)$ on crack-tip temperature. The margin of safety (MS) can then be established based on comparing the value of the applied J-integral to $J_c(T)$ as indicated in Fig. 31. Thus,

ORNL-DWG 92M-2903 FED
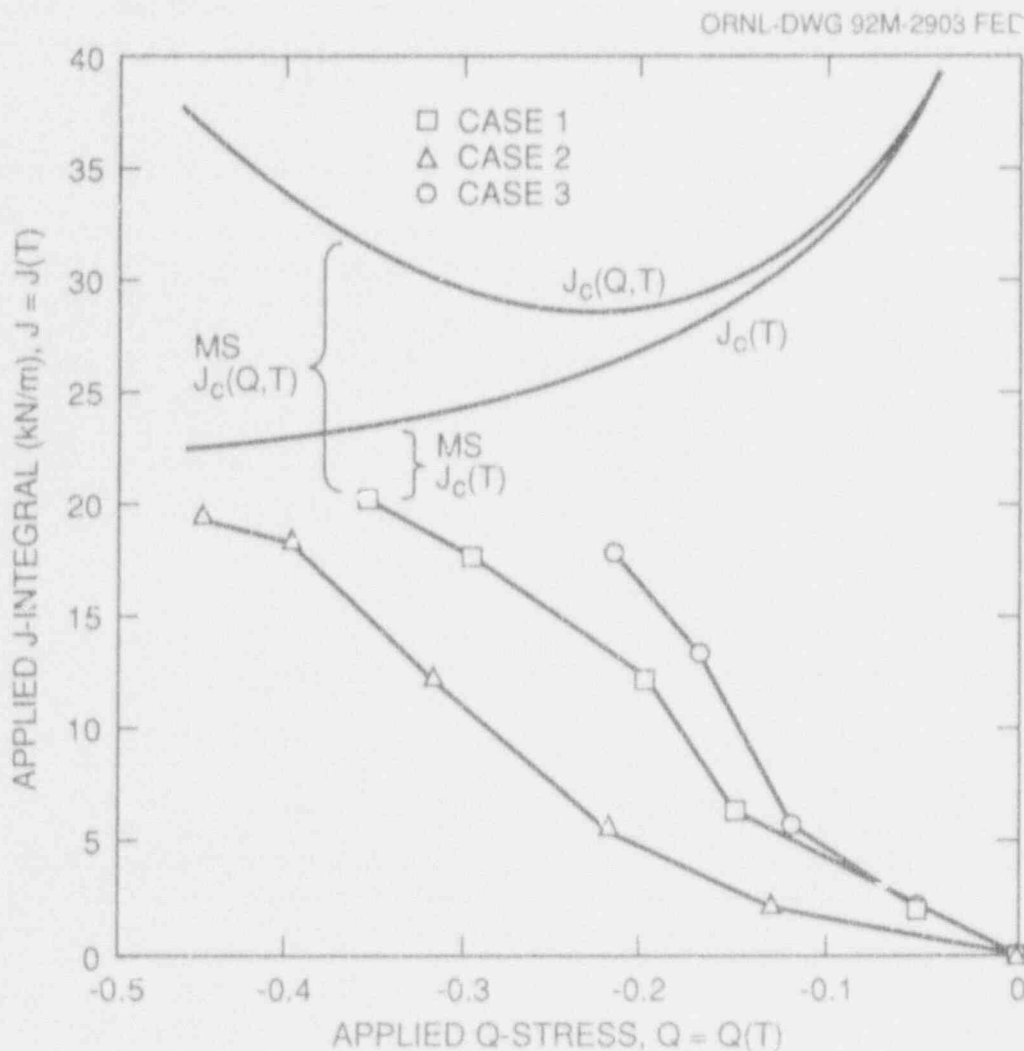


Figure 31 Schematic illustrating the margin of safety based on J-only or J-Q toughness data

the transient may be most severe, and the margin of safety at a minimum, at the transient time associated with the maximum value of the applied J-integral.

Also schematically indicated in Fig. 31 is a curve denoted as $J_c(Q,T)$ that, based on available small-specimen *unirradiated* toughness data such as those from the HSST shallow-flaw testing program, is believed to *qualitatively* illustrate the anticipated $J_c(Q,T)$ toughness locus trend for *irradiated* RPV-grade materials. Available (isothermal) unirradiated results suggest that the $J_c(Q,T)$ toughness locus depends weakly on the Q-stress for the approximate range of $Q > -0.2$.[23,*] This weak dependence is reflected in the near coincidence of the $J_c(Q,T)$ and $J_c$ locus in that Q-stress regime. Further, it is assumed that "shallow-flaw" toughness enhancement dominates over the toughness degradation associated with decreasing crack-tip temperature. For values of the Q-stress in the range $Q < -0.2$, the experimentally observed "shallow-flaw" or Q-stress effects on toughness are reflected in the elevation of the $J_c(Q,T)$ locus above the $J_c(T)$ locus.

Note that the indicated $J_c(Q,T)$ toughness locus is qualitative in nature due to the absence of irradiated experimental data. However, the point is that the margin of safety, for example, at the transient time when the applied J-integral is maximum, is predicted to be larger based on the two-parameter $J_c(Q,T)$ approach as compared with the conventional one-parameter $J_c(T)$ approach. Furthermore, depending on the actual shape of $J_c(T)$, $J_c(Q,T)$, and the applied J-Q trajectory, the time at which the PTS transient is most severe in a J-Q approach, defined as the minimum margin of safety, might differ with that determined using the one-parameter J-only approach. Most importantly, a flaw that is predicted to initiate in a PTS scenario based on the $J_c(T)$ approach might be predicted to be stable based on the more rigorous $J_c(Q,T)$ approach.

A potentially significant aspect of the results in Fig. 31 is that the calculated J-Q trajectory for Case 3 conditions (simulated irradiated-embrittlement) involves absolute values of the Q-stress parameter that are smaller than either Case 1 or 2 (unirradiated). From Fig. 31, the relative increase in the margin of safety between a one- and two-parameter approach is sensitive to the actual value of the Q-stress parameter. The results in Fig. 31 suggest that the effects of irradiation embrittlement may reduce the potential "shallow-flaw" toughness enhancement relative to unirradiated material conditions. However, it is emphasized that a more definitive interpretation awaits the generation of irradiated $J_c(T)$ and $J_c(Q,T)$ data.

Figure 31 suggests that the margin of safety in RPVs under PTS conditions is greater based on the J-Q approach than that predicted based on a J-only approach. However, it is emphasized that the requisite $J_c(Q,T)$ toughness locus is not yet available for either unirradiated or irradiated RPV-grade materials. Before the J-Q analysis technique can be applied to RPV analyses, the technique itself needs further verification. In addition, the determination and application of $J_c(Q,T)$ toughness data involve the resolution of several issues, which are detailed in the following chapter.

---

*C. F. Shih, N. P. O'Dowd, and M. T. Kirk, "A Framework for Quantifying Crack Tip Constraint," presented at the ASTM Symposium on Constraint Effects in Fracture, Indianapolis, Ind., May 8–9, 1991.

# 5 Thermal-Shock Tests

Reexamination of previous HSST thermal-shock experiment (TSE) data[10] is necessary when considering the implications of the shallow-flaw effect on RPVs during PTS transients. Thermal-shock tests were conducted to determine the fracture response of an RPV to thermal-shock loading with various flaw configurations and depths. The initial flaws ranged from 11 to 19 mm deep in a vessel wall that was 152 mm thick. These flaws are roughly the same depth as those tested in the HSST shallow-flaw program. The key result of the TSE data is that the initial initiation values were mostly within the scatter band of the ASME data base. In other words, the TSE data appear to show no substantial increase in the effective fracture toughness due to any shallow-flaw effect.

The first crack initiation in the TSE and the shallow-flaw data are presented in Fig. 32 with the ASME lower-bound curve. As can be seen, the TSE data fall near the ASME lower-bound curve, while the HSST shallow-crack data are elevated over both the deep-crack data and ASME lower-bound curve. Figure 32 also indicates that the HSST deep-crack data are significantly elevated over the ASME lower-bound curve.

A possible explanation for the lack of a shallow-crack elevation in the thermal-shock data is the presence of out-of-plane stresses, which are not present in the HSST shallow-flaw specimens. Out-of-plane (biaxial) loading has been shown to decrease the effective fracture toughness in other applications.[28] The current hypothesis being investigated is that the thermal shock tests were subjected to two offsetting influences: a "shallow-flaw effect," which increases the toughness, and a "biaxial loading effect," which decreases the toughness. The net result is that the TSE data appear consistent with the uniaxially loaded deep-crack data used to generate the ASME lower-bound curve. If the postulate is correct, the fracture toughness associated with a given shallow flaw will be a function of both constraint loss due to the shallow-flaw effect and constraint increase due to the out-of-plane stress effect. In the case of the TSE tests, which were conducted on unclad cylinders, the two effects appear to offset each other almost entirely.
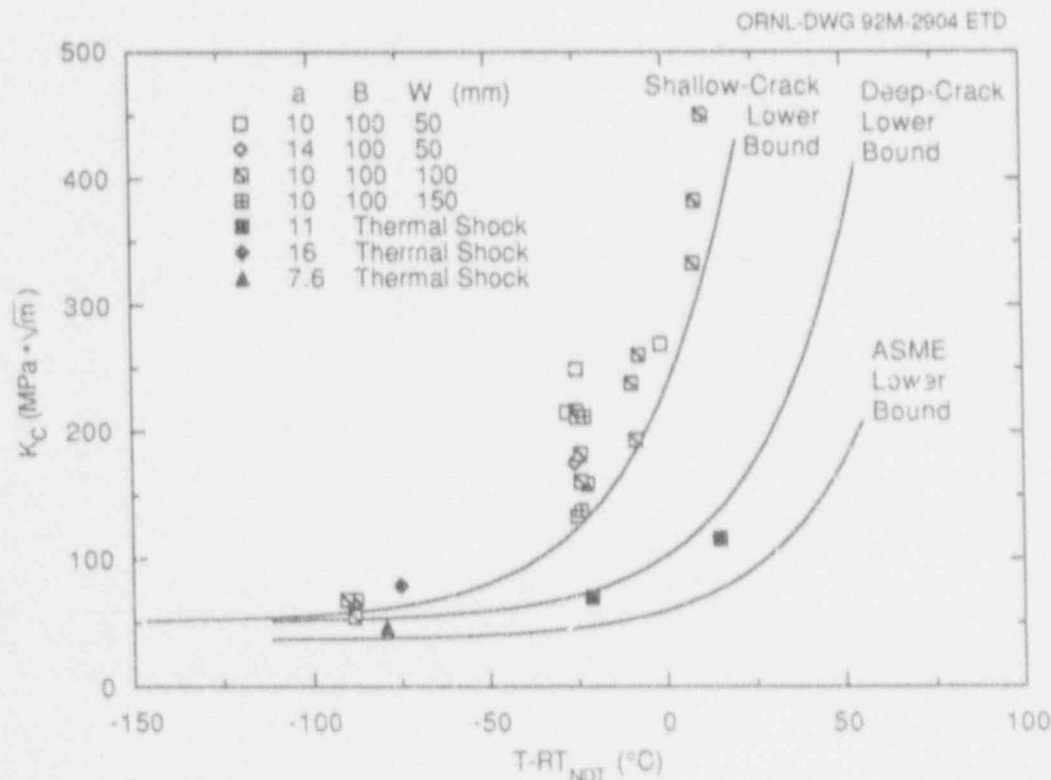


ORNL-DWG 92M-2904 ETD

Figure 32  HSST shallow-crack and thermal-shock (TSE) data with ASME lower-bound curve

# 6 Summary, Discussion, and Conclusions

This chapter summarizes the experimental and analytical studies performed to date to establish the transferability of shallow-flaw laboratory results to the PTS analysis of RPVs. Interim summaries from the previous chapters and conclusions of each are presented below. In addition, this report details work that should be performed to resolve outstanding issues and apply the shallow-flaw data using the J-Q approach to an RPV.

## 6.1 Summary of Test Results

1. Thirty-eight relatively large laboratory beam specimens were tested to compare the behavior of specimens with shallow flaws to that of specimens with deep flaws.

2. The results showed conclusively that A 533 B shallow-flaw beam specimens have a significant increase in CTOD or $J_c$ toughness (~150%) and $K_c$ toughness (~60%) in the transition region. All specimens were 100 mm deep (W). Shallow-crack beams had crack depths ranging from 9 to 14 mm (a/W ~ 0.1 to 0.14), while deep-crack beams had 50-mm-deep cracks (a/W ~ 0.5).

3. There is little or no difference in toughness on the lower shelf where linear-elastic conditions exist for specimens with either deep or shallow flaws.

4. Varying the beam thickness from 50 to 150 mm had little or no influence on the toughness in both the shallow- and deep-crack specimens in spite of the fact that the ASTM E-399 requirement for valid plane-strain results were not met.

5. In the transition region, the increase in shallow-flaw toughness compared with deep-flaw results appears to be well characterized by a temperature shift of about 35°C (63°F).

## 6.2 Summary of Posttest Specimen Analysis

1. Posttest 2-D plane-strain analyses were performed on both shallow- and deep-flaw specimens. The analytical J-integral results were consistent with experimental J-integral results based on the techniques presented in Chap. 2, confirming the validity of the J-estimation schemes used and the effect of flaw depth on fracture toughness.

2. The two-parameter J-Q analysis methodology was used as a means of quantifying the effect of flaw depth on constraint and fracture toughness. Analysis results appear to support the utility of the J-Q concept and interpretation method to characterize the crack-tip fields up to the onset of crack initiation in specimens with either deep or shallow flaws. At J-critical (onset of cleavage initiation) for the deep-flawed specimens, the Q-stress was about zero, indicating SSY conditions. At J-critical for the shallow-flawed specimens, the Q-stress was about –0.7. This negative Q-stress indicates a significant loss of constraint.

3. The observation that the two-parameter J-Q approach correlated with the loss of constraint with decreasing crack depth indicates that a J-Q analysis of actual reactor vessels may give a more accurate assessment of reactor vessel reliability than current analyses.

## 6.3 Summary of RPV Analysis

1. A 2-D plane-strain analysis of an RPV subjected to a postulated PTS transient was conducted using the two-parameter J-Q approach.

2. Three material models of A 533 B steel with yield strengths equal to an unirradiated lower-transition temperature, an unirradiated upper-shelf temperature, and irradiation-embrittled condition were studied.

3. The first two models (unirradiated lower-shelf and upper-shelf temperature models) had similar maximum values of J throughout the transient ($J_{max}$) at a time of ~1200 s (20 min) after the postulated PTS event. The third model (irradiation-embrittled) had only a slightly lower value of $J_{max}$, indicating a relative insensitivity of the value of $J_{max}$ to the particular material model.

4. Analysis results appear to support the utility of the J-Q approach and interpretation method to characterize the crack-tip fields in an RPV under PTS conditions. The value of the Q-stress ratio at $J_{max}$ is different for all three cases and appears to vary with yield strength. It ranges from –0.2 to –0.4, with the highest yield strength model (irradiation-embrittled) having the maximum constraint (Q = –0.2).

5. Using the two-parameter J-Q approach, the Q-stress ratio appears to become more negative as time increases up to the point of maximum loading. Beyond $J_{max}$, the significance of the Q-stress parameter is unclear.

6. The margin of safety appears to be greater using the J-Q approach than that predicted using only the J-approach, although additional studies must be made to validate the observation.

## 6.4 Summary of Thermal-Shock Tests

1. Previous HSST thermal-shock data failed to show any substantial toughness increase in spite of the fact that the tests were conducted on large, unclad cylindrical vessels with a shallow, initial flaw. There is no reason to believe that the thermal-shock cylinders would not have shown a toughness elevation if the cylinders had been subjected to the same loading conditions as the shallow-crack beams, namely, no biaxial stress.

2. The current hypothesis is that the thermal shock tests are being influenced by two nearly offsetting effects: a shallow-crack effect that increases the toughness and a biaxial stress effect that reduces the toughness.

## 6.5 Interpretation and Implications of RPV Analyses

The results previously summarized have several important implications for PTS analysis of an RPV. The primary implication is that J-Q analysis indicates that for the RPV transient considered, the margin of safety is potentially greater than that considered using J analyses alone. More work needs to be done before any available increase in the margin of safety can be quantified at this time. However, it is likely that other transients and RPVs that previously would have been predicted to result in crack initiation events with conventional fracture methodology would be stable based on J-Q analyses.

## 6.6 Future Work

Studies of the shallow-flaw effect on fracture toughness have been positive to date. The J-Q technique appears promising as being able to appropriately model differing constraint levels. However, numerous questions remain and need to be answered before the transferability of shallow-flaw test results to the analysis of RPVs can be made reliably. The future work is based on the use of the J-Q technique. If an alternate constraint theory is used, similar work will be necessary to validate and apply that technique for RPV analyses.

The following future work is recommended.

1. **Generate additional $J_c(Q)$ toughness data.** The $J_c(Q)$ toughness locus for A 533 B steel needs to be better defined. In particular, Q-stress data between 0 and –0.7 need to be collected. In addition, scatter in the $J_c(Q)$ data exists that needs to be quantified. Finally, the current $J_c(Q)$ data are based on 2-D finite-element analysis (FEA) and 3-D specimen data. The introduction of 3-D effects not previously considered needs to be assessed.

To produce a sufficient $J_c(Q)$ locus for application to an RPV, additional testing and analysis must take place. First, additional analyses of HSST shallow-crack beams need to be performed. In particular, beams at other temperatures and the beam with an intermediate crack depth (a = 14 mm) need to be analyzed to produce additional Q-stress data between 0 and –0.7. Temperature should be included as a variable to determine if a different $J_c(Q)$ locus needs to be determined for each temperature. Second, tests being conducted at David Taylor Research Center (DTRC) need to be included in the $J_c(Q)$ locus. These tests will be conducted with alternate geometries and with increased-yield-strength A 533 B material so comparisons can be made with the HSST shallow-crack beam data. Finally, full-thickness clad beam tests are to be conducted on actual PWR material with flaw depths similar to those tested in the HSST shallow-crack program in the near future. These tests need to be analyzed in terms of J-Q to determine the influence of different beam depths (W) on fracture toughness. These steps should begin to quantify the scatter in the $J_c(Q)$ locus and provide Q-stress data between 0 and –0.7. Eventually sufficient data will need to be generated to validate the J-Q approach as a reliable correlator of a toughness increase rather than a means of interpreting the constraint loss.

To assess the influence of 3-D effects, additional analyses need to be conducted to evaluate both the 2-D and 3-D response of a shallow-crack beam. If this analysis is inconclusive, then 3-D analyses of an RPV may need to be compared with current 2-D RPV analyses.

2. **Perform sensitivity analyses of applied J-Q data.** Analyses presented in this report are based on one RPV geometry using one particular transient. Sufficient analyses need to be performed on multiple RPV geometries and PTS transients to determine the sensitivity of the applied J-Q curve to important PTS parameters (such as pressure level and thermal shock severity).

3. **Determine applicability of J-Q approach to irradiated data.** Available $J_c(Q,T)$ toughness locus data, including the HSST shallow-flaw data, are limited to unirradiated material properties and simple laboratory-specimen geometries. TSEs that involved cylindrical vessels with shallow inner-surface axial flaws were performed by the HSST program staff. The vessel material was A 508 chemistry with elevated tensile properties to simulate irradiated material properties.[29-32] Published analyses on the thermal-shock test results are available only in the context of linear-elastic one-parameter approaches in terms of K and J. Detailed elastic-plastic J-Q analysis of the thermal-shock tests is in progress. A quantitatively correct $J_c(Q,T)$ toughness locus needs to reflect the effects of irradiation

# Summary

embrittlement on fracture toughness. Currently, the effects of crack-tip temperature and irradiation embrittlement on fracture toughness are assumed to be indexed by, or dependent on, $T - RT_{NDT}$.[3] This temperature-shift methodology provides the basis for a convenient engineering approach to incorporate temperature and irradiation effects on toughness. Results from the HSST shallow-flaw testing program appear to indicate that the "shallow-flaw" or Q-stress effects on unirradiated toughness might be amendable to some form of $RT_{NDT}$ shift. It remains to be determined if an appropriate temperature-shift methodology could be established for irradiated $J_c(Q,T)$ toughness data.

**4. Experimentally verify the J-Q fracture methodology.** The J-Q analyses presented in this report are a promising method of taking into account different constraint levels. However, before this technique can be fully implemented into RPV fracture methodology, additional experimental verification of the J-Q method should take place. Primarily, an investigation should be conducted on either direct or indirect measurement of the Q-stress. In addition, the J-Q technique should be applied to other fracture experiments with differing levels of constraint to determine the limitations of the technique.

**5. Determine influence of biaxial loading.** Currently the influence of out-of-plane (biaxial) loading is inferred from thermal-shock and HSST shallow-crack data. The direct influence of biaxial loading needs to be shown analytically and experimentally. The current hypothesis is that the TSE data are being influenced by both the shallow-crack effect and a biaxial stress effect. To substantiate this hypothesis,

3-D analyses of a shallow flaw in a TSE cylinder and a free-standing thin ring will be performed under thermal-shock loading. The cylinder will represent fully biaxial loading, and the ring will have out-of-plane (axial) stresses that are much less than in the cylinder. Thus, the influence of the axial stress can be investigated. If a significant difference is found between the in-plane stresses of the cylinder and the ring, the current hypothesis will be substantiated. If no differences are found, then additional analyses and alternate criteria such as a strain-based criteria may be required to explain the HSST shallow-crack toughness elevation and the lack of toughness increase in the TSE data.

**6. Resolve different $J_c(Q)$ data.** Recent reanalysis of the ORNL wide-plate series using a 2-D, J-Q analysis and the HSST shallow-crack beam J-Q analysis produced different sets of $J_c(Q)$ data. According to the underlying theory of the J-Q technique, these data sets should have been similar. This discrepancy will have to be explained before the J-Q techniques can be used in RPV fracture methodology.

In summary, the enhancement in fracture toughness of A 533 B steel specimens with shallow flaws has been verified both experimentally and analytically. However, additional studies, some of which are in progress, are necessary to provide a sound engineering basis for transferring this information to the structural margin assessment of RPVs with shallow flaws. Accordingly, if it can be shown that the shallow-flaw data can be used reliably in PTS analyses, the actual reliability of reactor vessels may be greater than currently considered.

# References

1. T. J. Theiss, Martin Marietta Energy Systems, Inc., Oak Ridge Natl. Lab., "Recommendations for the Shallow-Crack Fracture Toughness Testing Task Within the HSST Program," USNRC Report NUREG/CR-5554 (ORNL/TM-11509), August 1990.[*]

2. T. J. Theiss, G. C. Robinson, and S. T. Rolfe, "Preliminary Test Results from the Heavy-Section Steel Technology Shallow-Crack Toughness Program," Proceedings of the ASME Pressure Vessel & Piping Conference, Pressure Vessel Integrity, PVP Vol. 213/MPC-Vol. 32, pp. 125–129, ASME 1991.[†]

3. W. E. Pennell, "Heavy-Section Steel Technology Program: Recent Developments in Crack Initiation and Arrest Research," pp. 2-1 to 2-2 in Transactions of the Nineteenth Water Reactor Safety Information Meeting, NUREG/CP-0118, October 1991.[*]

4. S. T. Rolfe, University of Kansas for Martin Marietta Energy Systems Inc., Oak Ridge Natl. Lab., "The Behavior of Shallow Flaws in Reactor Pressure Vessels: Status Report," USNRC Report NUREG/CR-5767 (ORNL/Sub/90-SH640/1), November 1991.[*]

5. R. D. Cheverton and D. G. Ball, Martin Marietta Energy Systems, Inc., Oak Ridge Natl. Lab., "Pressurized-Thermal-Shock Evaluation of the H. B. Robinson Nuclear Power Plant," pp. 253–306, USNRC Report NUREG/CR-4183 (ORNL/TM-9567/V1), September 1985.[*]

6. R. D. Cheverton and D. G. Ball, Martin Marietta Energy Systems, Inc., Oak Ridge Natl. Lab., "Pressurized-Thermal-Shock Evaluation of the Calvert Cliffs Nuclear Power Plant," pp. 201–244, USNRC Report NUREG/CR-4022 (ORNL/TM-9408), September 1985.[*]

7. R. D. Cheverton and D. G. Ball, Martin Marietta Energy Systems, Inc., Oak Ridge Natl. Lab., "Preliminary Development of an Integrated Approach to the Evaluation of Pressurized Thermal Shock as Applied to the Oconee 1 Nuclear Power Plant," pp. 5.1–5.51, USNRC Report NUREG/CR-3770 (ORNL/TM-9176), May 1986.[*]

8. U. S. Nuclear Regulatory Commission Regulatory Guide 1.154, "Format and Content of Plant-Specific Pressurized Thermal Shock Safety Analysis Reports for Pressurized Water Reactors," January 1987.[‡]

9. W. Marshall, "An Assessment of the Integrity of PWR Pressure Vessels," October 1976.[§]

10. R. D. Cheverton, S. K. Iskander, and D. G. Ball, "Review of Pressurized-Water-Reactor-Related Thermal Shock Studies," pp. 752–766 in Fracture Mechanics: Nineteenth Symposium, ASTM STP 969, American Society for Testing and Materials, Philadelphia, 1988.[†]

11. T. J. Theiss, Martin Marietta Energy Systems, Inc., Oak Ridge Natl. Lab., "Cleavage Crack Initiation," pp. 43–50 in HSST Program Semiann. Prog. Rep. April–September 1991, USNRC Report NUREG/CR-4219, Vol. 8, No. 2 (ORNL/TM-9593/V8&N2), April 1992.[*]

12. W. A. Sorem, R. H. Dodds, Jr., and S. T. Rolfe, "An Analytical Comparison of Short Crack and Deep Crack CTOD Fracture Specimens of an A36 Steel," WRC Bulletin 351, Welding Research Council, New York, February 1990.[†]

13. J. A. Smith, and S. T. Rolfe, "The Effect of Crack Depth to Width Ratio on the Elastic-Plastic Fracture Toughness of a High-Strength Low-Strain Hardening Steel," WRC Bulletin 358, Welding Research Council, New York, November 1990.[†]

14. D. J. Naus et al., Martin Marietta Energy Systems, Inc., Oak Ridge Natl. Lab., "SEN Wide-Plate Crack-Arrest Tests Using A 533 Grade B Class 1 Material: WP-CE Series," USNRC Report NUREG/CR-5408 (ORNL/TM-11269), November 1989.[*]

15. D. J. Naus et al., Martin Marietta Energy Systems, Inc., Oak Ridge Natl. Lab., "Crack Arrest Behavior in SEN Wide Plates of Quenched and Tempered A 533 Grade B Steel Tested Under Nonisothermal Conditions," USNRC Report NUREG/CR-4930 (ORNL-6388), August 1987.[*]

16. R. K. Nanstad and S. K. Iskander, Martin Marietta Energy Systems, Inc., Oak Ridge Natl. Lab., "Material Characterization and Properties," pp. 23–25 in HSST Program Semiann. Prog. Rep. April–September 1991,

# References

USNRC Report NUREG/CR-4219, Vol. 8, No. 2 (ORNL/TM-9593/V8&N2), April 1992.[*]

17. K. J. Bathé, Massachusetts Institute of Technology, "ADINA-87, A Finite Element Program for Automatic Dynamic Incremental Nonlinear Analysis," MIT Report 82448-1, 1975.[*]

18. J. M. Barsom and S. T. Rolfe, *Fracture and Fatigue Control in Structures*, Prentice-Hall, Englewood Cliffs, N.J., 1987.

19. N. P. O'Dowd and C. F. Shih, "Family of Crack-Tip Fields Characterized by a Triaxiality Parameter: Part I—Structure of Fields," *J. Mech. Phys. Solids* 39, 989–1015 (1991).[*]

20. A. M. Al-Ani and J. W. Hancock, "J-Dominance of Short Cracks in Tension and Bending," *J. Mech. Phys. Solids* 39, 23–43 (1991).[*]

21. ABAQUS *Theory Manual*, Version 4-8, Hibbitt, Karlson and Sorensen, Inc., Providence, R.I., 1989.

22. H. Tada, P. C. Paris, and G. R. Irwin, *The Stress Analysis of Cracks Handbook*, Del Research Corporation, Hellertown, Pa., 1973.

23. J. D. G. Sumpter and J. W. Hancock, "Shallow Crack Toughness of HY80 Welds: An Analysis Based on T Stresses," *Int. J. Pres. Ves. & Piping* 45, 207–221 (1991).[†]

24. S. Glasstone and A. Sesonske, p. 458, in *Nuclear Reactor Engineering*, Van Nostrand Reinhold Co., New York, 1981.

25. J. J. McGowan, "Tensile Properties of Irradiated Nuclear Grade Pressure Vessel Plate and Welds for the Fourth HSST Irradiation Series," USNRC Report NUREG/CR-3978 (ORNL/TM-9516), January 1985.[*]

26. D. K. M. Shum, Martin Marietta Energy Systems, Inc., Oak Ridge Natl. Lab., "Implications of Warm Pre-stress on Safety-Margin Assessment of Reactor Pressure Vessels," ORNL/NRC/LTR-92/9, March 1992.[§]

27. D. K. M. Shum et al., Martin Marietta Energy Systems, Inc., Oak Ridge Natl. Lab., "Potential Change in Flaw Geometry of an Initially Shallow, Axially Oriented, Inner-Surface Finite-Length Flaw During a Pressurized-Thermal-Shock Transient," ORNL/NRC/LTR-92-1, January 1992.[§]

28. D. Aurich et al., "The Influence of the Stress State on K_Ic," *Transactions of the 4th International Conference on Structural Mechanics in Reactor Technology*, Vol. G, August 1977.[†]

29. R. D. Cheverton, Union Carbide Corp. Nucl. Div., Oak Ridge Natl. Lab., "Pressure Vessel Fracture Studies Pertaining to a PWR LOCA-ECC Thermal Shock: Experiments TSE-1 and TSE-2," USNRC Report ORNL/NUREG/TM-31, September 1976.[*]

30. R. D. Cheverton and S. E. Bolt, Union Carbide Corp. Nucl. Div., Oak Ridge Natl. Lab., "Pressure Vessel Fracture Studies Pertaining to a PWR-LOCA-ECC Thermal Shock: Experiments TSE-3 and TSE-4 and Update of TSE-1 and TSE-2 Analysis," USNRC Report ORNL/NUREG-22, December 1977.[*]

31. R. D. Cheverton, S. K. Iskander and S. E. Bolt, Union Carbide Corp. Nucl. Div., Oak Ridge Natl. Lab., "Applicability of LEFM to the Analysis of PWR Vessels under LOCA-ECC Thermal Shock Conditions," USNRC Report NUREG/CR-0107 (ORNL/NUREG-40), October 1978.[*]

32. R. D. Cheverton et al., Martin Marietta Energy Systems, Inc., Oak Ridge Natl. Lab., "Pressure Vessel Fracture Studies Pertaining to the PWR Thermal-Shock Issue: Experiment TSE-7," USNRC Report NUREG/CR-4304 (ORNL-6177), August 1985.[*]

33. U.S. Nuclear Regulatory Commission, *Regulatory Guide 1.99, Revision 2*, "Radiation Embrittlement of Reactor Vessel Materials."[‡]

---

[*]Available for purchase from National Technical Information Service, Springfield, VA 22161.
[†]Available from public technical libraries.
[‡]Copies are available from U.S. Government Printing Office, Washington, D.C. 20402. ATTN: Regulatory Guide Account.
[§]Available in NRC Public Document Room for inspection and copying for a fee.

# Appendix A

## Experimental Determination of Toughness for Shallow Flaws

This appendix describes the experimental techniques used to determine the shallow-crack toughness in terms of the CTOD, the J-integral, and the stress-intensity factor $K_c$. The deep-crack toughness has been calculated according to ASTM E1290, Crack-Tip Opening Displacement (CTOD) Fracture Toughness Measurement; ASTM E813, $J_{Ic}$, A Measure of Fracture Toughness; and ASTM E399, Plane-Strain Fracture Toughness of Metallic Materials, respectively. ASTM E813 was used for $J_c$ calculations even though the failures were predominantly cleavage events. The shallow-crack toughness formulations are as similar as possible to the deep-crack ASTM standard toughness formulations.

### A.1 CTOD $\delta_c$ Calculation

The plastic component of CTOD is determined experimentally from the plastic component of CMOD and the rotation factor. The plastic displacement of the crack flanks is assumed to vary linearly with distance from the plastic center of rotation. In this way, the plastic CMOD can be related to the plastic CTOD. The plastic center of rotation is located ahead of the crack tip a distance equal to the rotation factor (RF) multiplied by the remaining ligament $(W-a)$[1]. Numerous experimental and analytical techniques have been used to determine the rotation factor,[1-8] although no single technique seems to be universally accepted, and the various experimental and analytical determinations sometimes appear contradictory,[3] especially for shallow-crack specimens. The rotation factor in ASTM E1290 is given to be 0.4 but is a function of specimen geometry and material.

In the HSST shallow-crack study two experimental methods were used to determine the rotation factor. The first method was the use of dual clip gages located at different distances from the crack mouth. Clip gages were mounted directly on the crack mouth and elevated 8.89 mm (0.35 in.) above the crack mouth. The second technique was to locate the neutral axis of the beam ahead of the crack tip using strain gages, assuming that the plastic center of rotation was located at the neutral axis of the beam. Because the rotation factor relates the plastic component of CMOD to the plastic component of CTOD, only plastic strains were used to determine the rotation factor. The dual clip gage technique produced values of the rotation factor that varied significantly from 0.4 and were not constant as a function of load. However, the rotation factors determined using the strain gage technique were close to 0.4 and were relatively insensitive to load once plastic

strains became nontrivial. The rotation factors from strain gages were averaged for the deep- and shallow-crack geometries and were used in the CTOD calculations. The average rotation factor varied from 0.44 for the deep-crack specimens to 0.49 for the shallow-crack specimens. The rotation factor used for the CTOD toughness calculations is the average of the values from the strain-gage technique for the two crack depths.

A parametric evaluation was performed to assess the sensitivity of the calculated CTOD toughness on the rotation factor. This evaluation indicated that the plastic component of CTOD is not overly sensitive to the value of the rotation factor. Shallow-crack beams are less sensitive to the rotation factor than deep-crack beams. A 25% increase in rotation factor increases the plastic CTOD by ~5% and 17% for the shallow- and deep-crack geometries, respectively. The rotation factor is insensitive to beam thickness and absolute beam dimensions, varying only with a/W ratios for a given material.

### A.2 J-Integral $J_c$ Calculations

Fracture toughness was determined for each beam in terms of the J-integral using two slightly different techniques. Little or no crack growth took place in these tests, so ASTM E813 is not strictly applicable. In the first technique, $J_c$ was computed using a total energy approach utilizing the total area under the load - LLD curve and a single $\eta$ factor that was estimated from finite-element analyses of the HSST deep- and shallow-crack beams. The second technique calculates J by dividing the elastic and plastic components of J and using only the plastic component of area under the load vs LLD curve and a plastic $\eta$ factor.[3] The following equations were used to determine the shallow-crack J-integral toughness:

$$J_c = J_{el} + J_{pl} , \tag{A.1}$$

where

$$J_{el} = K_c^2 (1 - \nu^2)/E \tag{A.2}$$

and

$$J_{pl} = \eta_{pl} U_{pl}/[B(W-a)] , \tag{A.3}$$

where $U_{pl}$ is plastic energy or area under load vs LLD curve.

## Experimental

The two J-integral techniques gave reasonably close values of J-integral toughness within ~20% of each other. The second technique yielded more consistent values of $J_c$ as a function of thickness. The J-integral toughness values using the divided energy technique are given in Table 3 of Chap. 2.

## A.3 Stress-Intensity Factor $K_c$ Calculation

Because $J_c$ and $\delta_c$ are related according to $J_c = m \cdot \sigma_f \cdot \delta_c$, comparison of $J_c$ and $\delta_c$ allows m, the constraint parameter, to be determined as a function of crack depth.[9] Plots of J vs CTOD show a linear relationship between the two toughness expressions. The constraint parameter m for each test was determined using the critical toughness ($J_c$ and $\delta_c$) and the estimated flow stress $\sigma_f$. Use of the critical toughness is in keeping with Sumpter's contention that $\eta_{pl}$ is valid only for a perfectly plastic material after limit load.[3] The constraint values were calculated for each test. The average constraint parameter was 1.5 for deep-crack specimens and 1.1 for shallow-crack specimens.

Although the J-integral and CTOD toughness expressions are generally consistent with each other, the CTOD toughness was considered more reliable than the J-integral because the experimental load vs CMOD records were more consistent and repeatable than the load vs LLD records. For these reasons, $K_c$ was calculated from CTOD using the following relation:[9]

$$K_c = \{m \cdot \sigma_f \cdot E' \cdot \delta_c\}^{1/2} , \qquad (A.4)$$

where $m = 1.5$ and $E' = E/(1 - v^2)$ for deep-crack specimens, and $m = 1.1$ and $E' = E$ for shallow-crack specimens.

The plane strain value of $E'$ was used for the deep-crack specimens in spite of not meeting the validity requirements of ASTM E399 because the experimental data in this program indicates little or no influence of beam thickness on the data.

For comparison, $K_c$ was calculated directly from the J-integral values discussed above in addition to using CTOD and Eq. (A.4). The two methods of determining $K_c$ are very consistent with the average difference between the two methods within 6%.

## References

1. W. A. Sorem, R. H. Dodds, Jr., and S. T. Rolfe, "An Analytical Comparison of Short Crack and Deep Crack CTOD Fracture Specimens of an A36 Steel," *WRC Bulletin 351*, Welding Research Council, New York, February 1990.[*]

2. J. A. Smith and S. T. Rolfe, "The Effect of Crack Depth to Width Ratio on the Elastic-Plastic Fracture Toughness of a High-Strength Low-Strain Hardening Steel," *WRC Bulletin 358*, Welding Research Council, New York, November 1990.[*]

3. J. D. G. Sumpter, "$J_c$ Determination for Shallow Notch Welded Bend Specimens," *Fatigue Fract. Eng. Mat. & Struct.* 10(6), 479–493 (1987).[*]

4. B. Cottrell et al., "On the Effect of Plastic Constraint on the Ductile Tearing in a Structural Steel," *Eng. Fract. Mech.* 21(2), 239–244 (1985).[*]

5. Q.-F. Li, "A Study About $J_i$ and $d_i$ in Three-Point Bend Specimens with Deep and Shallow Notches," *Eng. Fract. Mech.* 22(1), 9–15 (1985).[*]

6. D.-Z. Zhang and H. Wang, "On the Effect of the Ratio a/W on the Value of $d_i$ and $J_i$ in a Structural Steel," *Eng. Fract. Mech.* 26(2), 247–250 (1987).[*]

7. G. Matsoukas, B. Cottrell, and Y.-W. Mai, "On the Plastic Rotation Constant Used in Standard COD Tests," *Int. J. Fract.* 26(2), R49–R53 (1984).[*]

8. T. L. Anderson, H. I. McHenry, and M. G. Dawes, "Elastic-Plastic Fracture Toughness Tests with Single-Edge Notched Bend Specimens," pp. 210–229 in *Elastic-Plastic Fracture Test Methods: The User's Experience, ASTM STP 856*, E. T. Wessel and F. J. Loss, Eds., American Society for Testing and Materials, 1985.

9. J. M. Barsom and S. T. Rolfe, *Fracture and Fatigue Control in Structures*, Prentice-Hall, Englewood Cliffs, N.J., 1987.

---

[*]Available in public technical libraries.

# Appendix B

## Definition of T-Stress and Q-Stress Parameters

### B.1 Definition of T-Stress Parameter

Within the context of LEFM, it is known that the asymptotic 2-D near-crack-tip fields, as a function of position relative to the crack tip, can be expressed in the form of an infinite series. Let $(r,\theta)$ denote the position of a material point relative to the crack tip in polar coordinates. The infinite series denoting the Mode I stress components then take the form

$$\sigma_{ij} = \frac{K_I}{\sqrt{2\pi r}} \tilde{\sigma}_{ij}(\theta) + T\delta_{1j}\delta_{i1} + \dots , \qquad (B.1)$$

where $\tilde{\sigma}_{ij}(\theta)$ are universal functions that are dependent on the angular coordinate $\theta$ only.

These infinite series are commonly referred to as the Irwin-Williams series.[1,2] The first terms in these series become unbounded as the crack tip is approached. The stress-intensity factor K is the amplitude of the first terms in these series, and its value is undetermined from the asymptotic expansion. Interpretation of K as a crack-tip-field intensity parameter forms the basis of conventional one-parameter LEFM theory.

The T-stress parameter is the next higher-order term in the series expansion for the "opening-mode" stress component. The T-stress parameter describes a stress field that is independent of position relative to the crack front and represents a uniform stress field parallel to the plane of the idealized 2-D crack. Within the context of 3-D LEFM, the Irwin-Williams asymptotic expansion concept can be generalized, resulting in three T-stresslike parameters.[3,4]

### B.2 Definition of Q-Stress Parameter

Within the context of elastic-plastic fracture mechanics (EPFM), the counterpart to the Irwin-Williams series in 2-D is the HRR solution for a deformation-theory material, with a uniaxial Ramberg-Osgood stress-strain relation.[5,6] The infinite series denoting the Mode I stress components have the form

$$\sigma_{ij} = \sigma_0 \left( \frac{J}{\alpha\sigma_0\varepsilon_0 I_n r} \right)^{\frac{1}{n+1}} \tilde{\sigma}_{ij}(\theta) + \dots , \qquad (B.2)$$

where $\tilde{\sigma}_{ij}(\theta)$ are again universal functions that are dependent on the angular coordinate $\theta$ only. In the HRR solution the first terms are also singular with an amplitude undetermined from the asymptotic analysis. In this case the undetermined amplitude corresponds to the value of the J-integral. Because the J-integral is path-independent for all deformation-theory material, its value can be evaluated from locations remote from the crack front. The path-independence of the J-integral and its identification with the amplitude or crack-tip-field intensity of the HRR field together form the basis of conventional one-parameter EPFM theory.

In a manner somewhat analogous to T-stress, the Q-stress parameter plays the role of a higher-order term in the HRR series expansion in the sense that the Mode I stress components in these series are assumed to take the form

$$\sigma_{ij} = \sigma_0 \left( \frac{J}{\alpha\sigma_0\varepsilon_0 I_n r} \right)^{\frac{1}{n+1}} \tilde{\sigma}_{ij}(\theta) + Q\sigma_0\delta_{ij} + \dots . \qquad (B.3)$$

Unlike the T-stress parameter, however, the Q-stress parameter is not an analytic consequence of the asymptotic expansion. Instead, use of the Q-stress parameter in the context of Eq. (B.3) follows from the following numerical observation. Detailed finite-element analyses performed for power-law hardening materials indicate that the near-crack-up fields appear to be consistent with the assumed expansion indicated in Eq. (B.3).[7] This assumed form generally applies only to the forward sectors that are symmetric about the crack plane ahead of the crack tip, extending ~90° to either side of the crack plane. Consequently, the utility of a Q-stress description of the near-crack-tip fields requires that the physical micromechanisms of fracture be confined within the forward sectors. The Q-stress parameter is readily understood as a state of 2-D hydrostatic tension superimposed on the HRR solution. The methodology for extending the Q-stress concept into 3-D fracture analysis is still an open issue.

Because of the numerical nature of its definition, determination of the Q-stress parameter is not without ambiguity. In its original development, the Q-stress parameter was defined as the difference between the full-field stress distributions of a given application, obtained using finite-strain theory, and the reference, small-strain HRR stress

## Definition

distributions along the crack plane. (The full-field distributions are the stress and strain distributions ... in a structure obtained by explicitly considering the influence of the finite geometry of the structure and the flaw.) It was observed that the Q-stress parameter thus determined was nearly constant over a range of distances extending $\sim 1 \leq J/\sigma_0 \leq 5$ ahead of the original crack tip. Definition of the Q-stress parameter was then made more precise by identifying Q-stress as the difference between the full-field stress distributions and reference distributions at a distance of $2J/\sigma_0$ ahead of the crack front. A limitation with this approach is that the HRR solution is available only for the case of an idealized pure-power-law material model.

A more recent approach is to define the SSY distributions (discussed in Appendix C) as the reference distributions. The Q-stress parameter is then defined as the difference between the full-field distributions and the associated SSY problem at a distance of $2J/\sigma_0$ ahead of the crack front using finite-strain theory. This approach has the advantage that it admits a more general representation of a material's stress-strain behavior. Magnitudes of the Q-stress parameter at the onset of crack initiation for the deep- and shallow-flaw geometry in Chap. 3, and for the various RPV models in Chap. 4, are determined based on this more recent approach.

## References

1. M. L. Williams, "On the Stress Distribution at the Base of a Stationary Crack," *J. Appl. Mech.* 24, 109–114 (1957).*

2. G. R. Irwin, "Fracture Mechanics," in *Structural Mechanics*, Pergamon Press, New York, 1960.

3. J. R. Rice, "Limitations to the Small Scale Yielding Approximation for Crack Tip Plasticity," *J. Mech. Phys. Solids* 22, 17–26 (1974).*

4. D. M. Parks, "Three-Dimensional Aspects of HRR-Dominance, Defect Assessment in Components—Fundamentals and Applications," pp. 205–231 in *Proceedings of the European Symposium on Elastic-Plastic Fracture Mechanics*, ESIS/EGF Publication 9, 1991.*

5. J. W. Hutchinson, "Singular Behavior at the End of a Tensile Crack in a Hardening Material," *J. Mech. Phys. Solids* 16, 13–31 (1968).*

6. J. R. Rice and G. F. Rosengren, "Plane Strain Deformation Near a Crack Tip in a Power-Law Hardening Material," *J. Mech. Phys. Solids* 16, 1–12 (1968).*

7. N. P. O'Dowd and C. F. Shih, "Family of Crack-Tip Fields Characterized by a Triaxiality Parameter: Part I—Structure of Fields," *J. Mech. Phys. Solids* 39, 989–1015 (1991).*

---

*Available in public technical libraries.

# Appendix C

## Small-Scale Yielding Conditions and Boundary-Layer Analysis

### C.1 Conditions of SSY

Conditions of SSY are present in a fracture mechanics application when a continuous annular region surrounding the crack tip can be located for which the influence of geometry, material behavior, and loading conditions can be expressed in terms of an "applied" value of the stress-intensity factor K that characterizes the magnitude of the near-crack-tip fields. Plane-strain fracture toughness is identified with the magnitude of K at the onset of crack initiation under conditions of SSY. Adoption of the SSY crack-tip fields as the reference distributions from which the Q-stress parameter is evaluated thus represents a natural measure of deviation from plane-strain constraint.

A unique feature of the SSY crack-tip fields is that they are self-similar with respect to the normalized distance parameter $r/(J/\sigma_0)$, where r is the planar polar distance ahead of the undeformed crack tip with its origin at the crack tip, J is the magnitude of the J-integral, and $\sigma_0$ is the initial yield stress in tension. Self-similarity in this case means that the spatial variation of the crack-tip fields, associated with a given magnitude of the applied K, is independent of the magnitude of K when the crack-tip fields are examined using the normalized distance parameter $r/(J/\sigma_0)$. A consequence of the self-similarity of the SSY crack-tip fields is that the magnitude of the applied remote loading, when expressed in terms of $(K/\sigma_0)^2$ or $J/\sigma_0$, represents the only relevant length scale under conditions of SSY. Based on well-known relations between $(K/\sigma_0)^2$ or $J/\sigma_0$ and the CTOD, self-similarity of the SSY crack-tip fields is equivalent to the viewpoint that under conditions of SSY the CTOD sets the size-scale of the fracture mechanics application.

### C.2 Boundary-Layer Analysis

In a boundary-layer analysis one takes advantage of the self-similarity of the SSY crack-tip fields by focusing directly on the near-crack-tip fields that result as a consequence of the global response of the structure under SSY conditions. Conditions of SSY are then associated with the asymptotic 2-D plane-strain fracture mechanics problem of a "semiinfinite" crack within an "infinite" continuum. Loading of the crack tip is characterized by a "remotely" applied stress-intensity factor K. The conditions of SSY require the spread of plasticity to be well confined within the elastic remote K-field. The elastic-plastic properties of the continuum are the same as those of the fracture

mechanics application under consideration. In the present study they correspond to those of the deep- and shallow-flaw specimens in Chap. 3 and to the various RPV material models in Chap. 4. Depending on analysis requirements in terms of material description and resolution of near-crack-tip fields, the analysis technique for performing a boundary-layer analysis can be based on the slip-line-field theory or the finite-element method.[1,*]

A boundary-layer approach using the finite-element code ABAQUS, assuming a rate-independent, $J_2$ (isotropic-hardening) incremental plasticity theory, is adopted in evaluating the reference SSY crack-tip fields in this study. In a finite-element-based boundary-layer approach the near-crack-tip region, over which the CTOD sets the size-scale of the problem, is modeled by constructing a finite-element mesh with a suitably large outer boundary as indicated in Fig. C.1(a). A unique feature of the finite-element mesh is a highly refined crack-tip region and the assumption of an initial root radius prior to the imposition of external loading as indicated in Fig. C.1(b). The outer radius of the mesh in Fig. C.1(a) is $1 \times 10^6$ times the initial root radius indicated in Fig. C.1(b). The finite-element mesh in Fig. C.1(a) and (b) is made up of 1119 10-node, isoparametric generalized-plane-strain elements and 3492 nodes. The integration order for these elements is $2 \times 2$.

The conditions of SSY require the spread of plasticity to be confined within the elastic "far-field" of the finite-element mesh, and in this study this requirement is accomplished by limiting the maximum extent of the plastic zone to be <10% of the outer mesh dimension. Convergence requirements of the finite-element results are accomplished by limiting the maximum value of the residual nodal force per unit thickness at any node to <0.1% of the product between the yield stress and the smallest element dimension in the finite-element mesh. Finally, the value of the CTOD upon reaching a target K value is at least 10 times the initial notch opening so that self-similarity of the SSY results is guaranteed.[*]

---

[*] B. R. Bass et al., Martin Marietta Energy Systems, Inc., Oak Ridge Natl. Lab., "Constraint Effects on Fracture Toughness for Circumferentially Oriented Cracks in Reactor Pressure Vessels," USNRC Report NUREG/CR-5792 (ORNL/TM-11968), to be published in June 1992.
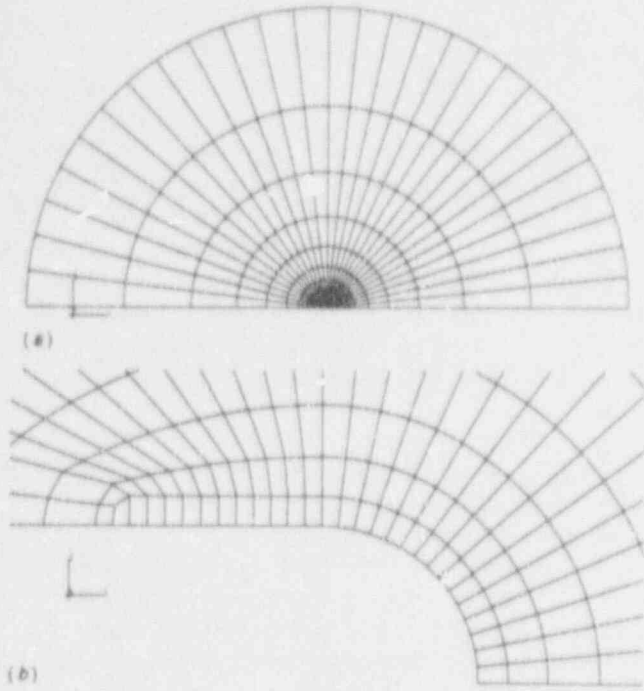
ORNL-DWG 92-2905 ETD



(a)

(b)

Figure C.1   Boundary-layer mesh

## Reference

1.  D. K. M. Shum et al., Martin Marietta Energy
    Systems, Inc., Oak Ridge Natl. Lab., "Analytical
    Studies of Transverse Strain Effects on Fracture
    Toughness for Circumferentially Oriented Cracks,"
    USNRC Report NUREG/CR-5592 (ORNL/
    TM-11581), April 1991.[*]

---

[*] Available for purchase from National Technical Information Service,
Springfield, VA 22161.

## Internal Distribution

1. D. J. Alexander
2. B. R. Bass
3. J. W. Bryson
4. E. W. Carver
5-6. R. D. Cheverton
7. J. M. Corum
8. W. R. Corwin
9. T. L. Dickson
10. F. M. Haggag
11. W. F. Jackson
12. J. E. Jones, Jr.
13. S. K. Iskander
14. J. Keeney-Walker
15. W. J. McAfee
16. D. E. McCabe
17. J. G. Merkle

18. R. K. Nanstad
19. D. J. Naus
20-25. W. E. Pennell
26. C. B. Oland
27. C. E. Pugh
28. G. C. Robinson
29-32. D. K. M. Shum
33. R. L. Swain
34-36. T. J. Theiss
37. E. W. Whitfield
38. ORNL Patent Section
39. Central Research Library
40. Document Reference Section
41. Laboratory Records Department
42. Laboratory Records (RC)

## External Distribution

43. L. C. Shao, Director, Division of Engineering, U.S. Nuclear Regulatory Commission, Washington, DC 20555

44. C. Z. Serpan, Jr., Division of Engineering, U.S. Nuclear Regulatory Commission, Washington, DC 20555

45. E. M. Hackett, Division of Engineering, U.S. Nuclear Regulatory Commission, Washington, DC 20555

46. A. L. Hiser, Division of Engineering, U.S. Nuclear Regulatory Commission, Washington, DC 20555

47-48. S. N. M. Malik, Division of Engineering, U.S. Nuclear Regulatory Commission, Washington, DC 20555

49. M. E. Mayfield, Division of Engineering, U.S. Nuclear Regulatory Commission, Washington, DC 20555

50. A. Taboada, Division of Engineering, U.S. Nuclear Regulatory Commission, Washington, DC 20555

51. J. W. Dally, Department of Mechanical Engineering, University of Maryland, College Park, MD 20742

52. W. L. Fourney, Department of Mechanical Engineering, University of Maryland, College Park, MD 20742

53. J. D. Landes, The University of Tennessee, Knoxville, TN 37996-2030

54-56. S. T. Rolfe, The University of Kansas, Lawrence, KS 66045-2235

57. A. R. Rosenfield, Battelle Columbus Division, Columbus, OH 43201

58. C. W. Schwartz, Department of Civil Engineering, University of Maryland, College Park, MD 20742

59. E. T. Wessel, 312 Wolverine, Haines City, FL 33844

60. Office of Assistant Manager for Energy Research and Development, DOE-OR, Oak Ridge, TN 37831

61-62. Office of Scientific and Technical Information, P. O. Box 62, Oak Ridge, TN 37831

| 1. REPORT NUMBER (Assigned by NRC, Add Vol., Supp., Rev., and Addendum Numbers, if any.) |
|---|
| NUREG/CR-5886 |
| ORNL/TM-12115 |

2. TITLE AND SUBTITLE

Experimental and Analytical Investigation of the Shallow-Flaw Effect in Reactor Pressure Vessels

| 3. DATE REPORT PUBLISHED | |
|---|---|
| MONTH | YEAR |
| July | 1992 |

| 4. FIN OR GRANT NUMBER |
|---|
| B0119 |

5. AUTHOR(S)

T. J. Theiss, D. K. Shum, S. T. Rolfe*

6. TYPE OF REPORT

Technical

7. PERIOD COVERED (Inclusive Dates)

8. PERFORMING ORGANIZATION — NAME AND ADDRESS (If NRC, provide Division, Office or Region, U.S. Nuclear Regulatory Commission, and mailing address; if contractor, provide name and mailing address.)

Oak Ridge National Laboratory          *University of Kansas
Oak Ridge, TN  37831-6285                Lawrence, KS

9. SPONSORING ORGANIZATION — NAME AND ADDRESS (If NRC, type "Same as above"; if contractor, provide NRC Division, Office or Region, U.S. Nuclear Regulatory Commission, and mailing address.)

Division of Engineering
Office of Nuclear Regulatory Research
U.S. Nuclear Regulatory Commission
Washington, DC  20555

10. SUPPLEMENTARY NOTES

11. ABSTRACT (200 words or less)    The Heavy-Section Steel Technology (HSST) Program is investigating the increase in effective fracture toughness of A 533 B steel associated with shallow flaws and the implications of the shallow-flaw effect on reactor pressure vessel (RPV) life assessments. Test data from beams indicate a significant increase in the fracture toughness of shallow-crack specimens compared with deep-crack specimens in the transition region of the toughness curve for unirradiated A 533 B steel. If the toughness increase present in the test specimens were also present in a reactor vessel, the impact on pressurized-thermal shock (PTS) analyses could be significant. To facilitate transferability of the specimen data to an RPV, posttest finite-element analyses have been performed on several test specimens and a reactor vessel for a single (PTS) transient. The analyses are sufficiently refined to allow interpretation of the results in terms of the J-integral and the so-called Q-stress parameter under plane-strain analysis assumptions. A negative Q-stress parameter is indicative of a loss of crack-tip constraint, which is associated with an increase in the fracture toughness. Analyses of the test specimens indicate that at the onset of crack initiation the deep-crack specimens exhibit an essentially zero Q-stress parameter but that the shallow-crack specimen exhibits a Q-stress parameter of about –0.7, which indicates a substantial loss of constraint in the shallow-crack beam. Using the test data and posttest analysis, a locus of toughness data in terms of the J-integral and the Q-stress parameter has been constructed for a particular temperature. Analyses were also performed on an RPV with a shallow flaw under PTS loading conditions up to the maximum value of J. At maximum J, the analyses reveal a Q-stress parameter about –0.2 to –0.4, which indicates some constraint loss but less than in the shallow-crack test specimens. Considering the RPV in terms of J-integral and Q-stress suggests there may be a larger margin of safety than would be found using the J-integral alone. Thermal-shock data, which were generated using cylindrical vessels under thermal shock loading, show no significant increase in toughness even for shallow-flaw depths. The thermal shock data seem to indicate two offsetting effects: a shallow-flaw effect, which increases toughness, and an out-of-plane (biaxial) stress effect, which decreases toughness. Additional work is necessary to resolve outstanding issues for applying shallow-crack data to an RPV and validating the J-Q technique for fracture evaluations.

12. KEY WORDS/DESCRIPTORS (List words or phrases that will assist researchers in locating the report.)

fracture toughness, elastic-plastic fracture, shallow-crack toughness, Q-stress, reactor pressure vellel (RPV), pressurized-thermal shock (PTS), A533B, constraint loss, Heavy-Section Steel Technology (HSST) Program, shallow-flaw effect

| 13. AVAILABILITY STATEMENT |
|---|
| Unlimited |

| 14. SECURITY CLASSIFICATION |
|---|
| (This Page) |
| Unclassified |
| (This Report) |
| Unclassified |

| 15. NUMBER OF PAGES |
|---|

| 16. PRICE |
|---|

UNITED STATES
NUCLEAR REGULATORY COMMISSION
WASHINGTON, D.C. 20555-0001